A genetic screen identifies processes that couple oocyte maturation to proteostasis in the immortal *C. elegans* germ lineage

Madhuja Samaddar*[,1], Jérôme Goudeau*[,1], Melissa Sanchez[2], David H. Hall[3], K. Adam Bohnert[1,#], Maria Ingaramo[1] and Cynthia Kenyon[1,†]

[1]Calico Life Sciences LLC, South San Francisco, CA 94080, USA.

[2]Department of Molecular and Cellular Biology, University of California, Berkeley, CA 94720, USA.

[3]Dominick P. Purpura Department of Neuroscience, Albert Einstein College of Medicine, New York, NY 01461, USA.

[#]Present address: Department of Biological Sciences, Louisiana State University, Baton Rouge, LA 70803

* These authors contributed equally

[†] Correspondence to: cynthia@calicolabs.com

Abstract

Somatic cells age and die, but the germ-cell lineage is immortal. In *C. elegans,* oocyte-maturation signals from sperm trigger the clearance of carbonylated proteins and protein aggregates. Here, we explore the cell biology of this proteostasis renewal in the context of a whole-genome RNAi screen for knockdowns that interfere with aggregate clearance. Oocyte-maturation signals are known to trigger protein-aggregate removal via lysosome acidification, and our findings suggest that lysosomes are acidified as a consequence of changes in ER morphology and function that permit assembly of the lysosomal V-ATPase. Once lysosomes are acidified, our genetic findings support the model that they remove aggregates by microautophagy. We also define two functions for mitochondria in this proteostasis renewal, both of which appear to be independent of mitochondrial ATP generation. Finally, many genes from the screen also regulate lysosome acidification and age-dependent protein aggregation in the soma, suggesting a fundamental mechanistic link between proteostasis renewal in the germline and the maintenance of the soma.

Introduction

The germ cells of an organism not only give rise to the rich diversity of somatic lineages, they also generate new germ cells that, by seeding subsequent generations, confer species immortality. This sequential rejuvenation of youthfulness is one of the most interesting mysteries in biology. How is it achieved? Not surprisingly, a process so crucial to the survival of the species involves multiple levels of quality control. At one level, an entire oocyte can be eliminated via apoptosis; for example, following DNA damage (Hunter, 2017; Luo et al., 2010; Qiao et al., 2018; Schumacher et al., 2001). Oocytes can also eliminate defective organelles or age-related molecular damage. For example, in mice, mitochondria containing defective DNA are eliminated during oogenesis (Fan et al., 2008), and in yeast, nuclear senescence factors and protein aggregates are extruded during meiosis (King et al., 2019; Ünal et al., 2011). Mechanisms likely exist to counteract protein aggregation in *Drosophila* as well: relative to the soma, the eggs of *Drosophila* exhibit enhanced proteasome activity and resistance to protein aggregation (Fredriksson et al., 2012). Autophagy, a process known to eliminate damaged organelles and macromolecules, may play a role as well, as it is required for the survival of the mouse germ lineage (Gawriluk et al., 2011).

The nematode *C. elegans* is a valuable organism for studies of germline quality control. The animal is transparent and genetically accessible, allowing one to analyze the effects of perturbations over time in living animals using fluorescent reporters. *C. elegans* is a hermaphrodite, producing both sperm and oocytes in each of two symmetrical gonadal arms. Germ cells originate in stem-cell niches located at the distal ends of each arm and pass through successive stages of meiosis as they move proximally towards the spermatheca, where fertilization occurs (Crittenden et al., 1994; Hubbard and Greenstein, 2005; Mccarter et al., 1999). (Figure 1A). In 2010, Goudeau and Aguilaniu discovered that carbonylated proteins, known to accumulate during aging, are present throughout the distal germline, but are eliminated in proximal oocytes (Goudeau and Aguilaniu, 2010). Mutant worms that lack sperm

84 and develop as females retain carbonylated proteins throughout the entire germline, indicating
85 that sperm play a role in their elimination. In addition to carbonylated proteins, protein
86 aggregates also accumulate in the proximal oocytes of females but not in those of
87 hermaphrodites (Bohnert and Kenyon, 2017). Signals from sperm trigger the elimination of
88 protein aggregates in a process that is coupled to the broader choreography of oocyte
89 maturation, which involves dramatic changes in organelle morphology and function (Bluemink et
90 al., 1983; Carroll et al., 1996; Charbonneau and Grey, 1984; FitzHarris et al., 2007; Kobayashi
91 et al., 1991; Maller et al., 1977; Mehlmann et al., 1995; Wasserman et al., 1982; Yamashita,
92 2018). In *C. elegans,* oocyte maturation is triggered by actin-like major sperm proteins (MSPs)
93 released from sperm (Kosinki et al., 2005; Miller et al., 2003, 2001), and involves changes in
94 chromosome and nuclear dynamics linked to progression through meiosis, up-regulation of
95 translation, and changes in ER, lysosomal and mitochondrial function (Bohnert and Kenyon,
96 2017; Huelgas-Morales and Greenstein, 2018; Langerak et al., 2019). The shift in lysosomal
97 physiology that occurs during oocyte maturation is crucial for aggregate removal: the sperm-
98 derived signals trigger the acidification of lysosomes, which in turn engulf the aggregates by a
99 process that resembles microautophagy morphologically (Bohnert and Kenyon, 2017).
100 Lysosomal acidification also triggers a conversion in mitochondrial dynamics from what appears
101 to be a poised state, characterized by a high membrane potential, to an active state, in which
102 the potential is reduced. Conditions that prevent this mitochondrial membrane-potential shift,
103 such as inactivation of mitochondrial ATP synthase, prevent aggregate removal. However, how
104 lysosomes become acidified in response to sperm signals, how mitochondria contribute to
105 aggregate removal, and whether other organelles also play a role in aggregate clearance are
106 important outstanding questions.
107 To better understand mechanisms of proteostasis enhancement in the *C. elegans* germ
108 lineage, we combined cell biological approaches with a confocal-microscopy based genome-
109 wide RNAi screen for gene knockdowns that cause protein aggregates to accumulate even in

110 the presence of sperm. Our findings deepen our understanding of many aspects of protein
111 aggregation and clearance within the germline. Specifically, we find that (i) protein aggregates
112 accumulate in young, newly formed oocytes in the absence of sperm—their formation is an
113 integral part of oocyte development, rather than a consequence of prolonged oocyte
114 quiescence; (ii) inhibiting processes required for changes in ER morphogenesis and function
115 during oocyte maturation, including protein synthesis and actin dynamics, prevents lysosome
116 acidification by preventing the assembly of the V-ATPase lysosomal proton pump; (iii)
117 mitochondria elaborate an energy-independent checkpoint that gates protein-aggregate
118 removal; (iv) ESCRT vesicle-transport proteins are required for aggregate removal, consistent
119 with protein aggregates being removed via microautophagy; and, unexpectedly (v) as with
120 proteasome inhibition, inhibiting TRiC-complex chaperonins or HSP70 chaperones promotes
121 protein aggregation indirectly, by acting upstream in the pathway to block lysosome
122 acidification. Finally, we show that inhibiting lysosomal V-ATPase, vesicle-transport or
123 proteasome function also accelerates age-dependent protein aggregation in the soma, thus
124 bridging mechanisms that enhance proteostasis in the immortal germ lineage to those that
125 maintain proteostasis in the aging soma.
126
127
128
129
130
131
132
133
134

Results

A genome-wide RNAi screen identifies 84 genes that influence oocyte protein aggregation.

To undertake an unbiased genome-wide RNAi screen for components of the germline proteostasis network, we utilized the Ahringer RNAi feeding library (Kamath et al., 2003), which targets ~87% of annotated *C. elegans* genes, to identify gene inhibitions that cause proteins to aggregate even in the presence of sperm; that is, in hermaphrodites. A germline-specific GFP::RHO-1 translational fusion was selected as the reporter for the screen, as it forms dense patchy aggregates in female oocytes (Bohnert and Kenyon, 2017) and in unfertilized oocytes of aging hermaphrodites, which deplete their stores of sperm (David et al., 2010). Oocytes are formed in young adults, so RNAi was initiated at the beginning of the last larval stage (L4) to reduce the chance of missing genes with essential roles during development (Figure 1B). The animals were examined manually by confocal microscopy on day 2 of adulthood for the presence of GFP::RHO-1 aggregates in proximal oocytes (Figure 1A, 1B and S1A). The primary screen identified 367 genes whose knockdown led to GFP::RHO-1 aggregation in at least 50% of the animals. To eliminate false positives, the candidates were subjected to three independent rounds of validation using a similar workflow, with at least two independent rounds from two experimentalists (Figure 1C). We note that false negatives could result from failure of an RNAi bacterial strain to grow adequately, from insufficient or excessive gene inhibition, or because of functional redundancy.

The resulting set of 88 genes represented diverse cellular processes (Table S1), with highly enriched gene ontology (GO) categories including translation, RNA processing and cytoskeletal organization (Figure S1C). In addition, ATP-hydrolysis-coupled proton transport and lysosome acidification were both highly enriched, in agreement with our previous findings (Bohnert and Kenyon, 2017). We sorted the candidates according to relative representation in major biological processes (Figure 1D), after discarding candidates with known roles in male gonad and germ cell development (*fkh-6, spe-15*), in regulation of our proteostasis marker

161 RHO-1 (*cyk-4*), or with potential off-target effects (*adr-1* and *dhs-5*) (Table S1). Protein
162 synthesis and degradation, RNA processing, protein folding, and lysosome acidification were
163 strongly represented biological processes, as were genes involved in cytoskeletal organization,
164 including four of the five *C. elegans* actin genes. Among organelle systems, multiple candidates
165 were associated with ER homeostasis (*hsp-4, spcs-1 and srpa-68*) and vesicle-mediated
166 transport (*copb-2, sec-24.1, sar-1, rab-11.1* and *E03H4.8*). We also identified genes that could
167 not be classified into any of the highly-enriched biological-process categories and were
168 designated 'orphans' (Table S1 and Fig. 1D).
169 We subjected representative candidates from each group, as well as all the orphans, to
170 an orthogonal screening approach, this time utilizing a different aggregation reporter, a
171 germline-specific NMY-2::GFP fusion protein (Bohnert and Kenyon, 2017) that forms distinctive
172 punctate aggregates in the absence of sperm (Figure 1C and Table S1). Out of the 55
173 candidates tested, 53 RNAi knockdowns also caused NMY-2::GFP protein-aggregate
174 accumulation (Figure S1B). Thus, these genes are likely to have a general effect on protein-
175 aggregate clearance rather than a specific effect on GFP::RHO-1.
176

Figure 1

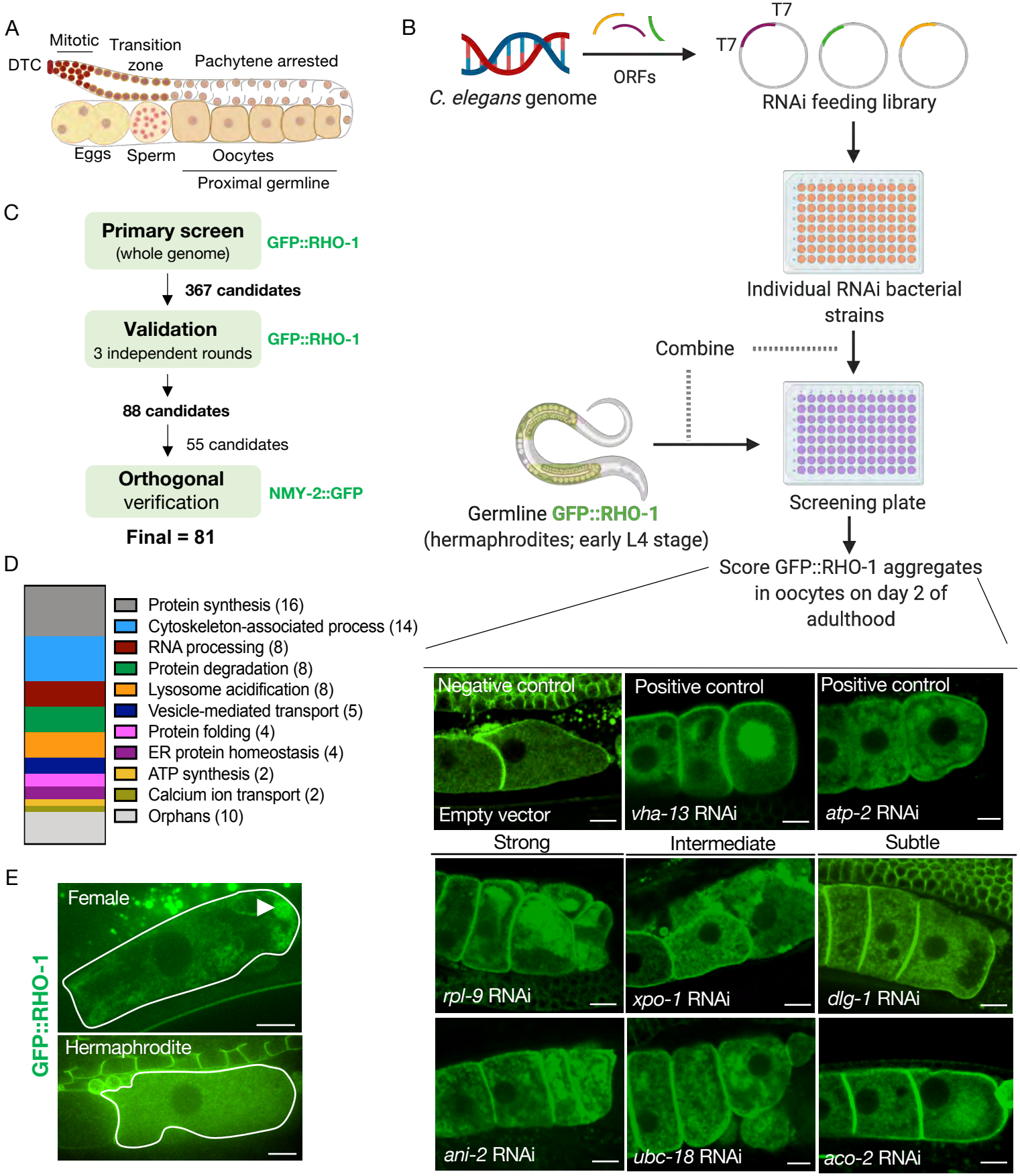
A
Mitotic
Transition zone
DTC
Pachytene arrested
Eggs
Sperm
Oocytes
Proximal germline
B
C. elegans genome
ORFs
T7
T7
RNAi feeding library
Individual RNAi bacterial strains
Combine
Germline GFP::RHO-1 (hermaphrodites; early L4 stage)
Screening plate
Score GFP::RHO-1 aggregates in oocytes on day 2 of adulthood
C
Primary screen (whole genome)
GFP::RHO-1
367 candidates
Validation 3 independent rounds
GFP::RHO-1
88 candidates
55 candidates
Orthogonal verification
NMY-2::GFP
Final = 81
D
Protein synthesis (16)
Cytoskeleton-associated process (14)
RNA processing (8)
Protein degradation (8)
Lysosome acidification (8)
Vesicle-mediated transport (5)
Protein folding (4)
ER protein homeostasis (4)
ATP synthesis (2)
Calcium ion transport (2)
Orphans (10)
Negative control
Empty vector
Positive control
vha-13 RNAi
Positive control
atp-2 RNAi
Strong
Intermediate
Subtle
rpl-9 RNAi
xpo-1 RNAi
dlg-1 RNAi
ani-2 RNAi
ubc-18 RNAi
aco-2 RNAi
E
GFP::RHO-1
Female
Hermaphrodite

Figure 1. **Identification of genes that prevent protein aggregation in maturing *C. elegans* oocytes.** (A) Diagram of the *C. elegans* germline (B) Genome-wide RNAi-screen workflow. High resolution images from the validation rounds are represented here. Scale bars, 10 μm. (C) Schematic representing the procedure used for candidate validation and orthogonal verification using two independent germline-specific reporters. 45 candidates representing the major GO categories and all 10 orphans were subjected to orthogonal verification. (D) Common biological process GO categories enriched in the screen. Genes that were not members of these enriched categories were classified as orphans. (E) Very early oocytes of females and hermaphrodites (CF4557 and CF4552 strains, respectively). GFP::RHO-1 aggregates often appear in newly-formed female oocytes. Scale bars, 10 μm.

177 *Aggregates form in young proximal oocytes.*

178 We classified the RNAi phenotypes as strong, intermediate or subtle based on the
179 degree of GFP::RHO-1 aggregation (Table S1). Typically, the phenotypically strong
180 knockdowns led to sterility, whereas the subtle knockdowns generally did not, though some
181 reduced the brood size. In principle, one could imagine that aggregates accumulate in oocytes
182 from sterile hermaphrodites because oocytes that would normally undergo ovulation and pass
183 into the uterus do not, and instead simply "age in place". Likewise, aggregates could
184 accumulate in normal female oocytes because in the absence of sperm, they proceed much
185 more slowly through the spermatheca and into the uterus (Mccarter et al., 1999). As a
186 consequence, proximal oocytes of females are technically older than those of age-matched
187 hermaphrodites (Kim et al., 2013). This oocyte-age discrepancy raises the question of whether
188 aggregates accumulate only during long-term oocyte quiescence, or whether they are present in
189 newly formed female oocytes. To address this question, we collected age-matched late L4
190 ('Christmas-tree' stage) females and hermaphrodites and followed the hermaphrodites until their
191 first oocytes were cellularized. We found that age-matched first-proximal oocytes of young
192 females often contained protein aggregates (Figure 1E and S4). Therefore, protein-aggregate
193 accumulation does not require prolonged oocyte quiescence; instead, it appears to be part of
194 the normal developmental sequence of oocytes that are not exposed to sperm.
195

196 *The endoplasmic reticulum influences protein aggregation*

197 Many genes we identified were associated with the ER, so we explored ER biology in
198 more detail. The ER undergoes a major morphological rearrangement in response to oocyte
199 maturation signals (Langerak et al., 2019). We visualized the ER in *C. elegans* oocytes using a
200 germline-specific mCherry::SP12 reporter (Joseph-Strauss et al., 2012). SP12 is a signal-
201 peptidase subunit (Poteryaev et al., 2005) and *spcs-1*, which encodes SP12, was identified in
202 our screen. In hermaphrodite oocytes, the ER assumed a fine network appearance, whereas in
203 female oocytes, the ER formed bright, distinctive patches (Figure 2A, 2C and S2A). We also
204 examined ER morphology in the first, newly-formed female oocytes, using the L4 staging
205 procedure described above. Pristine female oocytes also exhibited ER patches, indicating that
206 the altered ER architecture is an intrinsic property of female oocytes and not a consequence of
207 prolonged quiescence (Figure 2B and S2B). The fluorescent signal from the female ER was
208 further enhanced as oocytes aged, possibly due to continued ER biogenesis coupled with
209 oocyte compression caused by their packing within the gonad (Figure S2A). Using two
210 fluorescent reporters, we visualized both the ER and GFP::RHO-1 simultaneously (Figure 2B,
211 S2C, S3 and S4), and found that in female oocytes, the ER and GFP::RHO-1 aggregates
212 segregated spatially into mutually-exclusive regions (Figure 2B, S2C and S4).

213 We also examined oocytes from young, age-matched hermaphrodites and females by
214 transmission electron microscopy (TEM). The ER in pristine oocytes from both sexes appeared
215 to be associated with ribosomes, indicative of active (or poised) protein synthesis, yet the
216 female ER was distinctively clustered into parallel stacks (Figure 2D and S5).

217 To test whether the stacked ER architecture of female oocytes could be reversed by
218 sperm, we visualized fluorescently-tagged ER and NMY-2::GFP aggregates simultaneously
219 over time in female oocytes after mating. The presence of sperm triggered distinctive
220 remodeling of the ER architecture and the clearance of aggregates, although with different
221 kinetics (Figure 2E and S6A). The earliest changes in the ER were detected approximately 10

222 minutes after mating, and the morphology was significantly altered by 30 minutes (Figure 2E). In
223 contrast, the clearance of NMY-2 aggregates started a few minutes later, with aggregate
224 clearance in the most proximal oocytes typically occurring between 20 to 30 minutes after
225 mating (Figure S6A, S6B and S7A).

226 Next, we investigated whether the genes identified in our RNAi screen might contribute
227 to proteostasis by influencing a process associated with ER architecture. To this end, we
228 subjected mCherry::SP12-germline-labeled hermaphrodites to 35 RNAi treatments representing
229 the various biological process categories as well as the individual orphans. This subset of RNAi
230 clones, which we termed the "assay pool", was used for all subsequent large-scale phenotypic
231 analyses (Table 1). We visualized oocyte ER morphology in young adults subjected to the gene
232 knockdowns (Figure S7B and Table 1). Genes involved in cytoskeletal organization, protein
233 synthesis and protein folding were required for maintaining normal ER morphology and led to an
234 altered ER architecture when knocked down. Genes involved in RNA processing, protein
235 degradation and trafficking comprised a mixed class, with some knockdowns appearing to affect
236 ER morphology. [We note that our analysis does not distinguish between genes with direct
237 effects on ER morphogenesis, like the actin cytoskeleton (Poteryaev et al., 2005), and genes
238 with indirect effects, like the proteasome, which is required for the degradation of GLD-1
239 (Bohnert and Kenyon, 2017; Goudeau et al., 2020b; Spike et al., 2018), a translational
240 repressor involved in oocyte cell fate determination (Francis et al., 1995; Jones et al., 1996)].
241 Notably, disrupting the mitochondrial ATP synthase, the V-ATPase complex or ER function itself
242 did not visibly alter the ER network, suggesting that these gene functions were not required for
243 the sperm-induced ER morphology change, or more generally for ER morphogenesis.

Figure 2

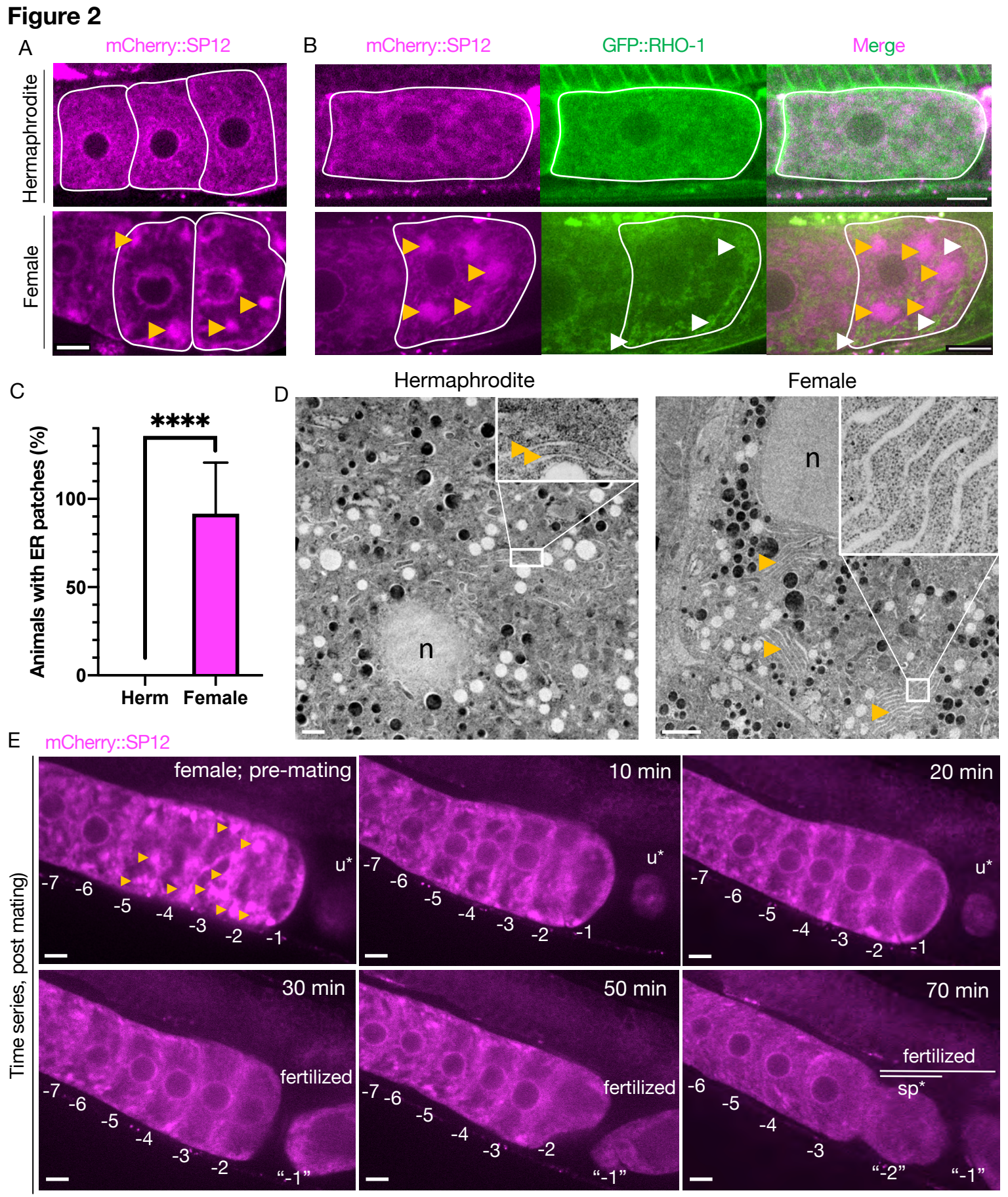
A
mCherry::SP12
Hermaphrodite
Female
B
mCherry::SP12
GFP::RHO-1
Merge
C
****
Animals with ER patches (%)
100
50
0
Herm
Female
D
Hermaphrodite
Female
n
n
E
mCherry::SP12
Time series, post mating)
female; pre-mating
10 min
20 min
30 min
50 min
70 min
u*
-7
-6
-5
-4
-3
-2
-1
fertilized
"-1"
sp*
"-2"

Figure 2. ER morphology is regulated by sperm and correlates with protein aggregation.

(A) ER morphology in the germline of hermaphrodite (OCF15) and female (CF4542) animals, visualized using a mCherry::SP12 reporter. Orange arrows, ER patches. Scale bar, 10 μm. (B) GFP::RHO-1 localization in newly-formed oocytes from hermaphrodites (CF4552) and females (CF4557) also expressing mCherry::SP12. White arrows, GFP::RHO-1 aggregates. Scale bars, 10 μm. (C) Percentage of animals with ER patches in oocytes. n=12; mean +/- s.d., **** $P \leq 0.0001$. (D) Transmission electron micrographs from hermaphrodite (N2E) and female (CF4101) oocytes. Orange arrows, ER. Left panel, magnification 1,400X, scale bar, 1 μm; inset: magnification 13,000X, scale bar, 100 nm. Right panel, magnification 1,200X, scale bar, 2 μm; inset: magnification 18,500X, scale bar, 100 nm. (E) Reversal of ER patches (orange arrows) in female oocytes upon mating with CB1490 males. Female oocytes were imaged before and after mating at the indicated time points. Each oocyte is numbered according to its initial position relative to the spermatheca, and original numbers are maintained after fertilization. The figure shows a single representative animal, from 7 independent experiments. u*, unfertilized oocyte/debris in uterus in a different focal plane; sp*, an oocyte passing through spermatheca during fertilization. Scale bars, 10 μm.

Biological process	RNAi targeted against	Gene code	Normal ER network architecture	GFP::VHA-13 puncta (skewness)	Lysosome acidification	Reduction in mitochondrial membrane potential
Protein degradation	*pbs-7*	F39H11.5	No	No	No	No
	rpn-6.1	F57B9.10	Mixed	No	No	No
Protein synthesis (Translation)	*rps-20*	Y105E8A.16	No	No	No	No
	rpl-3	F13B10.2	No	No	No	No
Protein folding (Chaperones)	*cct-1*	T05C12.7	No	Reduced	No	No
	cct-5	C07G2.3	No	Reduced	No	No
Cytoskeleton-associated process	*act-1*	T04C12.6	No	No	No	No
	pat-3	ZK1058.2	No	No	No	No
	ani-2	K10B2.5	No	No	No	No
ER protein homeostasis	*hsp-4*	F43E2.8	Yes	No	No	No
	spcs-1	C34B2.10	Yes	No	No	No
	srpa-68	F55C5.8	Yes	No	No	No
Vesicle-mediated transport (Trafficking)	*copb-2*	F38E11.5	No	No	No	No
	sec-24.1	F12F6.6	Inconclusive	No	No	No
	sar-1	ZK180.4	Mixed	No	No	No
Lysosome acidification (V-ATPase)	*vha-13*	Y49A3A.2	Yes	No signal	No	No
	vha-12	F20B6.2	Yes	No	No	No
	vha-2	R10E11.2	Yes	No	No	No
ATP synthase	*atp-3*	F27C1.7	Yes	Yes	Yes	No
	atp-2	C34E10.6	Yes	Yes	Yes	No
RNA processing	*ess-2*	F42H10.7	No	Reduced	No	No
	cgh-1	C07H6.5	Mixed	No	No	No
	let-711	F57B9.2	Mixed	Reduced	No	No
Calcium ion transport	*itr-1*	F33D4.2	No	Reduced	No	No
	sca-1	K11D9.2	Yes	Reduced	No	No
Orphans	*kin-2*	R07E4.6	Mixed	No	No	No
	ttr-14	T05A10.3	Mixed	No	No	No
	par-5	M117.2	Yes	No	No	No
	xpo-1	ZK742.1	Yes	No	No	No
	srab-17	T11A5.2	Yes	Reduced	No	No
	rmd-2	C27H6.4	Yes	No	No	No
	dlg-1	C25F6.2a.1	No	No	No	No
	lgc-46	Y71D11A.5	Yes	Reduced	No	No
	aco-2	F54H12.1	Yes	No	No	No
	imb-1	F28B3.8	Inconclusive	No	No	No
ESCRT subunits*	*vps-20*	Y65B4A.3	Not tested	Yes	Yes	Not tested
	vps-28	Y87G2A.10	Not tested	Yes	Yes	Not tested
	vps-37	CD4.4	Not tested	Yes	Yes	Not tested
	vps-54	T21C9.2	Not tested	Yes	Yes	Not tested

Table 1. Functional gene categories from the proteostasis screen.

List of representative genes from each functional category that were selected for the assay pool and their effects on ER morphology, lysosome acidification, GFP::VHA-13 localization, and mitochondrial membrane potential. The ESCRT complex subunits (*) were not derived from the original screen but from subsequent candidate testing.

244 *Sperm signals initiate V-ATPase assembly, enabling lysosomal acidification*

245 Signals from sperm elicit the lysosomal acidification required for the clearance of protein
246 aggregates, and inhibiting the V-ATPase, which acidifies lysosomes, causes proteins to
247 aggregate in hermaphrodite oocytes (Bohnert and Kenyon, 2017). However, the mechanism by
248 which lysosome acidification occurs in response to signals from sperm is not known (Goudeau
249 et al., 2020b; Spike et al., 2018). To address this question with minimal physiological disruption,
250 we first attempted to fluorescently tag endogenously-expressed V-ATPase subunits using
251 CRISPR/Cas9. We picked four different subunits, two from the membrane-embedded V_0 domain
252 (VHA-4 and VHA-7) and two from the peripheral V_1 domain (VHA-11 and VHA-13) (Table S2).
253 Unexpectedly, although each one of these tagged proteins was visible in somatic tissues, we
254 were unable to detect any fluorescence in the germline in either intact animals (Figure S8) or in
255 their dissected gonads (Figure S9A). Germline fluorescence was also undetectable when
256 imaging with a more sensitive wide-field system, or following photobleaching of the strong
257 intestinal signal, which we reasoned might mask a faint signal from the germline (data not
258 shown). Endogenous genes tagged with fluorescent proteins can be silenced in the germline by
259 the process of epigenetic RNAe (Shirayama et al., 2012); however, this explanation seems
260 unlikely since, unlike V-ATPase RNAi-treated animals, these animals produced viable embryos.

261 We also considered the possibility that these V-ATPase proteins did not act cell-
262 autonomously in the gonad, though V-ATPase mRNAs previously had been identified as direct
263 targets of the germline-specific GLD-1 translational regulator (Wright et al., 2011). To
264 investigate cell autonomy, we carried out tissue-specific RNAi experiments using sterility as a
265 phenotypic readout. Three hermaphrodite strains [wild-type, globally RNAi-defective *rde-*
266 *1(mkc36)* mutants (DCL565), and germline-only RNAi-sensitive DCL569 animals (Zou et al.,
267 2019)] were subjected to RNAi from hatching (empty vector, *vha-12* and *vha-13*). Both wild-type
268 and germline-RNAi-permissive DCL569 animals exhibited sterility when fed *vha-12* and *vha-13*
269 RNAi bacteria (Figure S9B), whereas the whole-body RNAi-defective *rde-1* mutant did not.

270 Thus, these V-ATPase subunits are expressed and required in the germline, despite our inability
271 to detect them when tagged endogenously.
272 As a next-best approach for visualizing germline V-ATPase subunits, we obtained a
273 Mos1-mediated Single Copy Insertion (MosSCI) of GFP::VHA-13 driven by the germline-specific
274 *pie-1* promoter. This construct expressed GFP::VHA-13 in a genetically-stable fashion, though
275 presumably at elevated levels. In this strain, we observed a striking, sperm-dependent pattern:
276 GFP::VHA-13 formed distinct foci in hermaphrodite oocytes (Figure 3A and S10A) that co-
277 localized with foci of LysoTracker, a dye that stains acidic lysosomes (Figure 3B and S11A). In
278 contrast, the proximal oocytes of females exhibited diffuse GFP::VHA-13 fluorescent signal
279 (Figure 3A and S10B), with a slight enrichment in the perinuclear region. Female oocytes
280 demonstrated very weak LysoTracker staining (Bohnert and Kenyon, 2017), and there was no
281 significant overlap in the two signals (Figure 3B and S11B). To better control for effects of
282 overexpression, we lowered the level of GFP::VHA-13 expression by serially diluting *gfp* RNAi
283 bacteria. Even at the limit of detection, hermaphrodites still exhibited GFP::VHA-13 foci, and
284 females exhibited a diffuse distribution (Figure S9C). Thus, the germline harbors a mechanism
285 by which VHA-13 is localized to discrete, acidic cellular locations, indicative of lysosomes, only
286 in the presence of sperm. Notably, knocking down the *vha-12* gene, which encodes another
287 peripheral V-ATPase V_1-domain subunit, also prevented GFP::VHA-13 foci formation in
288 hermaphrodite oocytes (Figure S9D), suggesting a coordinated assembly pathway.
289 To ask whether sperm signals regulate V-ATPase localization, we mated GFP::VHA-13-
290 expressing females with males and monitored their proximal oocytes. The diffuse fluorescent
291 signal began to change approximately 10 minutes after mating, organizing into distinct foci
292 within 20 to 30 minutes (Figure 3C and 3D). This change coincided with release from arrest and
293 oocyte maturation, ultimately leading to ovulation and fertilization. The time scales of ER
294 remodeling and GFP::VHA-13 relocalization (Figure 2E) were strikingly similar, suggesting a
295 possible causal relationship. Together these findings suggest that sperm signals lead to

296 lysosome acidification by initiating the recruitment of V-ATPase subunits to the surface of the

297 lysosome and enabling proton-pump assembly.

298

Figure 3

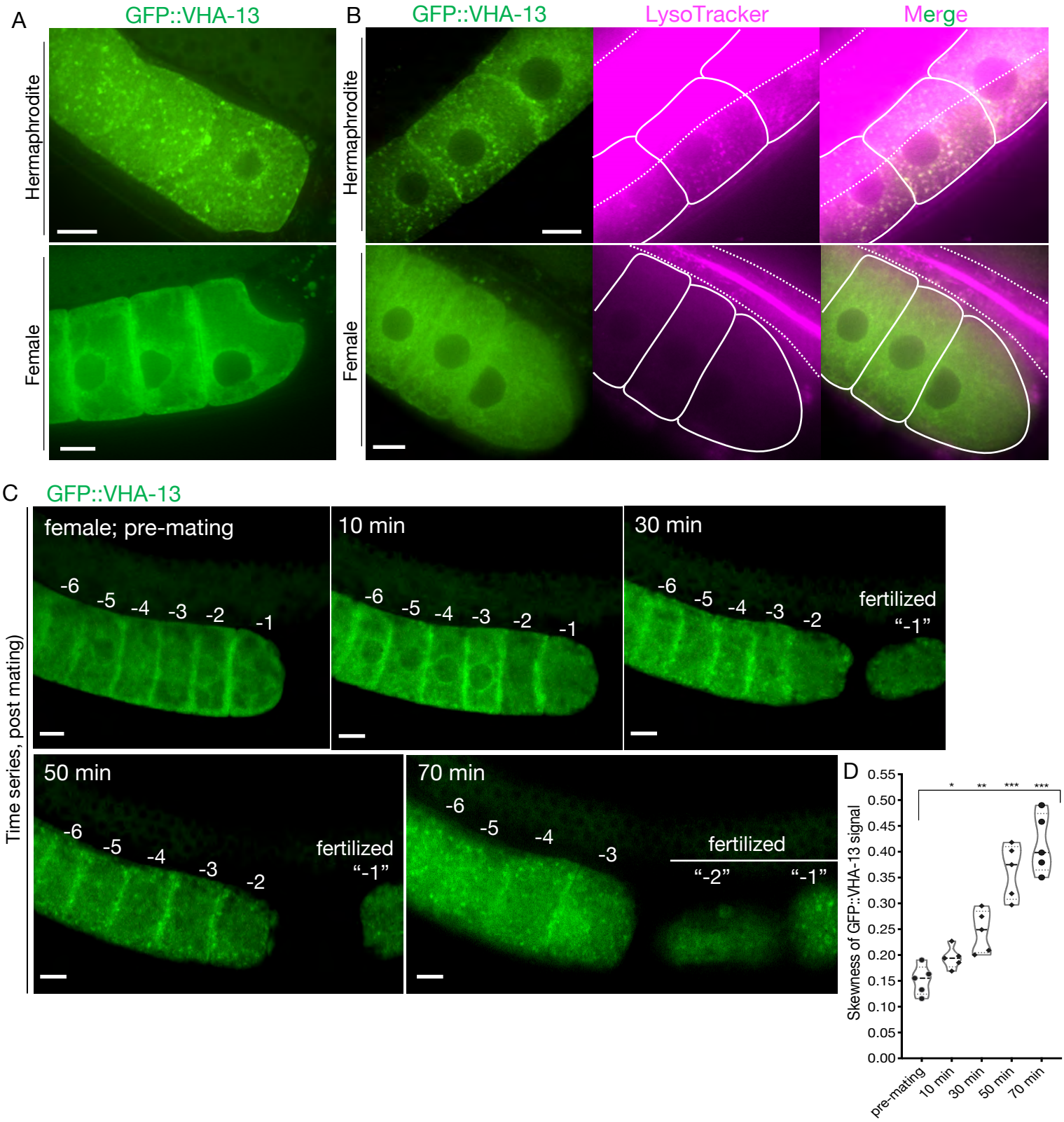
A
GFP::VHA-13
Hermaphrodite
Female
B
GFP::VHA-13
LysoTracker
Merge
Hermaphrodite
Female
C
GFP::VHA-13
Time series, post mating)
female; pre-mating
-6
-5
-4
-3
-2
-1
10 min
30 min
fertilized
"-1"
50 min
70 min
"-2"
D
Skewness of GFP::VHA-13 signal
0.55
0.50
0.45
0.40
0.35
0.30
0.25
0.20
0.15
0.10
0.05
0.00
*
**
***
pre-mating
10 min
30 min
50 min
70 min

Figure 3. Sperm-dependent lysosomal localization of VHA-13.

(A) Distribution of GFP::VHA-13 in proximal oocytes of hermaphrodites (PHX1414) and females (CF4599). (B) LysoTracker-stained oocytes from *gfp::vha-13*-expressing hermaphrodites and females, for visualization of acidic lysosomes. The two signals colocalize in hermaphrodite oocytes. Dotted line; intestinal boundary, and solid line; oocytes. (C) Sperm signal-induced GFP::VHA-13 redistribution in female oocytes (CF4599). Oocytes were imaged before and after mating with CB1490 males. The GFP::VHA-13 signal shifts from diffuse to punctate following mating. Each oocyte is numbered according to its initial position relative to the spermatheca, and original numbers are maintained after fertilization. A representative individual is shown, from 5 independent mating experiments. (D) Increase in signal skewness (inhomogeneity) of GFP::VHA-13 as a function of time following mating. Unpaired t-test with Welch's correction was used to determine statistical significance, and P values are represented as $P \leq 0.05$ = *, $P \leq 0.01$ = **, and $P \leq 0.001$ = ***. Scale bars, 10 μm (A-C).

299 *Most of the genes identified disrupt VHA-13 localization and lysosome acidification.*

300 To ask which gene inhibitions blocked lysosome acidification, we subjected
301 LysoTracker-stained hermaphrodites to knockdowns of the 'assay-pool' genes (Table 1). In wild-
302 type hermaphrodites, lysosomes are acidified only in proximal oocytes (Bohnert and Kenyon,
303 2017). Therefore, to internally control for variations in dye uptake, we analyzed the ratios of
304 staining intensities between proximal oocytes and distal germline regions. LysoTracker staining
305 of hermaphrodites, females and animals subjected to empty-vector RNAi, were used as
306 controls, and the simultaneous presence of GFP::RHO-1 aggregates confirmed successful gene
307 knockdown. Unexpectedly, we found that the great majority of gene inhibitions prevented
308 lysosome acidification (Figure 4A and S12A). The ATP synthase genes *atp-2* and *atp-3* were
309 the only exceptions, consistent with previous observations suggesting that mitochondrial ATP
310 synthase activity acts downstream of lysosome acidification to prevent protein aggregation
311 (Bohnert and Kenyon, 2017).

312 Next, we asked whether reduced lysosomal acidification in the RNAi-treated
313 hermaphrodites might be caused by an inability to localize the V-ATPase subunits to lysosomes,
314 as occurs in females. To test this, we subjected GFP::VHA-13-expressing animals to assay-pool
315 RNAi and screened for the presence of GFP::VHA-13 puncta (Figure S12C). The extent of
316 puncta formation was quantified by measuring the skewness (non-homogeneity) of the
317 GFP::VHA-13 signal at multiple locations within the most proximal oocyte. Hermaphrodites and
318 the empty-vector RNAi-treated animals demonstrated significantly higher skewness values than
319 did female oocytes, which exhibited diffuse GFP::VHA-13 localization (Figure 4B). All of the
320 knockdowns that blocked lysosome acidification showed reduced GFP::VHA-13 skewness,
321 albeit to varying degrees. While most knockdowns resulted in a marked reduction in GFP::VHA-
322 13 skewness, similar to the female, some genes involved in protein folding (*cct-1, cct-5*), RNA
323 processing (*ess-2, let-711*) and calcium ion transport (*itr-1, sca-1*) demonstrated intermediate
324 values of skewness, indicative of at least a reduction of GFP::VHA-13 localization (Figure 4B).

325 Similarly, the orphan-gene inhibitions demonstrated reduced GFP skewness, with several
326 candidates showing only intermediate effects (*kin-2, par-5, xpo-1, rmd-2, lgc-46, aco2, imb-1*)
327 (Figure S12B). As anticipated, neither of the two ATP synthase gene knockdowns affected
328 GFP::VHA-13 puncta formation (Figure 4B). Together these data support the model that the
329 failure of the knockdowns to acidify lysosomes is due, at least in part, to a failure to assemble
330 the lysosomal V-ATPase.
331

Figure 4

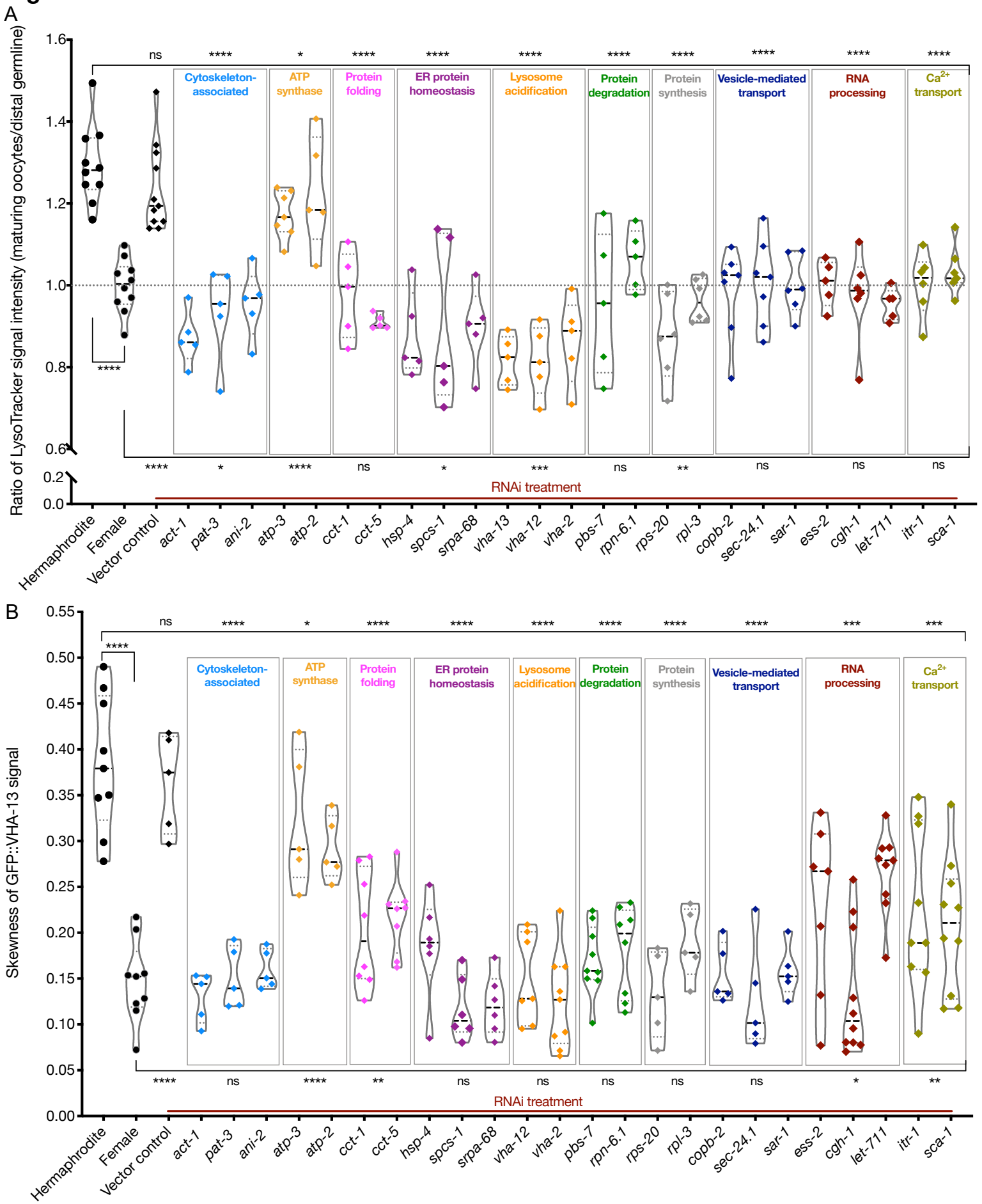
A
Ratio of LysoTracker signal intensity (maturing oocytes/distal germline)
1.6
1.4
1.2
1.0
0.8
0.6
0.2
0.0
ns
****
*
Cytoskeleton-associated
ATP synthase
Protein folding
ER protein homeostasis
Lysosome acidification
Protein degradation
Protein synthesis
Vesicle-mediated transport
RNA processing
Ca2+ transport
***
**
RNAi treatment
Hermaphrodite
Female
Vector control
act-1
pat-3
ani-2
atp-3
atp-2
cct-1
cct-5
hsp-4
spcs-1
srpa-68
vha-13
vha-12
vha-2
pbs-7
rpn-6.1
rps-20
rpl-3
copb-2
sec-24.1
sar-1
ess-2
cgh-1
let-711
itr-1
sca-1
B
Skewness of GFP::VHA-13 signal
0.55
0.50
0.45
0.40
0.35
0.30
0.25
0.20
0.15
0.10
0.05
0.00

Figure 4. Lysosome acidification and GFP::VHA-13 localization following knockdown of genes identified by the screen.

(A) LysoTracker staining in hermaphrodites (SA115) subjected to RNAi. The LysoTracker signal is represented as the ratio of proximal oocyte to distal germline staining. Staining ratios obtained from hermaphrodite (N2E) and female (CF4101) animals were used as controls (~1.3 and ~1.0, respectively). Each data point represents the average of values from three different locations in the most proximal oocyte of a single animal. The presence of GFP::RHO-1 aggregates in the same animals confirmed successful gene knockdown (not shown). (B) Analysis of GFP::VHA-13 localization, assessed by the degree of GFP skewness (inhomogeneity) in hermaphrodites (PHX1414) subjected to RNAi, and compared to control hermaphrodites and females (PHX1414 and CF4599). Each data point represents the average of ten skewness values from different regions within the first three proximal oocytes of a single animal. The presence of aggregates in GFP::RHO-1 animals (SA115) treated in parallel was used as a control to verify successful gene knockdown (not shown). For (A) and (B), Unpaired t-test with Welch's correction was used to determine the statistical significance. The top and bottom rows of significance indicators in each experiment compare the mean values from each process category to hermaphrodite and female animals, respectively. P values: $P > 0.05$ = n.s., $P \leq 0.05$ = *, $P \leq 0.01$ = **, $P \leq 0.001$ = *** and $P \leq 0.0001$ = ****.

332 *Two distinct, mysterious roles for mitochondria in protein aggregation.*

333 Mitochondria undergo a morphological and metabolic shift in response to signals from
334 sperm, a shift that is required for aggregate removal (Bohnert and Kenyon, 2017). Unfertilized
335 female oocytes exhibit a high mitochondrial membrane potential (ΔΨ) relative to hermaphrodite
336 oocytes or to female oocytes exposed to sperm by mating. Loss of the mitochondrial ATP
337 synthase, which discharges the proton gradient during the generation of ATP, elevates the ΔΨ
338 in hermaphrodites and causes protein aggregates to accumulate (Bohnert and Kenyon, 2017).
339 As expected, subunits from the mitochondrial ATP synthase complex (*atp-2, atp-3*) emerged
340 from the screen. Previously, we found that lysosomal V-ATPase activity was required for the
341 shift in mitochondrial membrane potential (Bohnert and Kenyon, 2017). To test the prediction
342 that our screen hits, which all inhibited lysosome acidification, would also block the ΔΨ switch,
343 we stained hermaphrodites with the dye DiOC6(3), whose signal is sensitive to ΔΨ. Again, to
344 control for dye uptake, we measured the ratio of DiOC6(3) staining intensities between proximal
345 oocytes and the distal syncytial germline. As predicted, all of the knockdowns prevented the ΔΨ
346 decrease in proximal hermaphrodite oocytes, with their mitochondria exhibiting ΔΨ values
347 similar to, or even higher than those of the distal germline (Figure 5A and S13A).

348 The observation that gene knockdowns from all the functional categories caused a
349 relatively high oocyte ΔΨ value prompted us to question whether a high mitochondrial
350 membrane potential might be necessary for protein aggregate accumulation. To test this, we
351 asked whether exposing females expressing germline GFP::RHO-1 to conditions that lower ΔΨ;
352 namely, to electron-transport chain (ETC) RNAi knockdowns, might reduce protein aggregation.
353 However, neither *cyc-1* nor *nuo-2* RNAi prevented females from accumulating aggregates, even
354 though ΔΨ was reduced (Figure 5B, S13B and S13C). Thus, a high mitochondrial membrane
355 potential is not a prerequisite for protein aggregation.

356 RNAi-inhibition of ATP synthase has been shown to reduce ATP levels in worms, as
357 does RNAi inhibition of electron transport (Dillin et al., 2002; Lee et al., 2003). To ask whether

358 inhibiting ATP synthase was likely to cause protein aggregation in hermaphrodites by limiting
359 ATP levels, we analyzed hermaphrodites subjected to ETC RNAi. The treatments reduced body
360 size and growth rate (data not shown), two known correlates of reduced ATP levels. However,
361 these perturbations did not cause protein aggregation in hermaphrodite oocytes (Figure 5B).
362 This finding suggests the interesting hypothesis that loss of ATP synthase causes aggregates to
363 accumulate in hermaphrodites not because it limits ATP levels, but for a different reason (see
364 Discussion).
365 Given the striking change in mitochondrial dynamics that takes place during oocyte
366 maturation, we were surprised that in our screen we recovered only one additional gene
367 encoding a mitochondrial-localized protein, *aco-2* (Krebs-cycle aconitase). We tested several
368 additional Krebs-cycle gene knockdowns (*pdha-1, idhg-1, ogdh-1, sucl-1,* and *sdhd-1*), and
369 found that α-ketoglutarate dehydrogenase (*ogdh-1*) and succinate dehydrogenase (*sdhd-1*)
370 RNAi also led to oocyte GFP::RHO-1 aggregation (Figure S13D). Notably, unlike ATP-synthase
371 inhibition, *aco-2* inhibition prevented lysosome acidification (Figure S12A), indicating that the
372 Krebs cycle and ATP synthase likely have distinct roles in the protein-aggregation pathway.
373

374 *ESCRT-complex genes are required for the clearance of protein aggregates.*

375 The direct mechanism by which protein aggregates are removed during oocyte
376 maturation is not known with certainty, although morphologically, the process resembles
377 lysosomal microautophagy (Bohnert and Kenyon, 2017). Microautophagy has not been
378 described previously in *C. elegans*; however, orthologs of genes encoding components of the
379 ESCRT machinery, which mediates microautophagy in yeast and mammals, are present (Sahu
380 et al., 2011; Williams and Urbé, 2007). We identified two ESCRT subunits (*vps-37* and *vps-54*)
381 in our primary screen, but they did not pass our initial validation cutoff (Table S3). To explore
382 the possibility that these were false negatives, we retested these RNAi clones along with RNAi
383 clones inhibiting additional ESCRT subunits (*tsg-101*, *vps-20* and *vps-28*). In these experiments,
384 the ESCRT subunits *vps-20*, *vps-28*, *vps-37*, and *vps-54* tested positive with subtle aggregation
385 phenotypes (although not observed in all animals tested) (Figure S14A), supporting the model
386 that aggregates are removed via microautophagy. Importantly, the degree of GFP::VHA-13
387 localization to puncta in these knockdowns was comparable to that of hermaphrodites (Figure
388 S14B, S14C), and they also permitted acidification of oocyte lysosomes (Figure 5C). Taken
389 together, these findings suggest that the ESCRT machinery operates downstream of V-ATPase
390 assembly and lysosome acidification to prevent aggregate accumulation.
391

A **Figure 5**

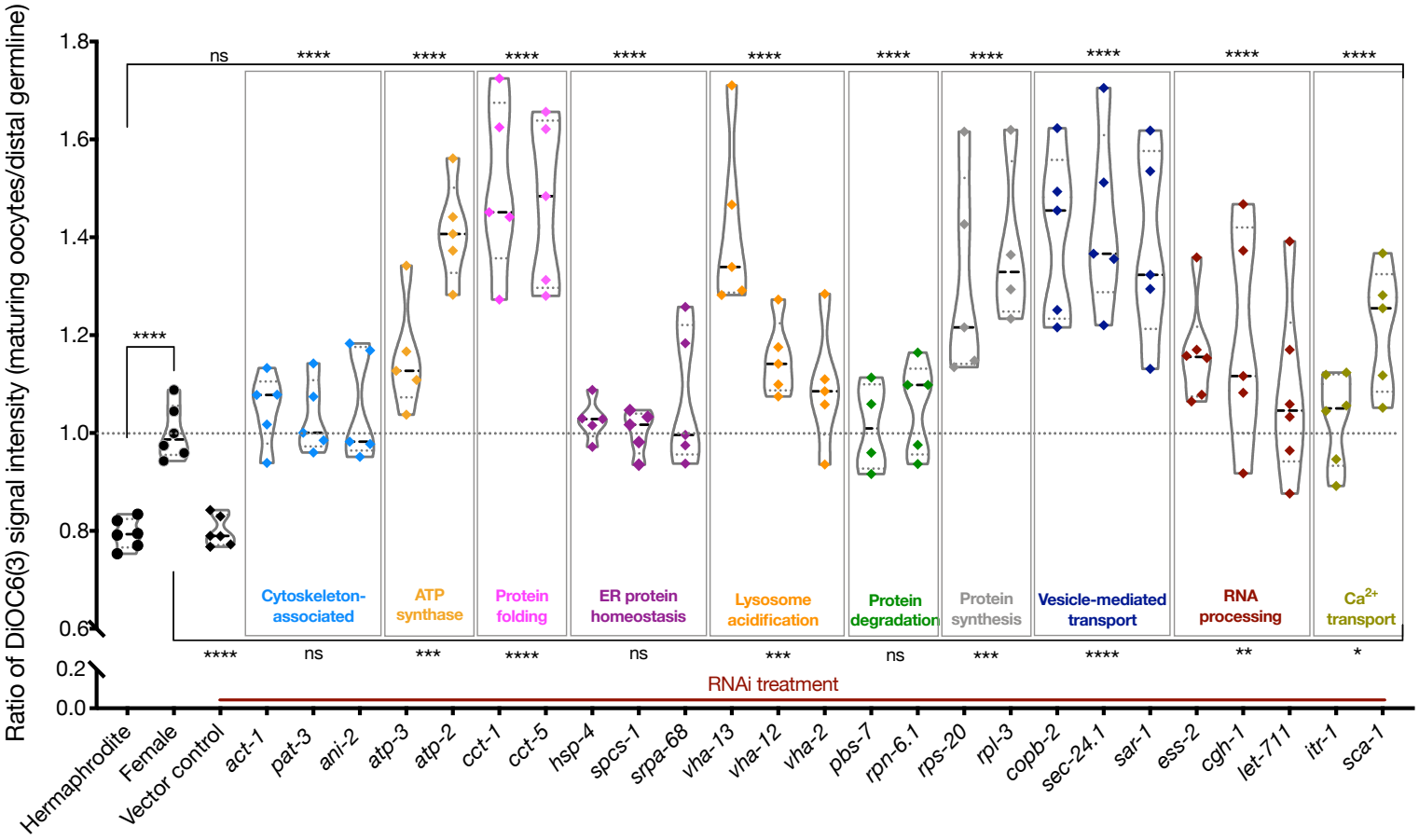
Ratio of DiOC6(3) signal intensity (maturing oocytes/distal germline)
1.8
1.6
1.4
1.2
1.0
0.8
0.6
0.2
0.0
ns
****
Cytoskeleton-associated
ATP synthase
Protein folding
ER protein homeostasis
Lysosome acidification
Protein degradation
Protein synthesis
Vesicle-mediated transport
RNA processing
Ca2+ transport
***
**
*
RNAi treatment
Hermaphrodite
Female
Vector control
act-1
pat-3
ani-2
atp-3
atp-2
cct-1
cct-5
hsp-4
spcs-1
srpa-68
vha-13
vha-12
vha-2
pbs-7
rpn-6.1
rps-20
rpl-3
copb-2
sec-24.1
sar-1
ess-2
cgh-1
let-711
itr-1
sca-1

B

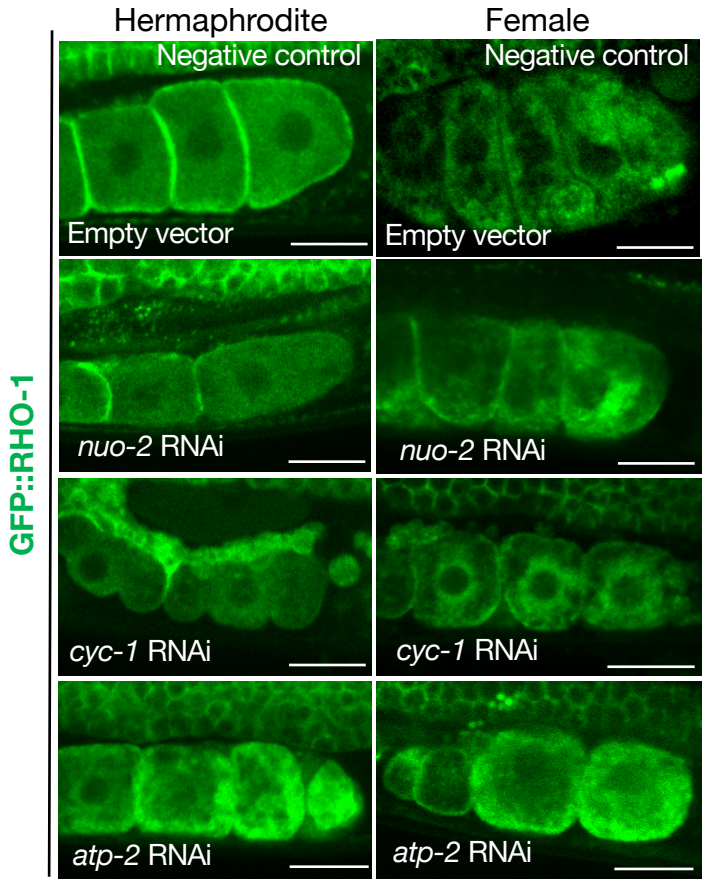
Hermaphrodite
Female
GFP::RHO-1
Negative control
Empty vector
nuo-2 RNAi
cyc-1 RNAi
atp-2 RNAi

C

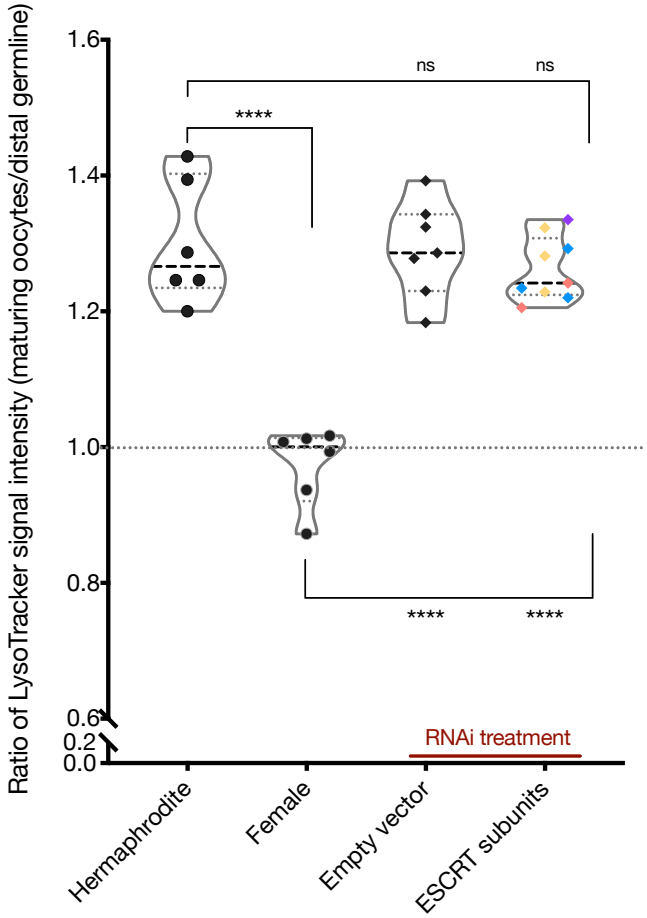
Ratio of LysoTracker signal intensity (maturing oocytes/distal germline)
1.6
1.4
1.2
1.0
0.8
0.6
0.2
0.0
ns
****
vps-20
vps-28
vps-37
vps-54
RNAi treatment
Hermaphrodite
Female
Empty vector
ESCRT subunits

Figure 5. Analysis of mitochondrial membrane potential and ESCRT-complex subunits

(A) Analysis of oocyte ΔΨ using DiOC6(3) staining in RNAi-treated hermaphrodites (OCF15), represented as the ratio of proximal oocyte to distal germline staining. Staining ratios obtained from N2E hermaphrodites (~0.8) and CF4101 females (~1) were used as controls for comparison. Each data point represents the average of values from three different locations in the most proximal oocyte of a single animal. When applicable, alteration in ER morphology was used as a control to determine successful gene knockdown in the same animals. The presence of GFP::RHO-1 aggregates in SA115 animals treated in parallel, was also used as an RNAi control (not shown). (B) Visualization of GFP::RHO-1 aggregates in oocytes of hermaphrodites (SA115) and females (CF4115) subjected to disruption of mitochondrial electron transport chain genes. Successful ETC disruption was confirmed by smaller body sizes, visible in the images and severely reduced brood sizes, similar to ATP synthase subunit knockdowns. Scale bars, 25 μm. (C) LysoTracker staining in hermaphrodites (SA115) subjected to ESCRT-complex RNAi, represented as the ratio of proximal oocyte to distal germline staining, and compared to hermaphrodites (N2E) and females (CF4101). Only animals exhibiting GFP::RHO-1 aggregates upon RNAi treatment (confirming knockdown; shown in Fig. S14A), were included in the quantification. For (A) and (C), unpaired t-test with Welch's correction was used to determine the statistical significance. The top and bottom rows of significance indicators in each experiment compare the mean values from each process category to hermaphrodite and female animals respectively. P values: $P > 0.05$ = n.s., $P \leq 0.05$ = *, $P \leq 0.01$ = **, $P \leq 0.001$ = *** and $P \leq 0.0001$ = ****.

392 *Mechanisms enhancing germline proteostasis also operate in the soma.*

393 Widespread proteostasis collapse is an inherent part of aging in *C. elegans* (Ben-Zvi et
394 al., 2009; David et al., 2010; Taylor and Dillin, 2011; Walther et al., 2015), and mechanisms that
395 extend lifespan invariably enhance cellular proteostasis. Understanding how the immortal germ
396 lineage maintains cellular quality and proteostasis across the generations could suggest new
397 ways to enhance proteostasis in the soma and delay organismal aging. Our lab and others have
398 shown that many endogenous proteins become insoluble with age and can form visible
399 aggregates when overexpressed with fluorescent tags (David et al., 2010; Huang et al., 2019;
400 Reis-Rodrigues et al., 2012; Roux et al., 2016). To visualize age-related protein aggregation, we
401 monitored the casein kinase subunit KIN-19, which forms insoluble aggregates in an age-
402 dependent manner in wild-type somatic tissues (David et al., 2010). To do this, we fluorescently-
403 tagged the endogenous *kin-19* gene specifically in the soma using split-wrmScarlet (Goudeau et
404 al., 2020a) (Table S2). To avoid interference from the bright intestinal autofluorescence, we
405 examined KIN-19::wrmScarlet in the head. The signal was mainly diffuse in young day-1 adults
406 but began to exhibit a striking punctate appearance as early as day-4 of adulthood (Figure 6A,
407 6B, S15A, S15B and S15C). To the best of our knowledge, this tool is the first used to visualize
408 age-dependent aggregation of an endogenously-expressed protein in *C. elegans*.

409 To ask whether the germline-proteostasis genes we identified in our screen might also
410 affect somatic protein aggregation, we screened our germline-aggregation 'assay pool' for gene
411 knockdowns that caused KIN-19 to aggregate prematurely in head tissues. We found that
412 multiple RNAi knockdowns that impaired lysosomal acidification in the germline induced
413 premature KIN-19::wrmScarlet aggregation in the soma, most notably RNAi of genes encoding
414 lysosomal V-ATPase subunits (*vha-12*, *vha-13*, *vha-16* and *vha-19*), but also genes that, in the
415 germline, were required for V-ATPase assembly (the actin gene *act-5* and the vesicle-mediated
416 ER-to-Golgi transport gene *copb-2*) (Figure 6C and 6D). We were not able to visualize lysosome
417 acidification in the head using LysoTracker, but these knockdowns did affect lysosome

418 acidification in the intestine, where the RNAi treatment led to fewer discrete acidic lysosome-
419 related organelles (LROs) thereby reducing the skewness of the LysoTracker signal (Figure 6E
420 and S16). We also recovered the proteasome subunits *pbs-7* and *rpn-6.1*, indicating a direct or
421 indirect role for proteasome function to maintain KIN-19 solubility in the aging soma (Figure 6C
422 and 6D).
423

Figure 6

A

Endogenous KIN-19::wrmScarlet$_{11}$ + somatic wrmScarlet$_{1-10}$

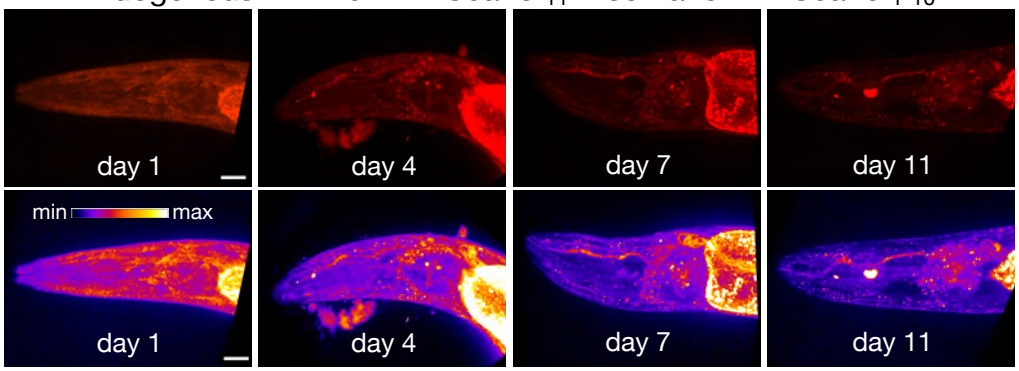

B

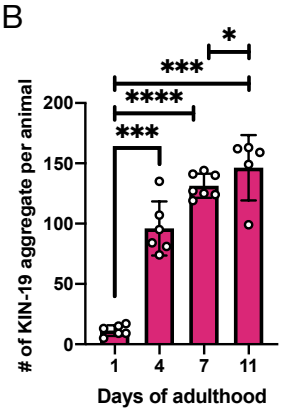

C

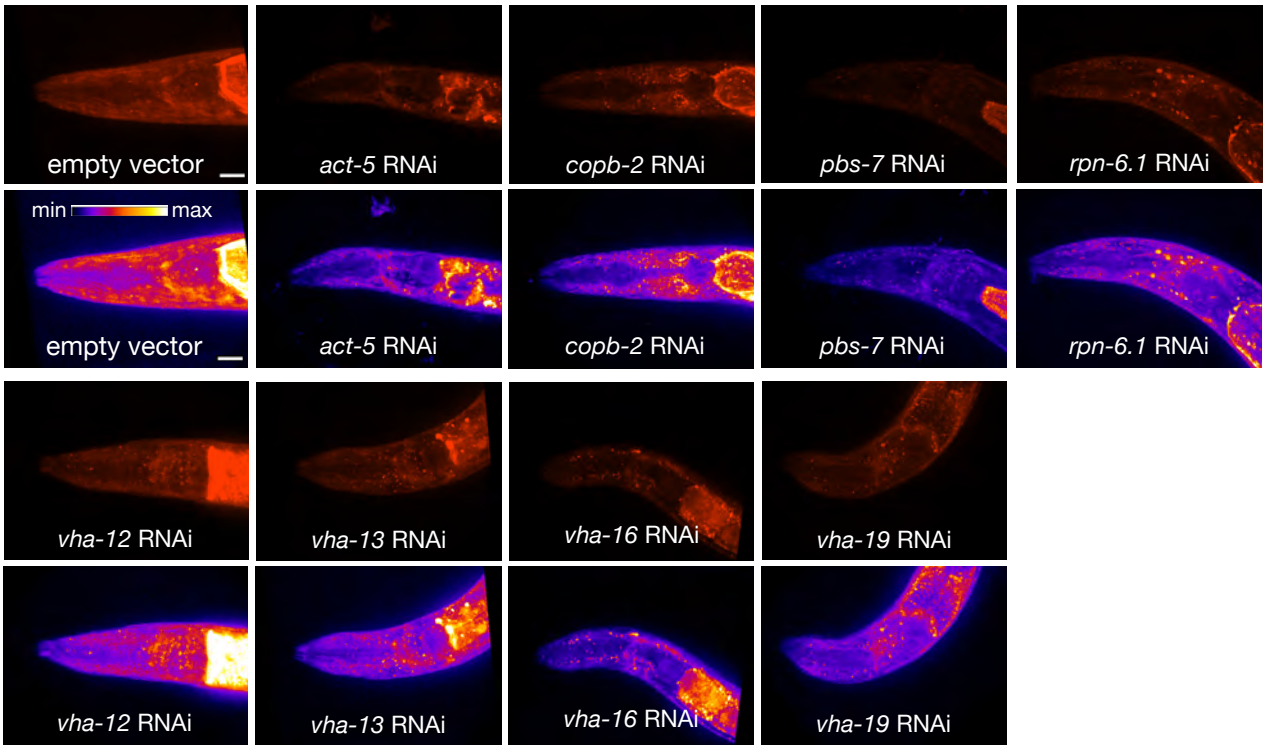

D

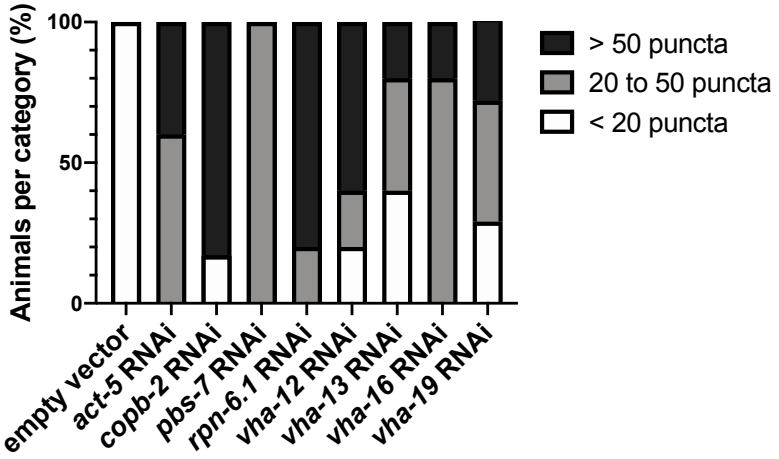

E

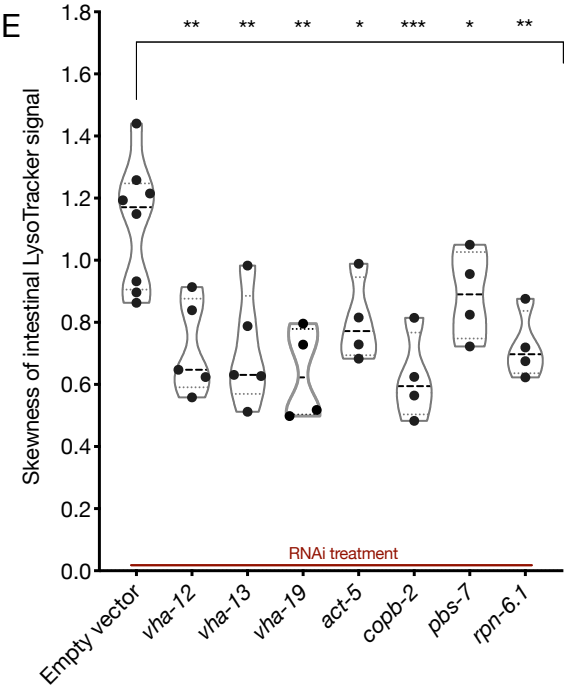

Figure 6. Analysis of protein aggregation and lysosome acidification in somatic tissues.

(A) Representative images of CF4609 animals expressing KIN-19::wrmScarlet$_{11}$ and somatic wrmScarlet$_{1-10}$ at days-1, 4, 7 and 11 of adulthood. Maximum intensity projections of 3D stacks are shown in red (upper panels), and also using an intensity scale (lower panels). Scale bars, 10 μm. (B) Quantification of KIN-19::wrmScarlet aggregates per animal in the head region. Unpaired t-test with Welch's correction was used to determine the statistical significance. *$P \leq 0.05$, ***$P \leq 0.001$ and **** $P \leq 0.0001$. (C) Representative images of CF4609 animals expressing KIN-19::wrmScarlet$_{11}$ and somatic wrmScarlet$_{1-10}$ subjected to RNAi or empty-vector negative control. Scale bars, 10 μm. (D) Quantification of fluorescent KIN-19 puncta in CF4609 animals subjected to RNAi or empty-vector control. (E) Skewness of the intestinal LysoTracker signal in SA115 animals subjected to RNAi (shown in Figure S16). Each data point represents the average of six independent skewness values from the anterior intestinal region, near the pharyngeal bulb, in a single animal. The simultaneous presence of GFP::RHO-1 aggregates in oocytes, was used as a control for successful gene knockdown in each animal (not shown). Unpaired t-test with Welch's correction was used to determine the statistical significance. P values: $P \leq 0.05$ = *, $P \leq 0.01$ = ** and $P \leq 0.001$ = ***.

Discussion

Sperm-derived signals that trigger oocyte maturation in *C. elegans* initiate a global change in oocyte structure and function, including the rapid removal of protein aggregates. A key step in aggregate removal is the acidification of lysosomes, which subsequently engulf the aggregates (Bohnert and Kenyon, 2017). In addition, mitochondria, which undergo morphological and metabolic changes in response to maturation signals, appear to play an important regulatory role, as inhibition of mitochondrial ATP synthase prevents the downshift in mitochondrial membrane potential normally triggered by sperm, and causes aggregates to form even when sperm are present (Bohnert and Kenyon, 2017). In this study, we identified a key role for a third organelle, the ER, in proteostasis renewal, and, using genetic and cell biological approaches, we deepened our understanding of all three organelles, the ER, lysosomes and mitochondria, in oocyte protein-quality control.

Limits of our genetic screen

To identify additional genes and processes involved in protein-aggregate metabolism in oocytes, we carried out a genome-wide screen for RNA-inhibitions that cause proteins to aggregate even in the presence of sperm; namely, in hermaphrodites. We expected to identify genes and processes that are directly involved in the sperm-dependent proteostasis switch, as well as genes that function more indirectly in protein homeostasis and cellular quality control. Many of the genes we recovered affected large multiprotein complexes, such as the ribosome and proteasome, making a compelling argument for these complexes influencing protein aggregation, directly or indirectly. However, we may have missed processes carried out by only one or a few genes if the corresponding RNAi bacteria were missing from the RNAi library or otherwise problematic; or if their inhibition produced milder protein-aggregation phenotypes, like the ESCRT genes that failed our initial, stringent validation tests (Table S3).

449 To place the genes into a proteostasis pathway, we asked which hallmarks of the sperm-
450 triggered aggregate-clearance pathway (lysosome acidification, mitochondrial membrane-
451 potential shift, etc.) were blocked by the knockdowns (Figure 7). An intrinsic limitation of this
452 strategy is that it only identifies the first role of a gene that acts in multiple steps in the process.
453 For example, because inhibiting the proteasome prevents degradation of the proximal-oocyte
454 cell-fate determinant GLD-1 (Bohnert and Kenyon, 2017; Kisielnicka et al., 2018), and inhibiting
455 various other chaperones prevents lysosome acidification, we cannot determine whether these
456 proteins also play a direct role in the process of aggregate clearance itself.
457

Figure 7

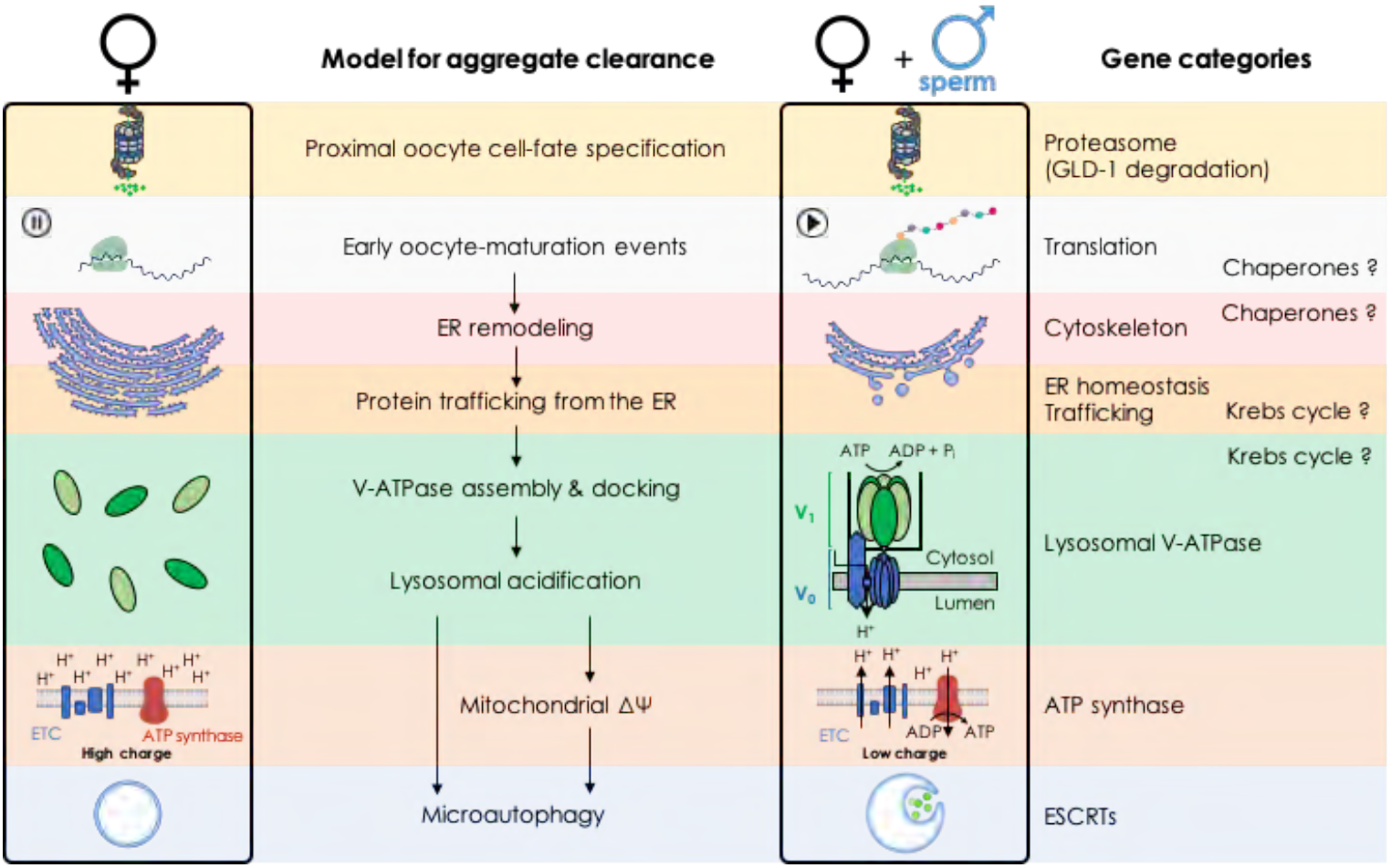

Figure 7. Model: Biological processes implicated in the clearance of protein aggregates during oocyte maturation.

458 *A role for the endoplasmic reticulum*

459 Many of the genes we identified affected the endoplasmic reticulum (Figure 7; Table 1). All of
460 these gene inhibitions prevented lysosome acidification, arguing that ER function influences
461 aggregate formation indirectly, acting at a relatively early step in the proteostasis pathway
462 (though ER function could be required again, at later stages, as well). Using transmission
463 electron microscopy and fluorescent reporters, we validated and extended previous
464 observations of ER reorganization during *C. elegans* oocyte maturation (Langerak et al., 2019).
465 We found that the ER assumes a stacked arrangement, spatially distinct from GFP::RHO-1
466 protein aggregates, in the proximal oocytes of females. Importantly, we found that neither the
467 ER stacking, nor protein-aggregate accumulation, were a consequence of long-term oocyte
468 quiescence ("oocyte aging"), as both were present as soon as female oocytes appeared during
469 development. When oocyte maturation was triggered by mating, the ER underwent a rapid
470 reorganization that preceded aggregate removal, consistent with a model that ER activity might
471 be a precondition for aggregate clearance.

472 The ER-gene inhibitions fell into two classes. First was a set of genes with known ER
473 functions that did not appear to affect ER morphology: *hsp-4* (BIP), *spcs-1* (signal peptidase),
474 and *srpa-68* (signal recognition protein). This finding argues that ER reorganization does not
475 require ER function itself. The second class did affect ER morphology, generally causing the ER
476 from hermaphrodites to exhibit a bright patchy appearance characteristic of (though not
477 necessarily identical to) that seen in female oocytes. Some of these gene knockdowns, such as
478 that of *itr-1,* which encodes the channel that releases calcium stored in the ER, likely cause both
479 sexes to adopt a female-specific, stacked ER morphology. In *C. elegans*, the major wave of
480 oocyte calcium release occurs after fertilization; this finding suggests that ER-dependent
481 calcium metabolism plays an important earlier role as well. Other RNAi knockdowns may simply
482 disrupt ER morphology more generally and might not identify genes that play an active role in
483 the oocyte proteostasis switch. For example, the actin cytoskeleton is known to influence ER

484 morphogenesis (Poteryaev et al., 2005), and we recovered a number of cytoskeletal gene hits.
485 Notably, TRiC-complex chaperonin genes fell into this class as well. The TRiC-complex
486 chaperonin can counteract protein aggregation directly; for example, by promoting correct
487 protein folding during protein synthesis. However, TRiC is known to assist in folding cytoskeletal
488 components including actin and tubulin (Llorca et al., 2000) and it was interesting to find that the
489 TRiC-complex genes we recovered, *cct-1* and *cct-5,* acted indirectly, by affecting ER
490 morphology and lysosome acidification. As mentioned above, the proteasome, too, affects
491 aggregate clearance indirectly. In general, it might be valuable to assay lysosome acidification
492 when analyzing the functions of these chaperone/chaperonin systems on the accumulation of
493 protein aggregates in other cellular systems, to test for the possibility of indirect effects. That
494 said, it is also possible that TRiC-complex and other chaperones act at multiple points in the
495 proteostasis pathway, with both indirect and direct effects on protein aggregation.
496 Finally, we identified several genes that, to our knowledge, were not previously known to
497 influence ER morphology; namely, *dlg-1*, *kin-2, and ttr-14* (Table 1). How these genes act,
498 directly or indirectly, to influence the ER could be interesting to explore in the future.
499
500 *Regulation of lysosome acidification*
501 A central goal of this study was to better understand how lysosomes are acidified during oocyte
502 maturation. To address this issue, we first generated functional, fluorescently-tagged V-ATPase
503 subunits expressed from their own loci. However, for reasons that we do not understand, none
504 of these proteins was visible in the germline. We then obtained a stable, single-copy MosSCI
505 strain in which *gfp::vha-13* was expressed from a germline-specific promoter. In these animals,
506 GFP::VHA-13 was visible, and we observed a striking sperm-dependent localization pattern. In
507 the presence of sperm (in hermaphrodites), GFP::VHA-13 was located on lysosomes; that is, it
508 assumed a punctate appearance that co-localized with LysoTracker signal. In the absence of
509 sperm (in unmated females), the protein was distributed throughout the cytoplasm (Figure 7).

510 The simplest interpretation of these findings is that signals from sperm trigger the localization of
511 GFP::VHA-13 to lysosomes, and that this localization enables lysosome acidification. In
512 principle, additional levels of control, such as translational repression of V-ATPase synthesis,
513 could operate as well, since our overexpressed construct could potentially override negative
514 regulators; though we observed no evidence of this with serially-diluted *gfp* RNAi treatments
515 that progressively reduced visible GFP::VHA-13 protein levels.

516 In yeast, peripheral, cytoplasmic V_1 subunits of the V-ATPase (such as VHA-13) localize
517 to lysosomes when the membrane-localized V_0 sector is trafficked there from the ER, where it is
518 assembled (Graham et al., 1998). Thus, we propose that the extensive rearrangement in ER
519 morphology triggered by sperm in *C. elegans* oocytes is coupled to movement of either pre-
520 existing or newly-synthesized membrane-localized V_0 subunits from the ER to lysosomes,
521 where they create docking sites for cytoplasmic, peripheral V_1 subunits. Consistent with this
522 idea, RNAi of the ER genes, as well as each of the three genes required for vesicle trafficking
523 from the ER to lysosomes, prevented GFP::VHA-13 localization to lysosomes, as did inhibiting
524 genes encoding the membrane-localized V-ATPase V_0 subunits. Unfortunately, our efforts to
525 observe the predicted sperm-activated movement of V_0 subunits from the ER to lysosomes were
526 thwarted by our inability to visualize either of two functional GFP-tagged V_0 subunits, even when
527 overexpressed using MosSCI technology. In the future, immuno-gold EM labeling of
528 endogenous V_0 subunits might enable this model to be tested more directly.

529 We note that an interesting puzzle remains unexplained: If the multi-subunit lysosomal
530 V-ATPase complexes are present in such low amounts in mature oocytes that they cannot be
531 seen when we fluorescently tag the endogenous *vha-13* gene, then why do they appear when
532 the tagged VHA-13 protein is overexpressed? How does the excess GFP::VHA-13 protein dock
533 onto lysosomes? Perhaps the ER supplies lysosomes with alternative docking sites for
534 unassembled V-ATPase subunits, or perhaps the stoichiometry change due to the excess
535 GFP::VHA-13 subunits triggers the production of entire new V-ATPase complexes that

536 incorporate the overexpressed GFP::VHA-13 subunits. This remains an unexplained but
537 intriguing mystery (see (Hughes and Gottschling, 2012)).
538 The gene knockdowns identified by the screen nearly all failed to acidify lysosomes,
539 reinforcing the central role of acidified lysosomes in clearing oocyte protein aggregates (Figure
540 7). Moreover, none of the knockdowns that failed to acidify lysosomes exhibited a punctate,
541 lysosomal GFP::VHA-13 pattern (Table 1). This finding suggests that V-ATPase activity may not
542 only be necessary but also sufficient for lysosome acidification; however, this interpretation
543 remains tentative, since we may simply have failed to identify the relevant genes in our screen.
544 Finally, several of the knockdowns from our screen did not appear to affect ER morphology (and
545 have not been reported to affect ER function), but did prevent V-ATPase localization, for
546 example *srab-17*, a chemosensory gene of the serpentine receptor class ab, and *lgc-46,*
547 involved in chloride ion transport (Table 1). How, directly or indirectly, these proteins might
548 influence V-ATPase localization and assembly is an interesting question to pursue in the future.
549
550 *Two Roles for Mitochondria*
551 Like the ER and lysosomes, mitochondria undergo morphological and functional changes during
552 *C. elegans* oocyte maturation. In response to sperm, the mitochondria of proximal oocytes
553 reduce their relatively high membrane potential and shift from a fragmented to a tubular
554 structure. Inhibiting mitochondrial ATP synthase preserves this high membrane potential even
555 when sperm are present and causes aggregates to accumulate. Injecting ADP, whose levels
556 would be expected to rise as maturing oocytes initiate protein synthesis and acidify lysosomes,
557 reduces the mitochondrial membrane potential in female oocytes, in an ATP-synthase
558 dependent fashion. Together these findings suggested the model that in the absence of sperm,
559 mitochondria are held in a quiescent, poised state that relaxes as metabolic activity and ATP
560 synthesis commences (Bohnert and Kenyon, 2017).

561 Whether *C. elegans* oocyte maturation is powered primarily by glycolysis or respiration is
562 unknown; however, in principle, the accumulation of protein aggregates caused by inhibiting
563 mitochondrial ATP synthase could reflect ATP limitation. However, if this were the case, then
564 inhibiting components of the electron transport chain should also cause protein aggregates to
565 accumulate in hermaphrodites, since this, too, limits ATP levels. However, though these
566 knockdowns affected body size, growth rates and brood size, this was not the case; ETC
567 knockdowns had no effect on protein aggregation. This unexpected finding suggests that ATP-
568 synthase knockdown prevents aggregate clearance not because of changes in ATP levels, but
569 instead either because a continuously high mitochondrial membrane potential acts like a
570 checkpoint to inhibit aggregate clearance (Figure 7), or because of another, unknown role of
571 ATP synthase in protein homeostasis.
572 Our screen revealed an additional requirement for mitochondria in protein homeostasis;
573 specifically, for Krebs cycle activity. Inhibiting mitochondrial aconitase (*aco-2)* produced a
574 different phenotype from inhibiting ATP synthase; namely, a failure to acidify lysosomes. Why
575 might this be? Again, the explanation seems unlikely to involve energy limitation, since inhibiting
576 ETC components or ATP synthase did not produce this phenotype. One possibility is that
577 inhibiting the Krebs cycle affects lysosome acidification by affecting redox potential, as several
578 Krebs cycle enzymes affecting protein aggregation (*ogdh-1* and *sdhd-1*) encode
579 dehydrogenases that produce the reducing agents NADH and $FADH_2$, and aconitase supplies
580 the substrate for another Krebs cycle dehydrogenase. Alternatively, other metabolites generated
581 via Krebs cycle intermediates could influence the events leading to lysosome acidification. It will
582 be interesting to explore this mechanism in the future.
583
584 *Microautophagy*
585 Previously, we observed lysosomes engulfing protein aggregates in a process reminiscent of
586 microautophagy (Bohnert and Kenyon, 2017). Before these observations, microautophagy had

587 not been described in *C. elegans.* In this study, using a candidate approach, we showed that
588 inhibiting ESCRT-complex members, which are known to mediate microautophagy in other
589 organisms, prevents aggregate accumulation in maturing *C. elegans* oocytes. Moreover, they
590 influence protein aggregation independently of lysosomal acidification, consistent with their
591 having a direct role. These findings strengthen the case that microautophagy is an active
592 proteostasis mechanism in *C. elegans,* and likely the mechanism by which aggregates are
593 cleared in response to oocyte-maturation signals (Figure 7).
594
595 *Implications for somatic proteostasis and aging*
596 Together our findings all point towards lysosomal acidification being a key, determinative event
597 in oocyte protein-aggregate clearance. Moreover, the screen hits that affected the lysosomal V-
598 ATPase and COPII (ER-to-lysosomal vesicle transport) had a striking ability to accelerate age-
599 dependent protein aggregation in somatic cells. Thus, the same mechanisms that enhance
600 oocyte proteostasis in the immortal germline likely enhance somatic proteostasis as well. These
601 findings may have implications for aging and longevity more broadly. In yeast, lysosomal acidity
602 declines with age, and overexpressing the yeast ortholog of the *C. elegans* V-ATPase gene
603 *vha-13* delays this decline and extends replicative lifespan (Hughes and Gottschling, 2012). In
604 worms, lysosome acidification also declines with age, and this decline is delayed in long-lived
605 mutants (Baxi et al., 2017; Sun et al., 2020). Whether increasing V-ATPase function might be
606 sufficient to extend lifespan in *C. elegans* is unclear, but overproduction of the transcription
607 factor HLH-30/TFEB, which augments many lysosomal functions, has been shown to do so
608 (Lapierre et al., 2013; O'Rourke and Ruvkun, 2013), and in mammals, similar perturbations slow
609 the aging of the immune system (Zhang et al., 2019).
610 In summary, a genetic screen for proteostasis enhancers in the immortal germ lineage
611 has revealed a landscape of interconnected processes, spanning protein translation,
612 cytoskeletal dynamics, Krebs cycle activity, ER activation and vesicle transport, that together

613 enable lysosome acidification and clearance of protein aggregates during oocyte maturation.
614 Lysosomal acidification maintains proteostasis in the aging soma as well. In addition to raising
615 many new questions for future investigations, our findings support a growing body of evidence
616 that interventions that rejuvenate lysosomal activity during aging might yield new ways to
617 increase human health and longevity.
618
619

620 **Acknowledgements:**
621 We thank colleagues in the Kenyon lab and at Calico Life Sciences for advice and discussion,
622 and Daniel Gottschling and Calvin Jan for comments on the manuscript. Special thanks to
623 Andrew Dillin (University of California, Berkeley) for sharing his transmission electron
624 microscopy resources, and Peichuan Zhang for help with converting the RNAi collection format.
625 We thank Robert Keyser for help with liquid handling robotics for the primary screen, and Kayley
626 Hake for suggesting skewness as a way to capture aggregate formation in microscopy images.
627 Peichuan Zhang and Rex Kerr helped to analyze somatic KIN-19 aggregation. We thank Di
628 Chen for sharing the DCL565 and DCL569 strains. Some *C. elegans* strains were provided by
629 the CGC, which is funded by NIH Office of Research Infrastructure Programs (P40 OD010440).
630 The endogenously tagged V-ATPase *C. elegans* strains were generated by SunyBiotech,
631 China. Some illustrations in Figures 1 and 7 were created with BioRender.com. The study was
632 supported by Calico Life Sciences and David H. Hall was supported by NIH OD010943.
633
634

635 **Author contributions:**
636 Ma.S and J.G executed all experiments with the exception of transmission electron microscopy,
637 which was performed by Me.S, in Andrew Dillin's laboratory. D.H.H provided advice for the TEM

638 experiments and helped in the interpretation of the TEM images. K.A.B provided valuable inputs
639 in the early stages of the project and contributed to the ER and ETC analysis. M.I. provided help
640 and advice for fluorescence microscopy experiments and data analysis. The research and
641 analysis was designed by Ma.S, J.G and C.K, who also prepared the final manuscript.
642
643
644 **Materials and Methods:**
645 ***C. elegans* strains and maintenance**
646 All strains used in this study are listed in Table S2. Hermaphrodites expressing germline
647 transgenes were maintained at 25°C to delay silencing. Mutants carrying the thermosensitive,
648 feminizing *fem-1(hc17ts*) allele, which causes cells that would normally become sperm instead
649 to become oocytes, were maintained at the permissive temperature of 15°C and moved to 25°C
650 for feminization prior to hatching, or at the L1 stage. Animals were grown under standard
651 laboratory conditions (Brenner, 1974) and maintained on Nematode Growth Medium (NGM)
652 seeded with OP50 bacteria, unless otherwise indicated.
653
654 **Generation of *C. elegans* strains**
655 **a. Strain generation: genetic crosses.**
656 The following *C. elegans* strains were created by standard genetic crosses: CF4542 *fem-*
657 *1(hc17ts) IV; ocfIs2[Ppie-1:mCherry::sp12::pie-1 3'UTR, Cbr-unc-119(+)]*, CF4552 *tjIs1[Ppie-*
658 *1::gfp::rho-1, Cbr-unc-119(+)]; ocfIs2 [Ppie-1:mCherry::sp12::pie-1 3'UTR, Cbr-unc-119(+)]*,
659 CF4557 *fem-1(hc17ts) IV; tjIs1[Ppie-1::gfp::rho-1, Cbr-unc-119(+)]; ocfIs2 [Ppie-*
660 *1:mCherry::sp12::pie-1 3'UTR, Cbr-unc-119(+)]*, CF4559 *zuIs45[Pnmy-2::nmy-2::gfp, Cbr-unc-*
661 *119(+)] V; ocfIs2 [Ppie-1:mCherry::sp12::pie-1 3'UTR, Cbr-unc-119(+)]*, CF4560 *fem-1(hc17ts)*
662 *IV; zuIs45[Pnmy-2::nmy-2::gfp, Cbr-unc-119(+)] V; ocfIs2 [Ppie-1:mCherry::sp12::pie-1 3'UTR,*

663 *Cbr-unc-119(+)]* and CF4599 *sybSi35[Ppie-1::gfp::vha-13::vha-13 3'UTR + Cbr-unc-119(+)] II;*
664 *unc-119(ed3/+) III; fem-1(hc17ts) IV*.

665 **b. Strain generation: Mos1-mediated single-copy insertion.**
666 The strains PHX1414 *sybSi35[Ppie-1::gfp::vha-13::vha-13 3'UTR + Cbr-unc-119(+)] II; unc-*
667 *119(ed3) III* and PHX2690 *sybIs2690[Ppie-1::vha-7::wrmScarlet::vha-7 3'UTR, Cbr-unc-119(+)]*
668 *I; unc-119(ed3) III* were generated by SunyBiotech using MosSCI services.
669 **c. Strain generation: CRISPR/Cas9-triggered homologous recombination**.
670 $WrmScarlet_{11}$ was introduced at the C-terminus of KIN-19 using CRISPR/Cas9 and single-
671 stranded oligodeoxynucleotide template (ssODN) in the strain CF4582 expressing $wrmScarlet_{1-}$
672 $_{10}$ in somatic tissues (driven by the *eft-3* promoter and *unc-54* 3'UTR), to obtain the strain
673 CF4609. CRISPR insertion of $wrmScarlet_{11}$ was performed following published protocols
674 (Goudeau et al., 2020a; Paix et al., 2016, 2015). Briefly, ribonucleoprotein complexes (protein
675 Cas9, tracrRNA, crRNA) and ssODN were microinjected into the gonad of young adults using
676 standard methods (Evans, 2006). Injected worms were singled and placed at 25ºC overnight.
677 The crRNA and ssODN template sequences used to generate $wrmScarlet_{11}$ knock-in at the C
678 terminus of *kin-19* are the following:
679 *ssDNA_kin-19C:*
680 ACAGGGAGCTACCGTTCCATCAGCTGGAGTTCCAGCTGGAGTTGCACCAGGAGGAACTAC
681 TCCACAGGGAGGAGGATCCTACACCGTCGTCGAGCAATACGAGAAGTCCGTCGCCCGTCA
682 CTGCACCGGAGGATAAgacgttttgttgccgtcctgaggctttttaatccaaaaaagcccatgttaaatcatgtactatc
683 *kin-19_C_crRNA:* GGCAACAAAACGTCTTACTG(TGG).
684 KIN-19::$wrmScarlet_{11}$ integrants were identified by screening for fluorescent progeny in the
685 progeny of injected worms.
686 Strains PHX731 *vha-13(syb731[wrmScarlet::vha-13]) V*, PHX1049 *vha-13(syb1049[gfp::vha-*
687 *13]) V*, PHX1198 *ieSi65[sun-1p::TIR1::sun-1 3'UTR + Cbr-unc-119(+)] II; unc-119(ed3) III; vha-*

688 *11(syb1198[vha-11::gfp::degron]/+) IV*, PHX1363 *vha-4(syb1363[wrmScarlet::vha-4]/+) II*, and
689 PHX1317 *vha-7(syb1317[vha-7::wrmScarlet]) IV* were generated by SunyBiotech using CRISPR
690 services for the Kenyon lab.
691 **d. Nucleic acid reagents.** Synthetic nucleic acids were purchased from Integrated DNA
692 Technologies (IDT). For $wrmScarlet_{11}$ knock-in, a 200-mer HDR template was ordered in
693 ssODN form (synthetic single-stranded oligodeoxynucleotide donors) from IDT.
694

695 ## RNA interference

696 Unless otherwise indicated, RNA interference was initiated in the early L4 larval stage, prior to
697 formation of oocytes but following much of development. One exception was *fem-1* RNAi, which
698 was initiated at hatching to ensure feminization. RNAi-bacterial feeding was initiated and
699 maintained for 36-40 hours prior to imaging to allow sufficient time for knockdown.
700

701 **a. Genome-wide screen**

702 The Ahringer *C. elegans* RNAi collection containing 18,225 bacterial clones, targeting around
703 87% of currently annotated *C. elegans* genes (Source BioScience), was used for screening. A
704 workflow for screening in liquid (Lehner et al., 2006) was modified suitably for our needs. For a
705 single 96-well plate, SA115 (GFP::RHO-1) hermaphrodites were grown on NGM plates seeded
706 with thick OP50 lawns (from 2 medium sized plates) for ~4 days to obtain a high density of
707 healthy and gravid young adults.
708 **Day 1:** Animals were subjected to standard bleaching and the eggs were washed thoroughly
709 and then incubated in M9 buffer overnight at 20°C on a rotating mixer to obtain synchronized
710 L1-arrested animals.
711 **Day 2:** L1 animals were transferred to NGM plates spotted with HT115 bacteria and incubated
712 24-28 hrs at 25°C to reach the early L4 stage. The RNAi-library plate was aseptically replicated

713 into deep well plates (96-well, square; Greiner Bio-One) containing 1 mL LB (with 25 µg/ml
714 carbenicillin and 12.5 µg/ml tetracycline) per well. Positive (*vha-13* and *atp-2*) and negative
715 (empty L4440 vector) controls were inoculated manually into blank wells if available, or into
716 wells on a separate control plate. The cultures were grown overnight at 37°C with shaking (185
717 rpm).
718 **Day 3:** Fresh media (1 mL LB with 25 µg/ml carbenicillin) was added to the wells and incubated
719 at 37°C, 155 rpm for 2 hrs. Subsequently, 4 mM isopropyl β-d-1-thiogalactopyranoside (IPTG;
720 Promega) was added to each RNAi well for induction of dsRNA synthesis and plates were
721 incubated for 3-4 hours at 30°C and 155 rpm. Synchronized L4 animals were washed off the
722 HT115 plates with M9 and resuspended in NGM broth (with 25 µg/ml carbenicillin and 1 mM
723 IPTG). This worm suspension (20 µL, ~10-15 animals) was added to each well of a Cellvis flat-
724 bottom glass plate with high performance #1.5 cover glass. The deep-well plate with dsRNA-
725 induced RNAi bacteria was centrifuged and the cells were resuspended in the same NGM broth
726 as the worms. 35 µL of each cell suspension was transferred into the corresponding well of the
727 Cellvis plate already seeded with L4 animals for bacterial RNAi feeding. The feeding plate was
728 incubated at 20°C, 155 rpm with adequate humidity in the shaker to prevent worms from settling
729 or drying out.
730 **Day 5:** After checking the for presence of adults with fully developed germlines, 25 mM sodium
731 azide (Sigma-Aldrich) was added to each well and the plate was subjected directly to imaging
732 on a spinning-disk confocal microscope. Typically, ~6 such 96-well plates were handled
733 simultaneously in a given round of screening. The presence of aggregates in 50% or more
734 animals for a specific RNAi condition was considered a hit.
735
736 *Notes:* The ability to automate image acquisition was complicated by a combination of low
737 GFP::RHO-1 reporter expression and the close apposition of gonads with the intestine, an
738 organ with significant autofluorescence. The density of animals and temperature of incubation

739 determine developmental rate and were optimized by multiple pilot trials. Liquid handling was
740 performed using Multidrop Combi from Thermo Scientific (initial inoculation of RNAi bacteria;
741 Day 2) and Agilent Bravo (resuspension and mixing of worms and induced bacteria; Day 3).
742 Following the validation rounds, the identities of the RNAi clones emerging from the screen
743 were verified by sequencing (Quintara Biosciences). Investigators were blinded to identity of
744 RNAi clones, except controls, during screening.
745
746 **b. RNAi feeding on agar plates**
747 Individual cultures were inoculated in tubes containing 1mL LB (with 25 µg/ml carbenicillin and
748 12.5 µg/ml tetracycline) and incubated at 37°C with shaking (200 rpm). The cultures were
749 diluted 1:10 in fresh LB containing only carbenicillin and allowed to grow for a further 2 hrs, after
750 which IPTG was added (4 mM) and tubes moved to a 30°C shaker for dsRNA induction (3-4
751 hours). Induced cultures were spotted on NGM plates containing 50 µg/ml carbenicillin and 2
752 mM IPTG and the bacterial lawn was allowed to grow for 24-36 hrs at 30°C, prior to introducing
753 synchronized L4 animals.
754
755 **c. Somatic KIN-19 protein-aggregation RNAi screen**
756 KIN-19::wrmScarlet-expressing CF4609 animals were grown from a synchronized population of
757 L1 animals on HT115 bacteria until they reached the L3 stage and then were transferred to
758 plates seeded with RNAi bacteria until they reached day-2 of adulthood. The animals' heads
759 were imaged by confocal microscopy. Z-stacks were analyzed using ImageJ (Fiji); image
760 manipulations consisted of maximum intensity projections. The images of KIN-19::wrmScarlet
761 puncta were quantified by the investigator who acquired the images (Figure 6B), as well as by
762 three blinded investigators (Figure S15).
763
764

765 **Fluorescence Microscopy**

766 Confocal fluorescence images were acquired on a Nikon Eclipse Ti CSU-X1 equipped with 405,
767 488, 561 and 640 nm lasers. Emission was collected through 455/50, 525/36, 605/70 or 700/75
768 nm filters on an Andor iXon Ultra EMCCD camera, using the NIS-Elements software. Images
769 were visualized using ImageJ Fiji. Maintenance and selection of transgenic worms expressing
770 fluorescent markers were performed using a Leica M165 FC fluorescent stereo microscope
771 equipped with a Sola SE-V light source. Photobleaching and wide-field experiments were
772 performed using a Leica TIRF microscope equipped with an infinity scanner, using 488 nm laser
773 excitation. Emission was collected through a GFP-T filter cube on a Hamamatsu ORCA-Flash4
774 camera.

775

776 **a. Preparing worms for microscopy**

777 Worms imaged in 96-well plates were immobilized by adding sodium azide to the liquid medium
778 at a concentration of 25 mM (except when measuring mitochondrial ΔΨ, where the medium was
779 carefully removed, and animals immobilized with levamisole). For all other experiments, animals
780 were picked from plates and placed in a drop of 2 mM levamisole (Sigma) on a 4% agarose pad
781 resting on a glass slide, and then secured with a coverslip.

782

783 **b. Dye staining**

784 For experiments involving several different RNAi-knockdown conditions, RNAi feeding was set
785 up similar to the screen workflow. The dyes LysoTracker Red DND-99 and DiOC6(3) (both from
786 Life Technologies) were added to the liquid NGM at 2 μM concentration prior to resuspension of
787 dsRNA-induced RNAi-bacterial cells. After addition of synchronized L4 animals, feeding and dye
788 uptake were allowed to proceed at 20°C for 36-40 hrs. The 96-well feeding plates were
789 protected from light during this time. The plate was centrifuged, bacterial suspensions were
790 carefully washed off, and the animals were resuspended in fresh M9 buffer for imaging. For

791 experiments involving fewer knockdown conditions or pairwise comparisons between
792 hermaphrodites and females, the dye-feeding was performed on NGM Agar plates as described
793 previously (Bohnert and Kenyon, 2017).
794 To analyze lysosome acidification in maturing oocytes, the ratio of signal intensities between
795 proximal oocytes and the distal germline were calculated. In case of intestinal LysoTracker
796 staining, signal intensities were not measured due to highly variable dye uptake and staining;
797 and signal skewness (inhomogeneity) was measured instead. In both cases, multiple regions of
798 oocytes or the anterior intestine were sampled for intensity or skewness values; and averaged
799 for a single animal.
800

801 **Mating experiments**

802 An individual female animal was immobilized on an agarose pad using 2 mM levamisole, and
803 the reporter of interest was imaged in the anterior gonad arm. Levamisole was washed off
804 immediately, and the animal was introduced to an NGM plate containing young CB1490 male
805 animals in a small spot of OP50 bacteria (5 males:1 female). The interactions were monitored
806 using a benchtop stereo microscope and when mating occurred, the female was transferred
807 immediately to the agarose pad and imaged again, ensuring that the same oocytes were
808 visualized before and after mating. Successful mating events were tracked by gonadal sheath
809 contractions in response to sperm and subsequently confirmed by successful ovulation.
810 Changes within individual oocytes upon mating were monitored up to 90 minutes at 10-minute
811 intervals. An identical procedure was performed for control females, except for exposure to
812 males. Specific regions within proximal oocytes of control female animals were compared at all
813 time points to determine the extent of signal intensity change due to photobleaching, with
814 increasing time (Figure S6B). In addition, regions of the distal germline were also monitored in
815 mated animals (data not shown) to verify that the disappearance of the signal representing ER
816 clusters and protein aggregates was not due to photobleaching.

817 **KIN-19::wrmScarlet aggregate accumulation in somatic tissues**

818 A synchronized population of KIN-19::wrmScarlet-expressing CF4609 animals were grown on
819 OP50 from L1 at 20°C. Worms were transferred every other day to freshly-seeded NGM plates
820 to remove progeny. Worms were imaged by confocal microscopy at day-1, day-4, day-7 and
821 day-11 of adulthood.

822

823 **Transmission electron microscopy**

824 N2E hermaphrodites and *fem-1(hc17ts)* females were cultured for five generations at 15°C
825 without starvation or contamination at any point. Animals from 12 small plates of each strain
826 were bleached, and the synchronized eggs were collected and washed thoroughly in M9 and
827 strained through 40 µm strainers to remove adult carcasses. Eggs were then resuspended in
828 fresh M9 and incubated at 25°C overnight on a rotating mixer. Synchronized L1 animals were
829 moved to NGM plates seeded with OP50 and incubated at 25°C (~50 animals per plate). Newly-
830 developed day-1 adults were further processed according to standard *C. elegans* TEM
831 techniques (Hall et al., 2012). Briefly, the animals were loaded into 100 µm-deep specimen
832 carriers and high-pressure frozen in a Bal-tec HPM (approximately 20 worms per carrier). After
833 freezing, the carriers were transferred to vials containing Freeze Substitution (FS) media (1%
834 OsO4 and 0.1% uranyl acetate in acetone), while still submerged in liquid N_2. Frozen samples
835 were slowly warmed to approximately -15°C while being agitated on a rotating platform (adapted
836 from (McDonald and Webb, 2011)). Following freeze substitution, samples were infiltrated with
837 Epon Resin/Acetone series [25% Resin (1hr), 50% Resin (1hr), 75% Resin (overnight), 100%
838 resin (1hr), 100% resin (1hr) and the resin from last step replaced with fresh resin for
839 embedding] and subjected to polymerization at 60°C for 48 hrs. For staining, thin sections (70
840 nm thick) were cut on an ultramicrotome, picked up on Formvar-coated 50 mesh grids and post-

841 stained for 7 min in 2% uranyl acetate (aq), followed by 7 min in lead citrate. Images were
842 acquired on a Tecnai 12 Transmission Electron Microscope.
843

844 **Data analysis and statistics**

845 ImageJ Fiji was used to quantify and analyze attributes from image data, and images from a
846 given experimental set were scaled and processed identically for comparison. Preparation of
847 graphs and statistical analyses were performed using GraphPad Prism 8. Statistical tests used
848 to determine significance and p-values are described in the figure legends of each experiment.
849 No statistical methods were used to predetermine sample sizes. Investigators were blinded to
850 identity of RNAi clones (except for controls) while imaging in 96-well plates.
851
852

853 **References:**

854 Baxi K, Ghavidel A, Waddell B, Harkness TA, de Carvalho CE. 2017. Regulation of lysosomal
855 function by the daf-16 forkhead transcription factor couples reproduction to aging in
856 caenorhabditis elegans. *Genetics*. doi:10.1534/genetics.117.204222
857 Ben-Zvi A, Miller EA, Morimoto RI. 2009. Collapse of proteostasis represents an early molecular
858 event in Caenorhabditis elegans aging. *Proc Natl Acad Sci U S A*.
859 doi:10.1073/pnas.0902882106
860 Bluemink JG, Hage WJ, van den Hoef MH, Dictus WJ. 1983. Freeze-fracture electron
861 microscopy of membrane changes in progesterone-induced maturing oocytes and eggs of
862 Xenopus laevis. *Eur J Cell Biol*.
863 Bohnert KA, Kenyon C. 2017. A lysosomal switch triggers proteostasis renewal in the immortal
864 C. Elegans germ lineage. *Nature* **551**:629–633. doi:10.1038/nature24620
865 Brenner S. 1974. The genetics of Caenorhabditis elegans. *Genetics*.

866 Carroll J, Jones KT, Whittingham DG. 1996. Ca2+ release and the development of Ca2+
867 release mechanisms during oocyte maturation: A prelude to fertilization. *Rev Reprod*
868 **1**:137–143. doi:10.1530/ror.0.0010137
869 Charbonneau M, Grey RD. 1984. The onset of activation responsiveness during maturation
870 coincides with the formation of the cortical endoplasmic reticulum in oocytes of Xenopus
871 laevis. *Dev Biol*. doi:10.1016/0012-1606(84)90177-5
872 Crittenden SL, Troemel ER, Evans TC, Kimble J. 1994. GLP-1 is localized to the mitotic region
873 of the C. elegans germ line. *Development* **120**:2901–2911.
874 David DC, Ollikainen N, Trinidad JC, Cary MP, Burlingame AL, Kenyon C. 2010. Widespread
875 protein aggregation as an inherent part of aging in C. elegans. *PLoS Biol* **8**:47–48.
876 doi:10.1371/journal.pbio.1000450
877 Dillin A, Hsu AL, Arantes-Oliveira N, Lehrer-Graiwer J, Hsin H, Fraser AG, Kamath RS, Ahringer
878 J, Kenyon C. 2002. Rates of behavior and aging specified by mitochondrial function during
879 development. *Science (80-)*. doi:10.1126/science.1077780
880 Evans T. 2006. Transformation and microinjection. *WormBook*. doi:10.1895/wormbook.1.108.1
881 Fan W, Waymire KG, Narula N, Li P, Rocher C, Coskun PE, Vannan MA, Narula J, MacGregor
882 GR, Wallace DC. 2008. A mouse model of mitochondrial disease reveals germline
883 selection against severe mtDNA mutations. *Science (80-)*. doi:10.1126/science.1147786
884 FitzHarris G, Marangos P, Carroll J. 2007. Changes in endoplasmic reticulum structure during
885 mouse oocyte maturation are controlled by the cytoskeleton and cytoplasmic dynein. *Dev*
886 *Biol* **305**:133–144. doi:10.1016/j.ydbio.2007.02.006
887 Francis R, Barton M, Kimble J, Schedl T. 1995. gld-1, a tumor suppressor gene required for
888 oocyte development in Caenorhabditis elegans. *Genetics* **139**:579–606.
889 Fredriksson Å, Johansson Krogh E, Hernebring M, Pettersson E, Javadi A, Almstedt A, Nyström
890 T. 2012. Effects of aging and reproduction on protein quality control in soma and gametes
891 of Drosophila melanogaster. *Aging Cell*. doi:10.1111/j.1474-9726.2012.00823.x

892 Gawriluk TR, Hale AN, Flaws JA, Dillon CP, Green DR, Rucker EB. 2011. Autophagy is a cell
893 survival program for female germ cells in the murine ovary. *Reproduction*.
894 doi:10.1530/REP-10-0489
895 Goudeau J, Aguilaniu H. 2010. Carbonylated proteins are eliminated during reproduction in C.
896 elegans. *Aging Cell* **9**:991–1003. doi:10.1111/j.1474-9726.2010.00625.x
897 Goudeau J, Paw J, Savy L, Leonetti MD, York A, Kenyon C, Ingaramo M. 2020a. Split-
898 wrmScarlet and split-sfGFP: tools for faster, easier fluorescent labeling of endogenous
899 proteins in Caenorhabditis elegans. *bioRxiv*. doi:10.1101/2020.07.02.185249
900 Goudeau J, Samaddar M, Bohnert KA, Kenyon C. 2020b. Addendum: A lysosomal switch
901 triggers proteostasis renewal in the immortal C. elegans germ lineage. *Nature* **580**:2020.
902 doi:10.1038/s41586-020-2108-0
903 Graham LA, Hill KJ, Stevens TH. 1998. Assembly of the Yeast Vacuolar H+-ATPase Occurs in
904 the Endoplasmic Reticulum and Requires a Vma12p/Vma22p Assembly Complex. *J Cell*
905 *Biol* **142**:39–49.
906 Hall DH, Hartwieg E, Nguyen KCQ. 2012. Modern Electron Microscopy Methods for C.
907 elegansMethods in Cell Biology. Academic Press Inc. pp. 93–149. doi:10.1016/B978-0-12-
908 394620-1.00004-7
909 Huang C, Wagner-Valladolid S, Stephens AD, Jung R, Poudel C, Sinnige T, Lechler MC,
910 Schörit N, Lu M, Laine RF, Michel CH, Vendruscolo M, Kaminski CF, Schierle GSK, David
911 DC. 2019. Intrinsically aggregation-prone proteins form amyloid-like aggregates and
912 contribute to tissue aging in caenorhabditis elegans. *Elife*. doi:10.7554/eLife.43059
913 Hubbard EJA, Greenstein D. 2005. Introduction to the germ line. *WormBook*.
914 doi:10.1895/wormbook.1.18.1
915 Huelgas-Morales G, Greenstein D. 2018. Control of oocyte meiotic maturation in C. elegans.
916 *Semin Cell Dev Biol*. doi:10.1016/j.semcdb.2017.12.005
917 Hughes AL, Gottschling DE. 2012. An early age increase in vacuolar pH limits mitochondrial

918 function and lifespan in yeast. *Nature* **492**:261–265. doi:10.1038/nature11654
919 Hunter N. 2017. Oocyte Quality Control: Causes, Mechanisms, and Consequences. *Cold Spring*
920 *Harb Symp Quant Biol* **82**:235–247. doi:10.1101/sqb.2017.82.035394
921 Jones AR, Francis R, Schedl T. 1996. GLD-1, a cytoplasmic protein essential for oocyte
922 differentiation, shows stage- ans sex-specific expression during Caenorhabditis elegans
923 germline development. *Dev Biol*. doi:10.1006/dbio.1996.0293
924 Joseph-Strauss D, Gorjánácz M, Santarella-Mellwig R, Voronina E, Audhya A, Cohen-Fix O.
925 2012. Sm protein down-regulation leads to defects in nuclear pore complex disassembly
926 and distribution in C. elegans embryos. *Dev Biol* **365**:445–457.
927 doi:10.1016/j.ydbio.2012.02.036
928 Kamath RS, Fraser AG, Dong Y, Poulin G, Durbin R, Gotta M, Kanapin A, Le Bot N, Moreno S,
929 Sohrmann M, Welchman DP, Zipperien P, Ahringer J. 2003. Systematic functional analysis
930 of the Caenorhabditis elegans genome using RNAi. *Nature* **421**:231–237.
931 doi:10.1038/nature01278
932 Kim S, Spike C, Greenstein D. 2013. Control of oocyte growth and meiotic maturation in
933 caenorhabditis elegans. *Adv Exp Med Biol* **757**:277–320. doi:10.1007/978-1-4614-4015-4-
934 10
935 King GA, Goodman JS, Schick JG, Chetlapalli K, Jorgens DM, McDonald KL, Ünal E. 2019.
936 Meiotic cellular rejuvenation is coupled to nuclear remodeling in budding yeast. *Elife* **8**.
937 doi:10.7554/eLife.47156
938 Kisielnicka E, Minasaki R, Eckmann CR. 2018. MAPK signaling couples SCF-mediated
939 degradation of translational regulators to oocyte meiotic progression. *Proc Natl Acad Sci U*
940 *S A* **115**:E2772–E2781. doi:10.1073/pnas.1715439115
941 Kobayashi H, Minshull J, Ford C, Golsteyn R, Poon R, Hunt T. 1991. On the synthesis and
942 destruction of A- and B-type cyclins during oogenesis and meiotic maturation in Xenopus
943 laevis. *J Cell Biol*. doi:10.1083/jcb.114.4.755

944 Kosinki M, McDonald K, Schwartz J, Yamamoto I, Greenstein D. 2005. C. elegans sperm bud
945 vesicles to deliver a meiotic maturation signal to distant oocytes. *Development* **132**:3357–
946 3369. doi:10.1242/dev.01916
947 Langerak S, Trombley A, Patterson JR, Leroux D, Couch A, Wood MP, Schisa JA. 2019.
948 Remodeling of the endoplasmic reticulum in Caenorhabditis elegans oocytes is regulated
949 by CGH-1. *Genesis* **57**:1–8. doi:10.1002/dvg.23267
950 Lapierre LR, De Magalhaes Filho CD, McQuary PR, Chu CC, Visvikis O, Chang JT, Gelino S,
951 Ong B, Davis AE, Irazoqui JE, Dillin A, Hansen M. 2013. The TFEB orthologue HLH-30
952 regulates autophagy and modulates longevity in Caenorhabditis elegans. *Nat Commun* **4**.
953 doi:10.1038/ncomms3267
954 Lee SS, Lee RYN, Fraser AG, Kamath RS, Ahringer J, Ruvkun G. 2003. A systematic RNAi
955 screen identifies a critical role for mitochondria in C. elegans longevity. *Nat Genet*.
956 doi:10.1038/ng1056
957 Lehner B, Tischler J, Fraser AG. 2006. RNAi screens in Caenorhabditis elegans in a 96-well
958 liquid format and their application to the systematic identification of genetic interactions.
959 *Nat Protoc* **1**:1617–1620. doi:10.1038/nprot.2006.245
960 Llorca O, Martín-Benito J, Ritco-Vonsovici M, Grantham J, Hynes GM, Willison KR, Carrascosa
961 JL, Valpuesta JM. 2000. Eukaryotic chaperonin CCT stabilizes actin and tubulin folding
962 intermediates in open quasi-native conformations. *EMBO J* **19**:5971–5979.
963 doi:10.1093/emboj/19.22.5971
964 Luo S, Kleemann GA, Ashraf JM, Shaw WM, Murphy CT. 2010. TGF-β and Insulin Signaling
965 Regulate Reproductive Aging via Oocyte and Germline Quality Maintenance. *Cell*
966 **143**:299–312. doi:10.1016/j.cell.2010.09.013
967 Maller J, Wu M, Gerhart JC. 1977. Changes in protein phosphorylation accompanying
968 maturation of Xenopus laevis oocytes. *Dev Biol*. doi:10.1016/0012-1606(77)90093-8
969 Mccarter J, Bartlett B, Dang T, Schedl T. 1999. On the Control of Oocyte Meiotic Maturation and

970 Ovulation in Caenorhabditis elegans.
971 McDonald KL, Webb RI. 2011. Freeze substitution in 3 hours or less. *J Microsc* **243**:227–33.
972 doi:10.1111/j.1365-2818.2011.03526.x
973 Mehlmann LM, Terasaki M, Jaffe LA, Kline D. 1995. Reorganization of the endoplasmic
974 reticulum during meiotic maturation of the mouse oocyte.
975 Miller MA, Nguyen VQ, Lee MH, Kosinski M, Schedl T, Caprioli RM, Greenstein D. 2001. A
976 sperm cytoskeletal protein that signals oocyte meiotic maturation and ovulation. *Science*
977 *(80-)* **291**:2144–2147. doi:10.1126/science.1057586
978 Miller MA, Ruest PJ, Kosinski M, Hanks SK, Greenstein D. 2003. An Eph receptor sperm-
979 sensing control mechanism for oocyte meiotic maturation in Caenorhabditis elegans.
980 *Genes Dev* **17**:187–200. doi:10.1101/gad.1028303
981 O'Rourke EJ, Ruvkun G. 2013. MXL-3 and HLH-30 transcriptionally link lipolysis and autophagy
982 to nutrient availability. *Nat Cell Biol* **15**:668–676. doi:10.1038/ncb2741
983 Paix A, Folkmann A, Rasoloson D, Seydoux G. 2015. High efficiency, homology-directed
984 genome editing in Caenorhabditis elegans using CRISPR-Cas9ribonucleoprotein
985 complexes. *Genetics*. doi:10.1534/genetics.115.179382
986 Paix A, Schmidt H, Seydoux G. 2016. Cas9-assisted recombineering in C. elegans: Genome
987 editing using in vivo assembly of linear DNAs. *Nucleic Acids Res* **44**:e128.
988 doi:10.1093/nar/gkw502
989 Poteryaev D, Squirrell JM, Campbell JM, White JG, Spang A. 2005. Involvement of the Actin
990 Cytoskeleton and Homotypic Membrane Fusion in ER Dynamics in Caenorhabditis elegans
991 □ V. *Mol Biol Cell* **16**:2139–2153. doi:10.1091/mbc.E04
992 Qiao H, Rao HBDP, Yun Y, Sandhu S, Fong JH, Sapre M, Nguyen M, Tham A, Van BW, Chng
993 TYH, Lee A, Hunter N. 2018. Impeding DNA Break Repair Enables Oocyte Quality Control.
994 *Mol Cell* **72**:211-221.e3. doi:10.1016/j.molcel.2018.08.031
995 Reis-Rodrigues P, Czerwieniec G, Peters TW, Evani US, Alavez S, Gaman EA, Vantipalli M,

996 Mooney SD, Gibson BW, Lithgow GJ, Hughes RE. 2012. Proteomic analysis of age-
997 dependent changes in protein solubility identifies genes that modulate lifespan. *Aging Cell*.
998 doi:10.1111/j.1474-9726.2011.00765.x
999 Roux AE, Langhans K, Huynh W, Kenyon C. 2016. Reversible Age-Related Phenotypes
1000 Induced during Larval Quiescence in C. Elegans. *Cell Metab*.
1001 doi:10.1016/j.cmet.2016.05.024
1002 Sahu R, Kaushik S, Clement CC, Cannizzo ES, Scharf B, Follenzi A, Potolicchio I, Nieves E,
1003 Cuervo AM, Santambrogio L. 2011. Microautophagy of Cytosolic Proteins by Late
1004 Endosomes. *Dev Cell*. doi:10.1016/j.devcel.2010.12.003
1005 Schumacher B, Hofmann K, Boulton S, Gartner A. 2001. The C. elegans homolog of the p53
1006 tumor suppressor is required for DNA damage-induced apoptosis. *Curr Biol*.
1007 doi:10.1016/S0960-9822(01)00534-6
1008 Shirayama M, Seth M, Lee HC, Gu W, Ishidate T, Conte D, Mello CC. 2012. PiRNAs initiate an
1009 epigenetic memory of nonself RNA in the C. elegans germline. *Cell*.
1010 doi:10.1016/j.cell.2012.06.015
1011 Spike CA, Huelgas-Morales G, Tsukamoto T, Greenstein D. 2018. Multiple mechanisms
1012 inactivate the LIN-41 RNA-binding protein to ensure a robust oocyte-to-embryo transition in
1013 caenorhabditis elegans. *Genetics* **210**:1011–1037. doi:10.1534/genetics.118.301421
1014 Sun Y, Li M, Zhao D, Li X, Yang C, Wang X. 2020. Lysosome activity is modulated by multiple
1015 longevity pathways and is important for lifespan extension in C. elegans. *Elife*.
1016 doi:10.7554/eLife.55745
1017 Taylor RC, Dillin A. 2011. Aging as an event of proteostasis collapse. *Cold Spring Harb*
1018 *Perspect Biol*. doi:10.1101/cshperspect.a004440
1019 Ünal E, Kinde B, Amon A. 2011. Gametogenesis eliminates age-induced cellular damage and
1020 resets life span in yeast. *Science (80-)* **332**:1554–1557. doi:10.1126/science.1204349
1021 Walther DM, Kasturi P, Zheng M, Pinkert S, Vecchi G, Ciryam P, Morimoto RI, Dobson CM,

1022 Vendruscolo M, Mann M, Hartl FU. 2015. Widespread proteome remodeling and
1023 aggregation in aging C. elegans. *Cell*. doi:10.1016/j.cell.2015.03.032
1024 Wasserman WJ, Richter JD, Smith LD. 1982. Protein synthesis during maturation promoting
1025 factor- and progesterone-induced maturation in Xenopus oocytes. *Dev Biol*.
1026 doi:10.1016/0012-1606(82)90303-7
1027 Williams RL, Urbé S. 2007. The emerging shape of the ESCRT machinery. *Nat Rev Mol Cell*
1028 *Biol*. doi:10.1038/nrm2162
1029 Wright JE, Gaidatzis D, Senften M, Farley BM, Westhof E, Ryder SP, Ciosk R. 2011. A
1030 quantitative RNA code for mRNA target selection by the germline fate determinant GLD-1.
1031 *EMBO J* **30**:533–545. doi:10.1038/emboj.2010.334
1032 Yamashita YM. 2018. Subcellular specialization and organelle behavior in germ cells. *Genetics*
1033 **208**:19–51. doi:10.1534/genetics.117.300184
1034 Zhang H, Alsaleh G, Feltham J, Sun Y, Napolitano G, Riffelmacher T, Charles P, Frau L, Hublitz
1035 P, Yu Z, Mohammed S, Ballabio A, Balabanov S, Mellor J, Simon AK. 2019. Polyamines
1036 Control eIF5A Hypusination, TFEB Translation, and Autophagy to Reverse B Cell
1037 Senescence. *Mol Cell* **76**:110-125.e9. doi:10.1016/j.molcel.2019.08.005
1038 Zou L, Wu D, Zang X, Wang Z, Wu Z, Chen D. 2019. Construction of a germline-specific RNAi
1039 tool in C. elegans. *Sci Rep* **9**:1–10. doi:10.1038/s41598-019-38950-8
1040

Figure S1

A

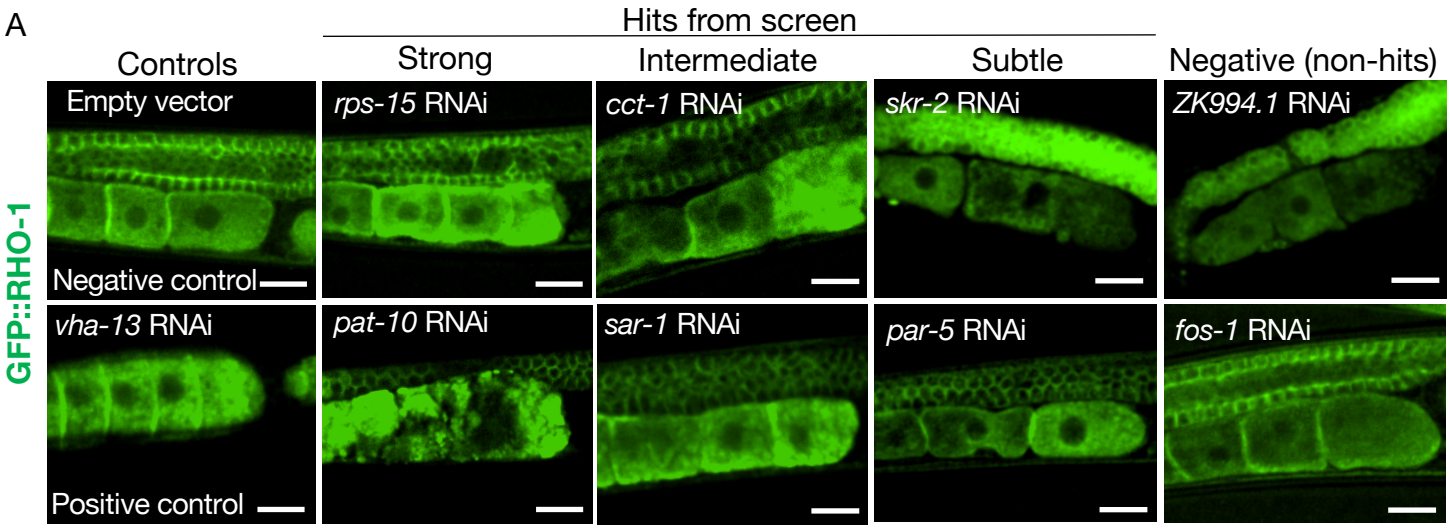

B

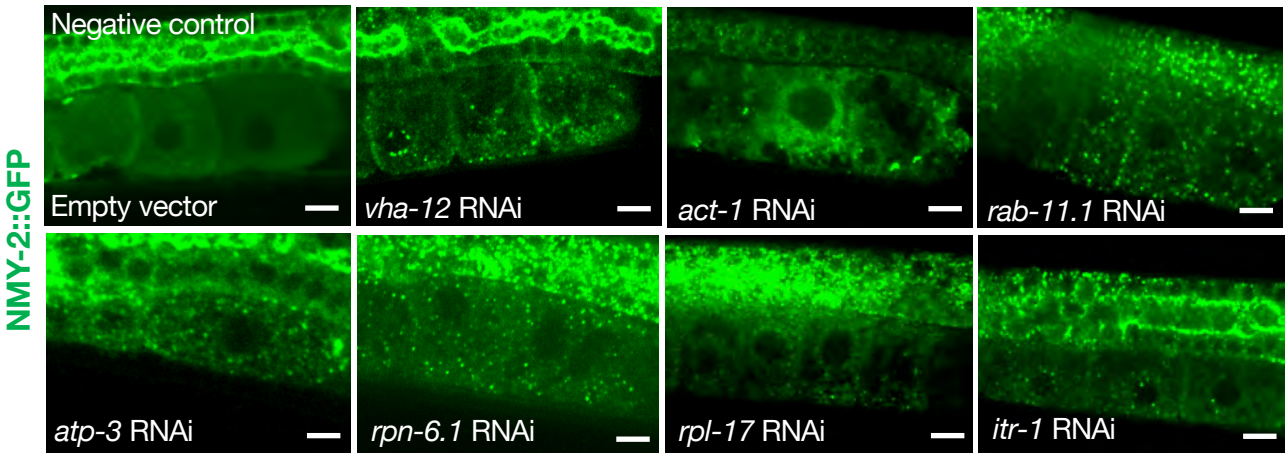

C

GO biological process	Fold enrichment	P-value
Translation	5.01	5.53E-08
ATP-hydrolysis coupled proton transport	27.17	3.76E-08
Ovulation	13.66	6.19E-05
RNA processing	3.26	3.22E-05
Cortical actin cytoskeleton organization	20.11	7.73E-04
Vacuolar acidification	24.58	4.77E-04

Figure S1.

(A) RNAi clones causing GFP::RHO-1 aggregates in hermaphrodite oocytes (SA115), visualized at low magnification (20X objective) during primary screening. Scale bars, 20 μm. (B) Examples of NMY-2::GFP aggregates in oocytes of hermaphrodites (JJ1473) undergoing orthogonal verification with a different aggregation-prone protein. Scale bars,10 μm. (C) The highest enriched gene-ontology (GO) process categories represented by the validated genes identified in the screen.

Figure S2

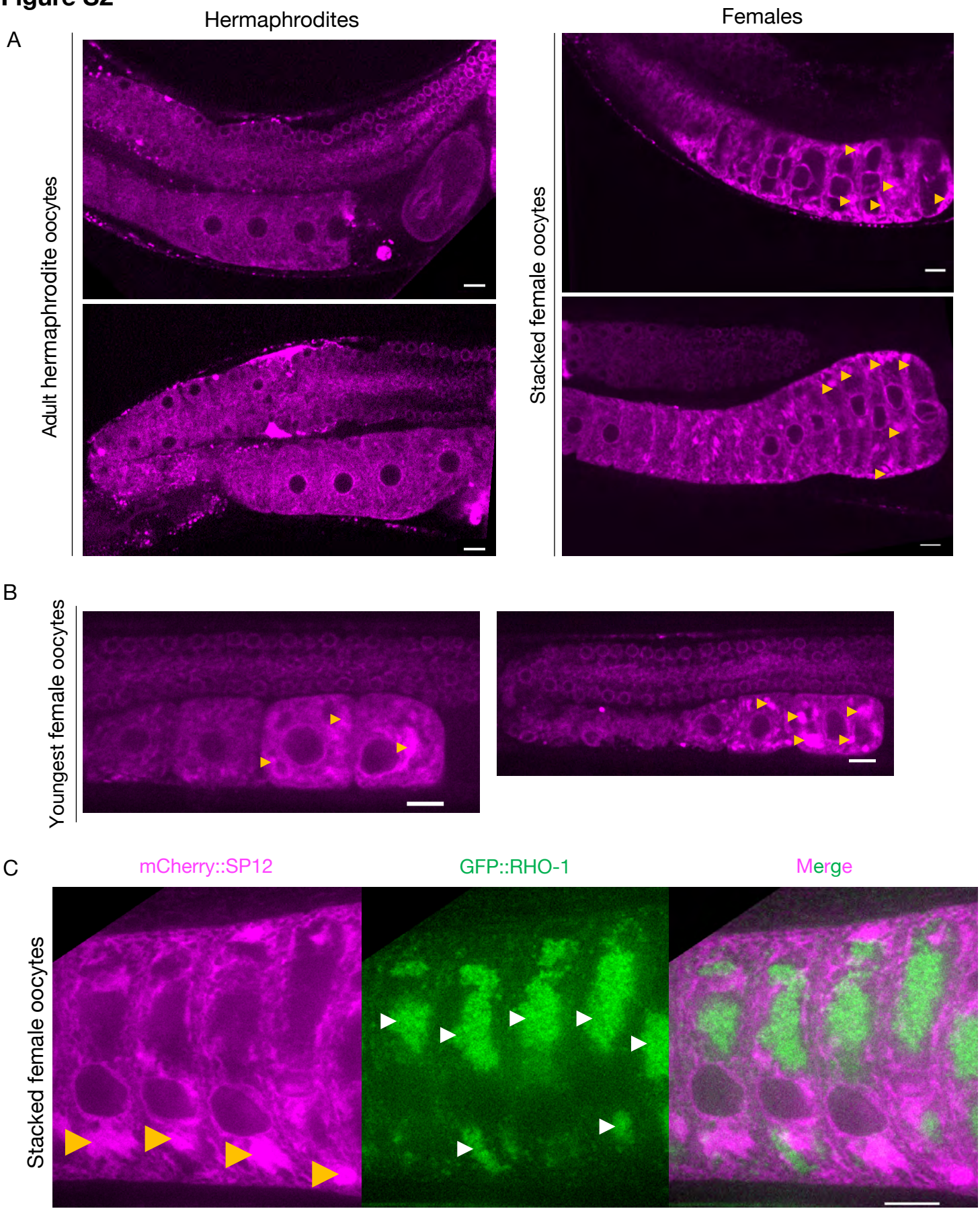
A
Hermaphrodites
Females
Adult hermaphrodite oocytes
Stacked female oocytes
B
Youngest female oocytes
C
mCherry::SP12
GFP::RHO-1
Merge
Stacked female oocytes

Figure S2.

(A) Comparison of ER morphology in oocytes from hermaphrodites (OCF15) and females (CF4542) expressing the ER reporter mCherry::SP12 in the germline. Oocytes in the female gonad stack over time, as new meiotic cells make their way down towards the spermatheca, but mature ones pass less readily into the uterus. Orange arrows, ER patches. (B) Visualization of ER patches in young oocytes of female animals, staged to capture the earliest oocytes. (C) Simultaneous visualization of GFP::RHO-1 aggregates and the ER in females (CF4557) at high magnification (100X objective). Orange arrows: ER patches; white arrows: GFP::RHO-1 aggregates. Scale bars (A-C),10 μm.

Figure S3

Hermaphrodites (Very first oocytes)

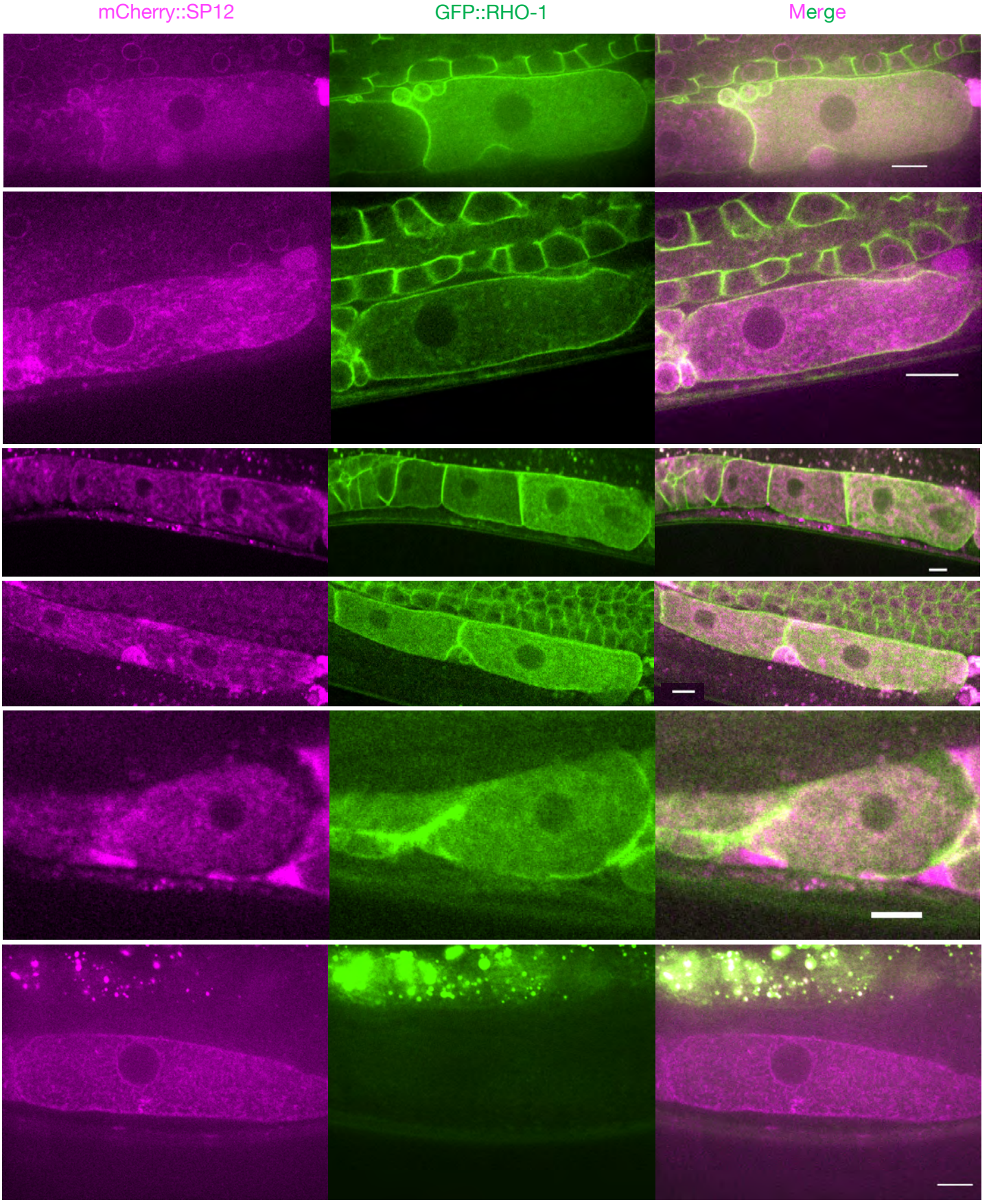

Figure S3.

Extended data related to Figure 2B.

ER morphology and GFP::RHO-1 localization in the first, newly-formed oocytes from mCherry::SP12-expressing hermaphrodites (CF4552). Scale bars,10 μm. Note that the GFP::RHO-1 image from the 1st row is also displayed in figure 1E.

Figure S4

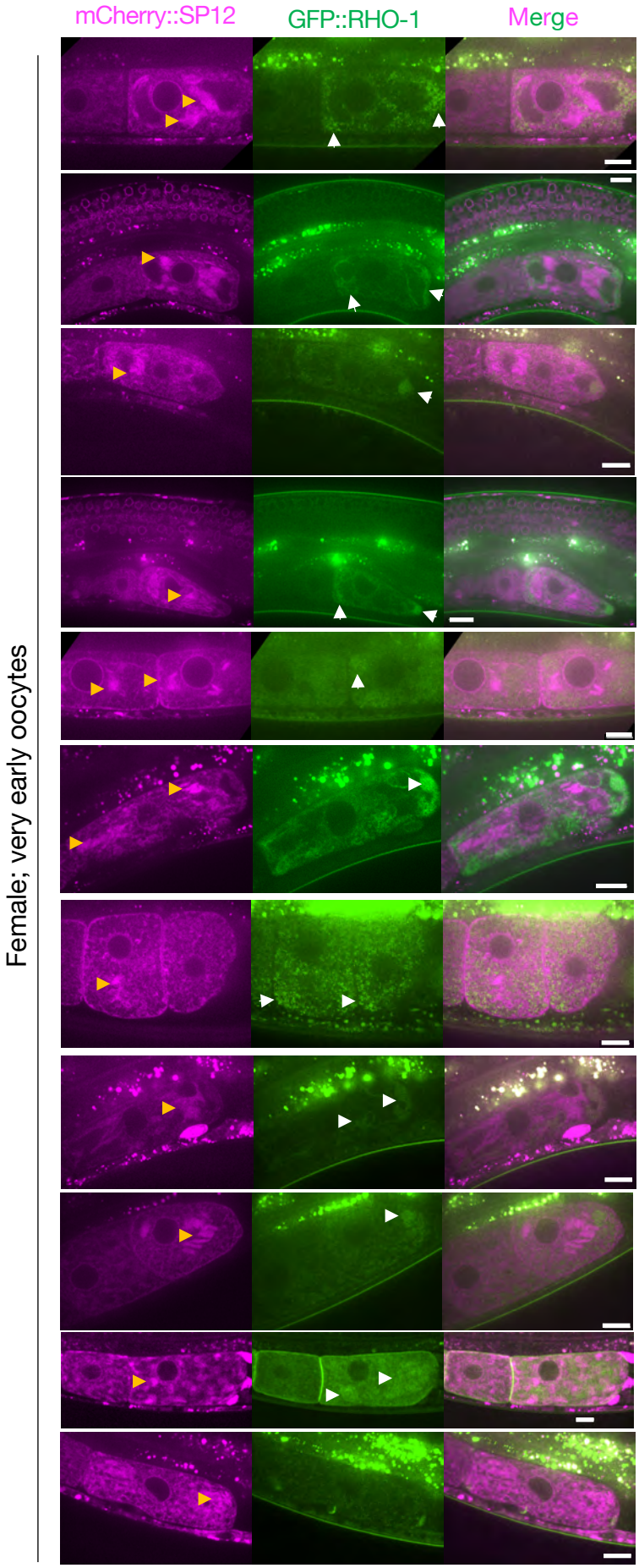

Figure S4.

Extended data related to Figure 2B.

ER morphology and GFP::RHO-1 localization in the first, newly-formed oocytes from mCherry::SP12 expressing females (CF4557). Orange arrows: ER patches; white arrows: GFP::RHO-1 aggregates. Scale bars, 10 μm. Note that the GFP::RHO-1 image from the 6th row is also displayed in figure 1E.

Figure S5

Females

A

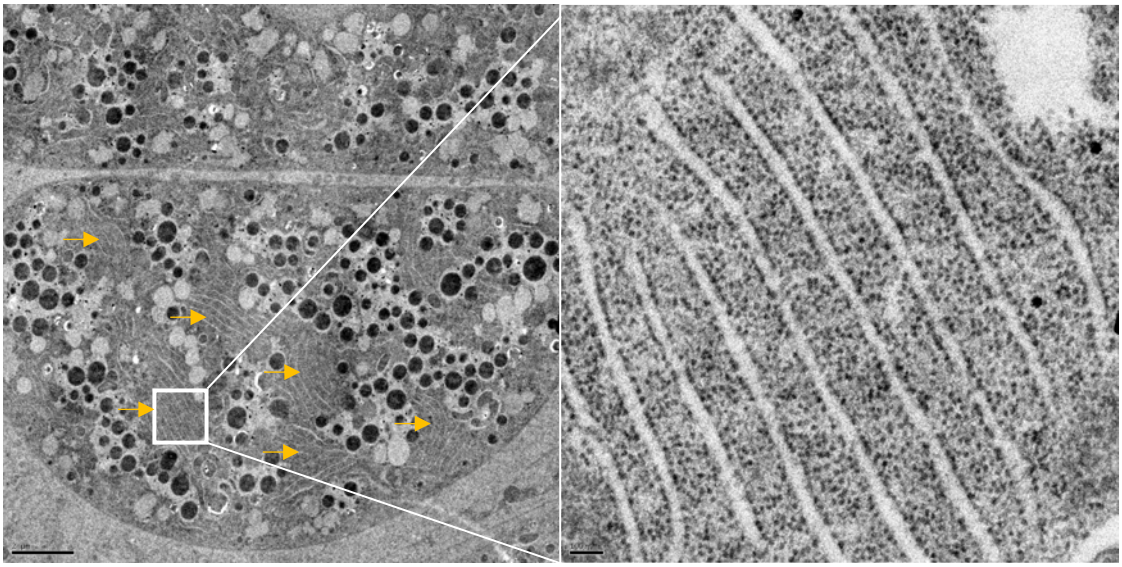

B

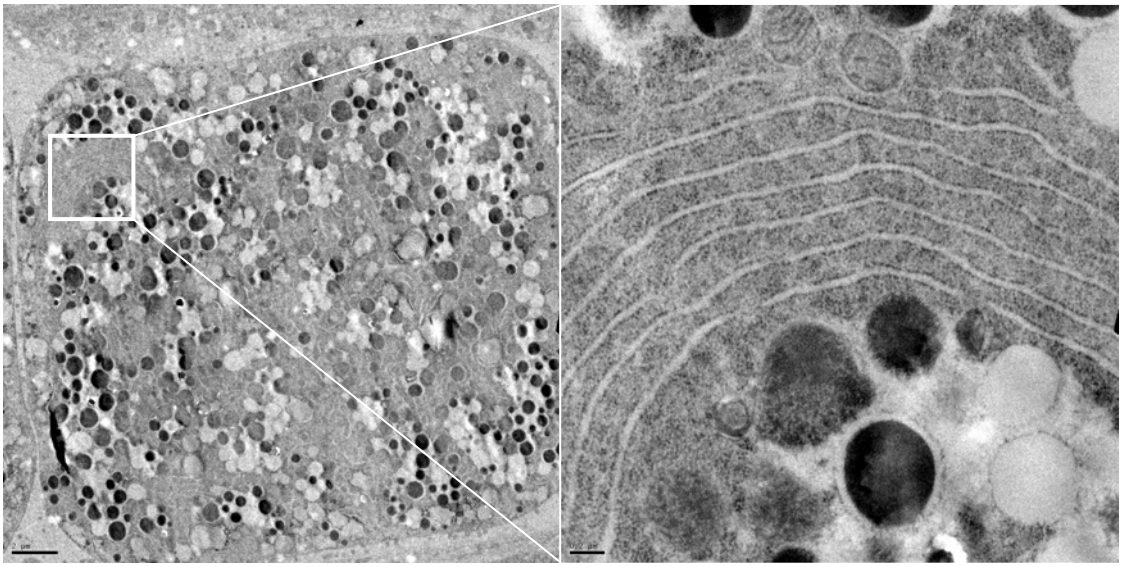

Hermaphrodite

C

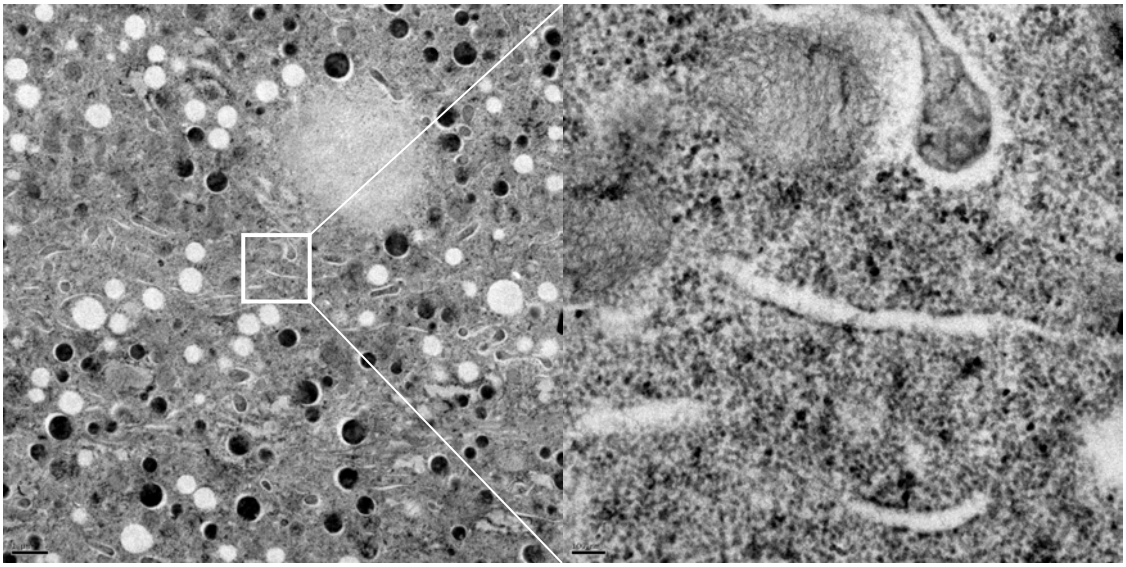

Figure S5.

Extended data related to Figure 2D.

Transmission electron micrographs from hermaphrodite (N2E) and female (CF4101) oocytes. (A) Female oocyte. Arrow, ER stacks. Left panel, magnification: 1,200X, scale bar, 2 μm. Right panel, magnification: 13,000X, scale bar, 100 nm. (B) Female oocyte. Arrow, ER. Left panel, magnification: 890X, scale bar, 2 μm. Right panel, magnification: 6,800X, scale bar, 200 nm. (C) Hermaphrodite oocyte. Arrow, ER. Left panel, magnification: 1,400X, scale bar, 1 μm. Right panel, magnification: 13,000X, scale bar, 100 nm.

Figure S6A

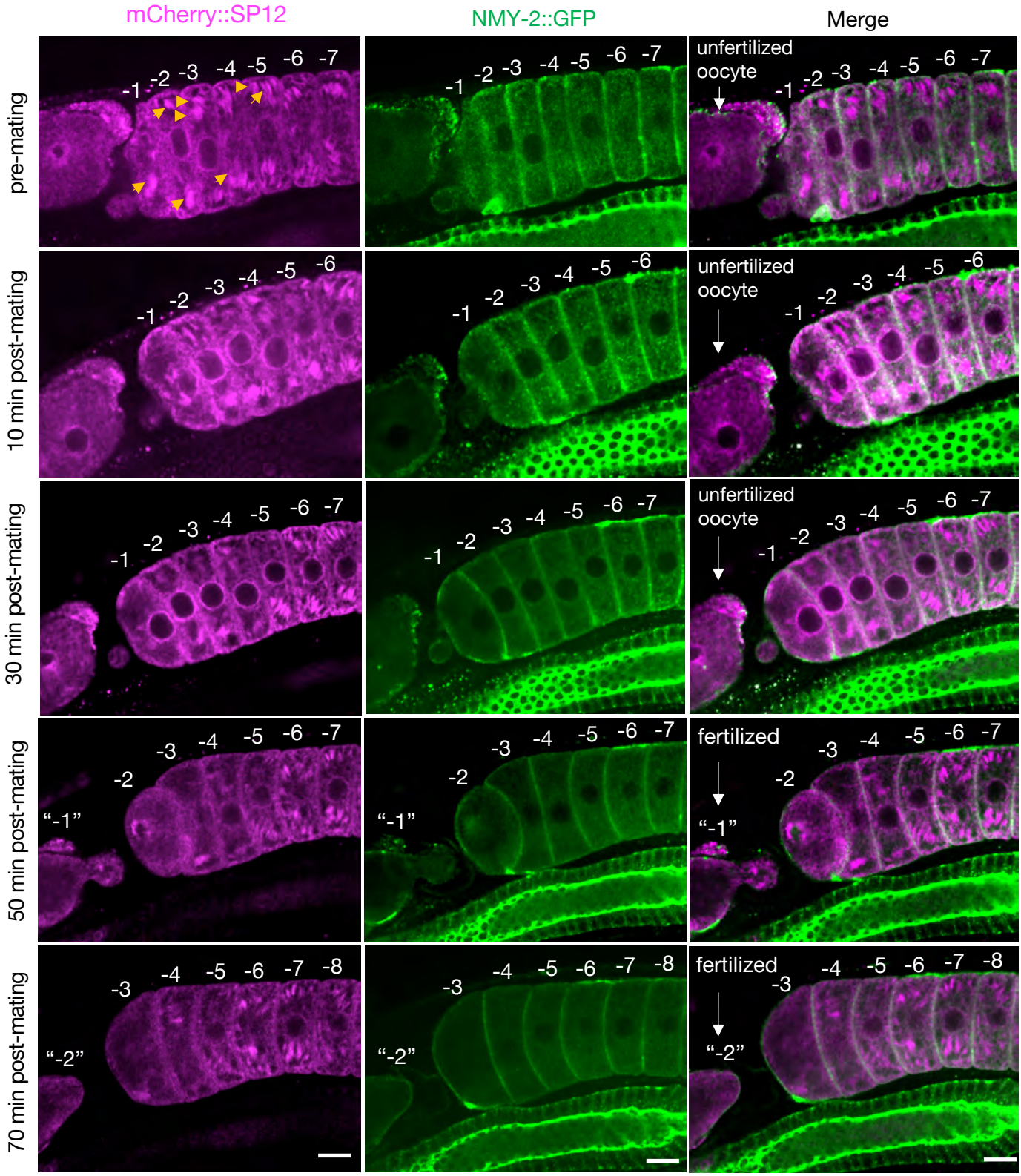
mCherry::SP12
NMY-2::GFP
Merge
pre-mating
10 min post-mating
30 min post-mating
50 min post-mating
70 min post-mating
unfertilized oocyte
fertilized
"-1"
"-2"

Figure S6B

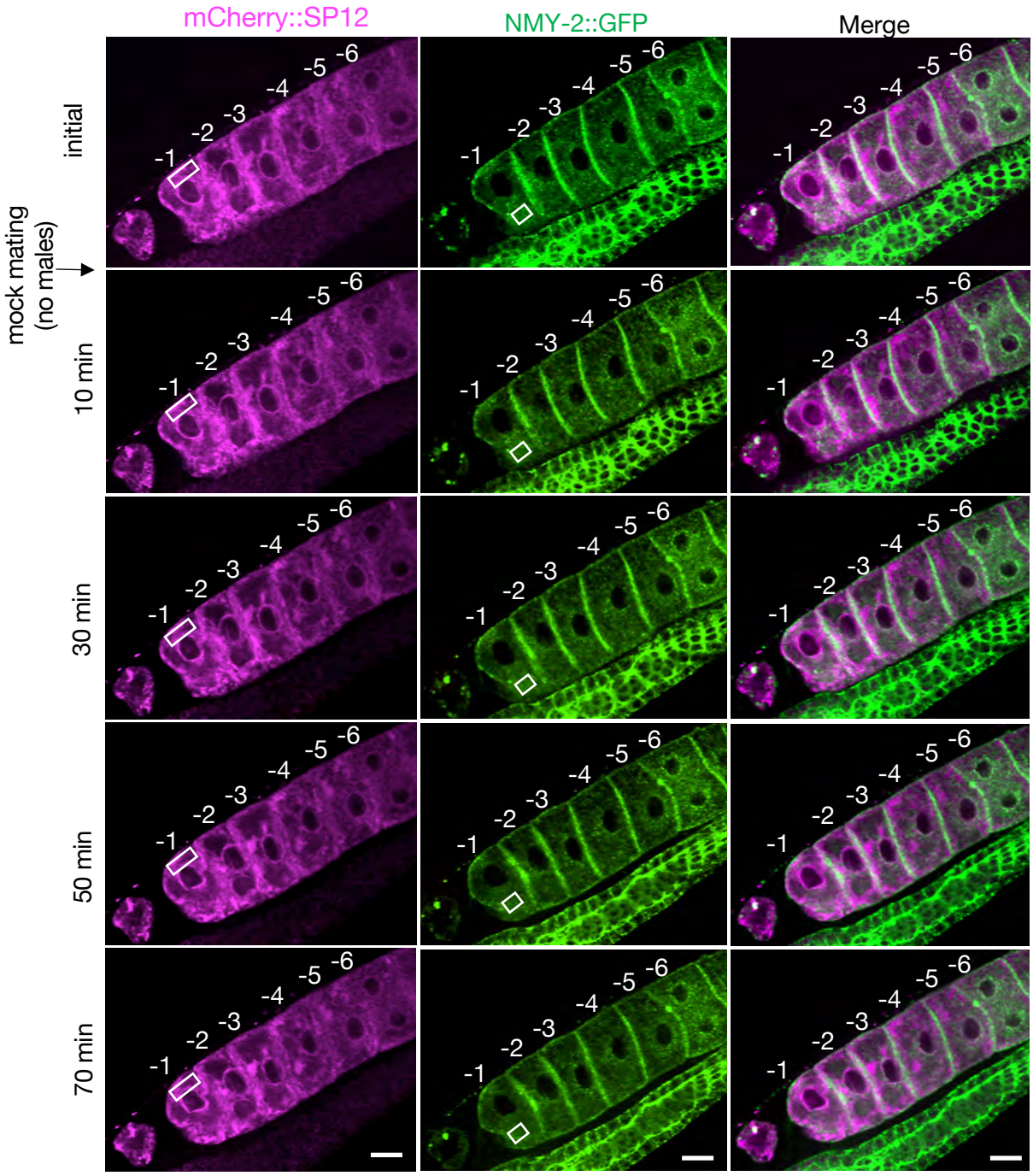
mCherry::SP12
NMY-2::GFP
Merge
initial
mock mating
(no males)
10 min
30 min
50 min
70 min
-1
-2
-3
-4
-5
-6

C

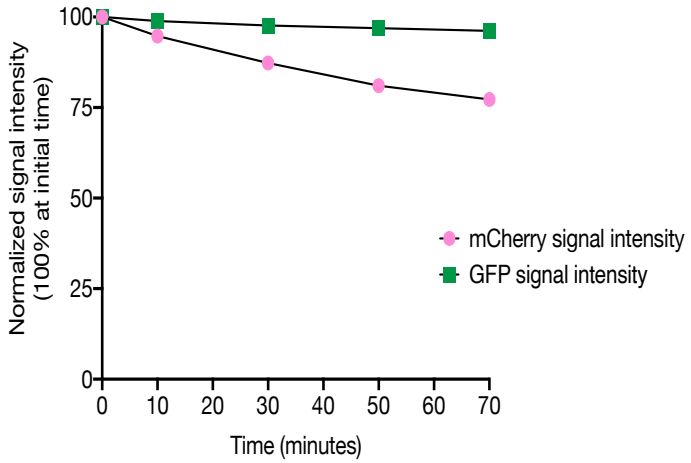
Normalized signal intensity
(100% at initial time)
100
75
50
25
0
0
10
20
30
40
50
60
70
Time (minutes)
mCherry signal intensity
GFP signal intensity

Figure S6.

(A) Simultaneous visualization of the alteration in ER morphology and clearance of aggregates in female oocytes (CF4560) as a function of time, following mating. The earliest changes in the mCherry::SP12 signal (ER) were observed ~10 minutes after mating, whereas the first signs of aggregate (NMY-2::GFP) clearance appeared later, between 20 and 30 minutes. The ER morphology was significantly altered by 30 minutes. Orange arrows: Initial ER patches altered at ~10 minutes. The oocytes are numbered according to their initial positions relative to the spermatheca prior to mating, and the numbers are maintained as the oocytes enter the uterus following fertilization. The figure shows a single representative animal from 7 independent experiments. Scale bars, 10 μm. (B) The mCherry::SP12 and NMY-2::GFP signals in oocytes of CF4560 females visualized as in (A) but not subjected to mating, to control for photobleaching. A single individual is shown from a total of 4 independent experiments. Scale bars,10 μm. (C) Reduction in signal intensity of the two fluorophores with time due to photobleaching, without exposure to males (from Fig. S6B). The signal intensities from specified areas (white rectangles) of the most proximal oocyte were assessed for this purpose.

Figure S7

A

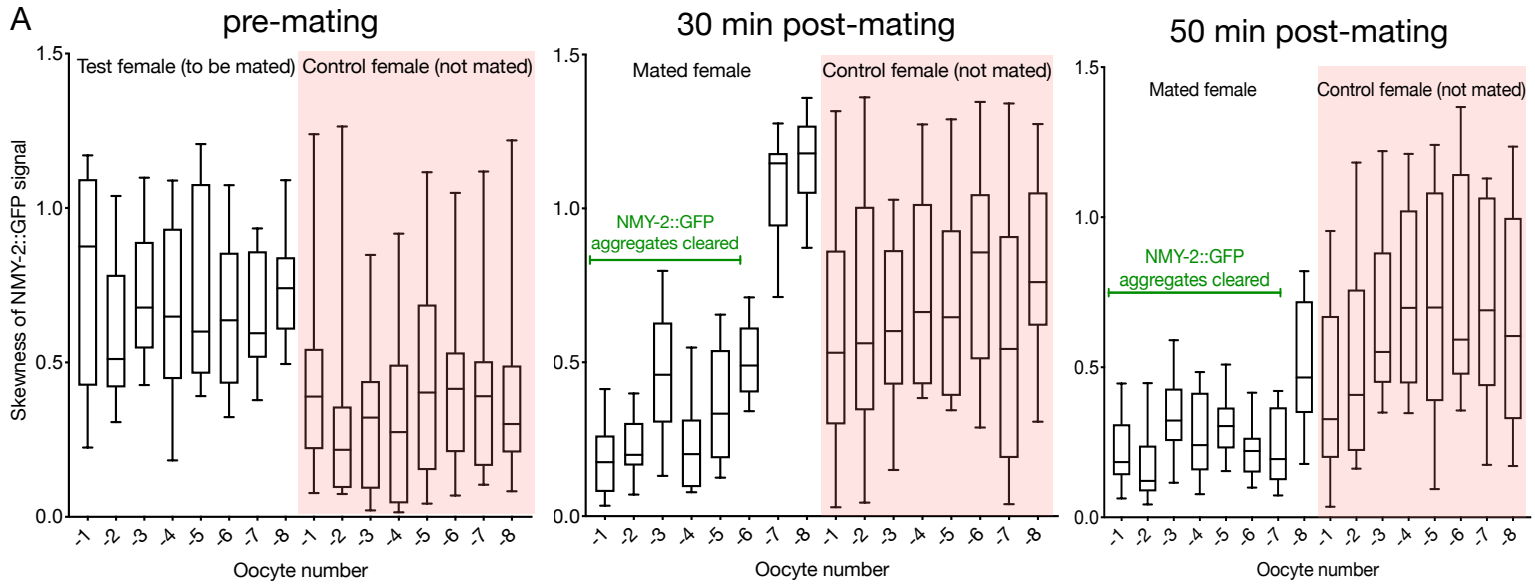
pre-mating
30 min post-mating
50 min post-mating
Test female (to be mated)
Control female (not mated)
Mated female
Control female (not mated)
Mated female
Control female (not mated)
NMY-2::GFP aggregates cleared
NMY-2::GFP aggregates cleared
Skewness of NMY-2::GFP signal
1.5
1.0
0.5
0.0
-1 -2 -3 -4 -5 -6 -7 -8
Oocyte number

B

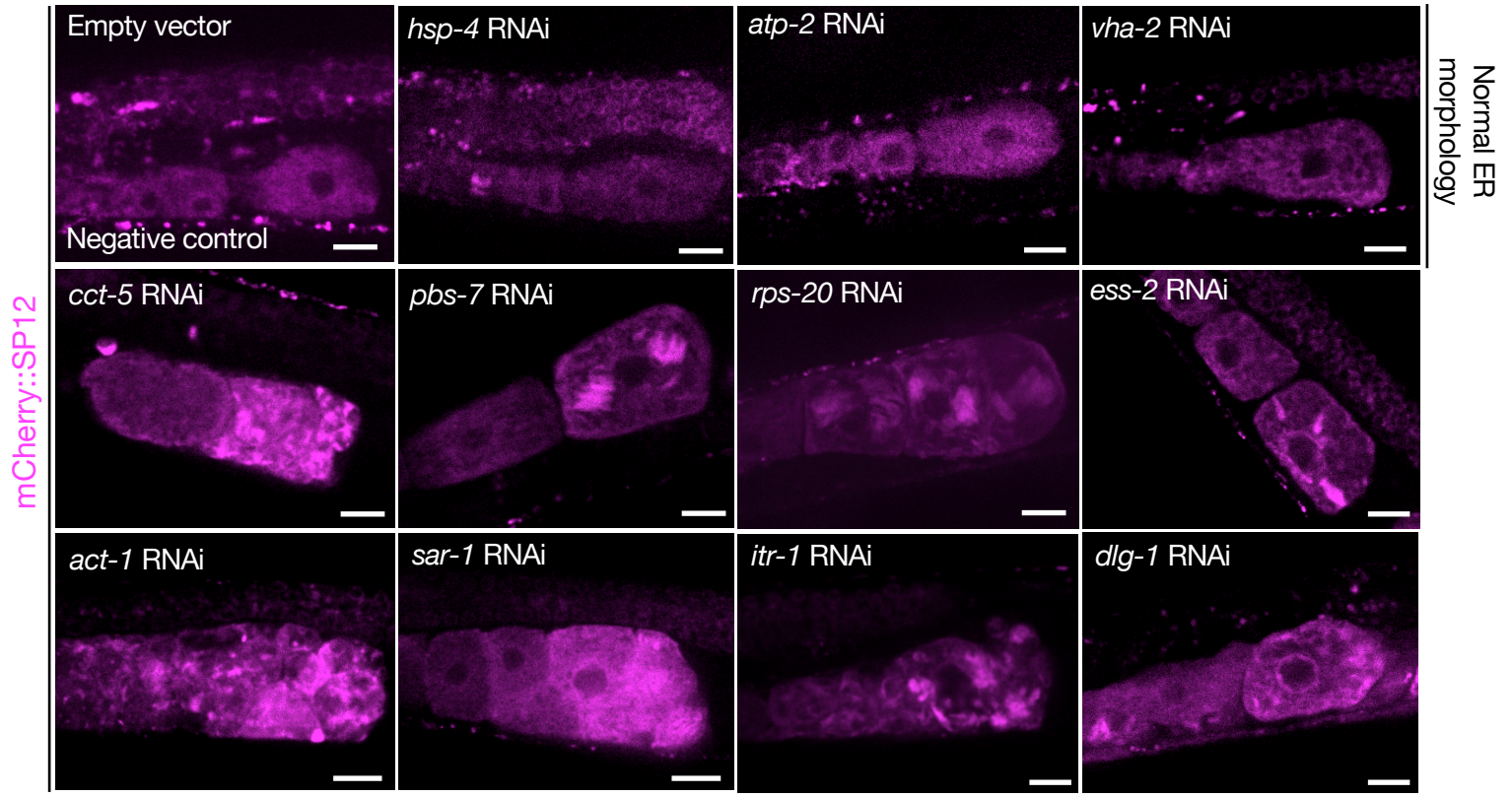
Empty vector
Negative control
hsp-4 RNAi
atp-2 RNAi
vha-2 RNAi
cct-5 RNAi
pbs-7 RNAi
rps-20 RNAi
ess-2 RNAi
act-1 RNAi
sar-1 RNAi
itr-1 RNAi
dlg-1 RNAi
mCherry::SP12
Normal ER morphology

Figure S7.

(A) NMY-2::GFP signal skewness as a function of time in the proximal oocytes of CF4560 females, either subjected to mating with CB1490 males (white), or not exposed to males (pink). The mated females exhibit a reduction in signal skewness with time, and in relation to the distance from spermatheca, indicative of aggregate clearance. (B) Examples of oocyte ER morphology in CF4552 hermaphrodites subjected to assay-pool RNAi treatment, demonstrating the range of morphologies we observed. GFP::RHO-1 aggregation in the same animals was used as a control to verify successful gene knockdown (not shown). Scale bars, 20 μm.

Figure S8

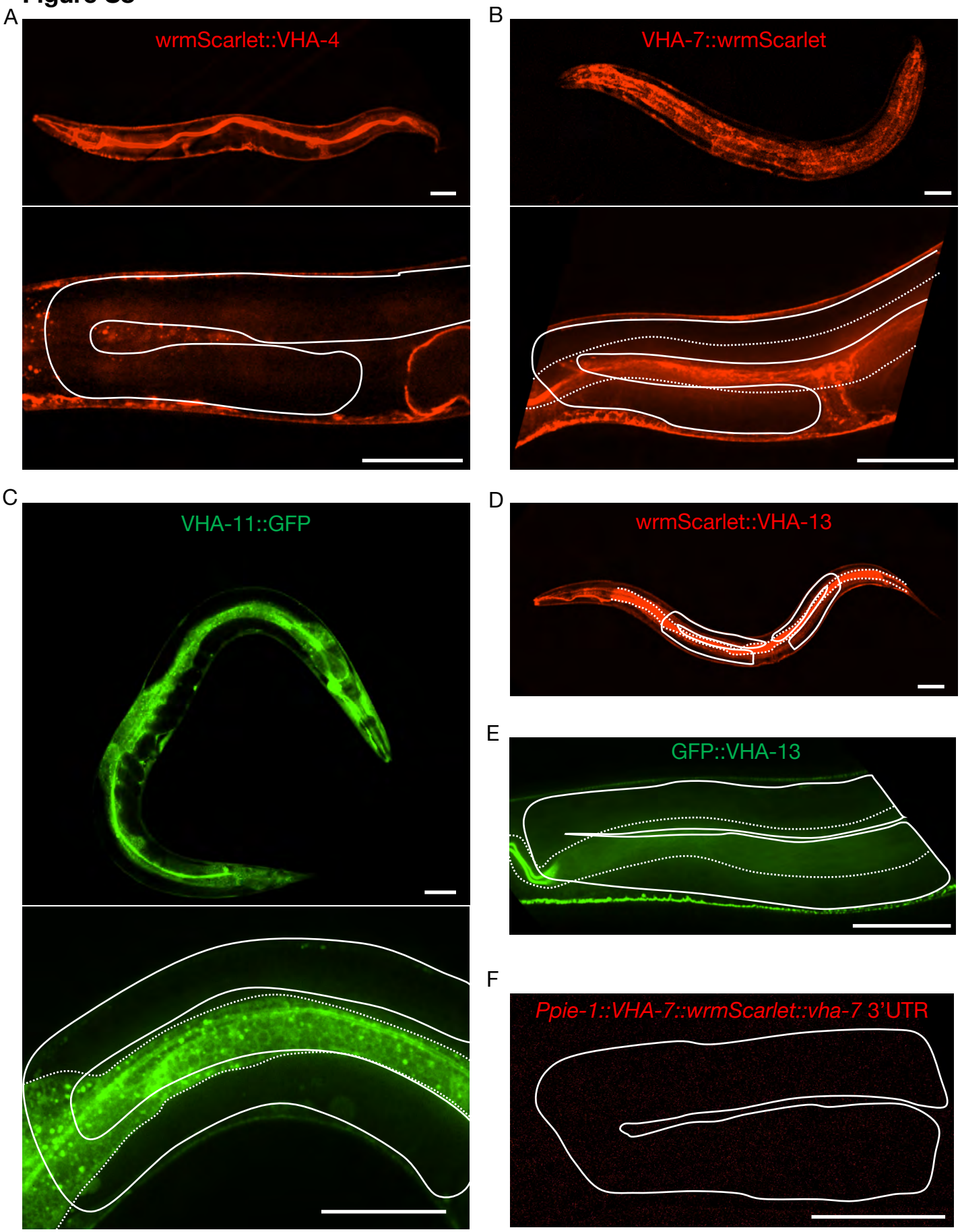
A
wrmScarlet::VHA-4
B
VHA-7::wrmScarlet
C
VHA-11::GFP
D
wrmScarlet::VHA-13
E
GFP::VHA-13
F
Ppie-1::VHA-7::wrmScarlet::vha-7 3'UTR

Figure S8.

Expression of endogenously tagged V-ATPase subunits from the V_0 domain (A and B) and the V_1 domain (C, D and E), and of a single-copy integrated germline transgene (F). None of the strains exhibited detectable signal in the gonad. (A) wrmScarlet::VHA-4, PHX1363 *vha-4(syb1363[wrmScarlet::vha-4]/+) II*, (B) VHA-7::wrmScarlet, PHX1317 *vha-7(syb1317[vha-7::wrmScarlet]) IV*, (C) VHA-11::GFP*,* PHX1198 *ieSi65[sun-1p::TIR1::sun-1 3'UTR + Cbr-unc-119(+)] II; unc-119(ed3) III; vha-11(syb1198[vha-11::gfp::degron]/+) IV*, (D) wrmScarlet::VHA-13, PHX731 *vha-13(syb731[wrmScarlet::vha-13]) V*, (E) GFP::VHA-13, PHX1049 *vha-13(syb1049[gfp::vha-13]) V,* (F) *Ppie-1::vha-7::wrmScarlet::vha-7* 3'UTR, PHX2690 *sybIs2690[Ppie-1::vha-7::wrmScarlet::vha-7 3'UTR, Cbr-unc-119(+)] I; unc-119(ed3) III.* Solid line; gonad and dotted line; intestine. Scale bars, 50 µm. Strains were generated by SunyBiotech for the Kenyon lab.

Figure S9

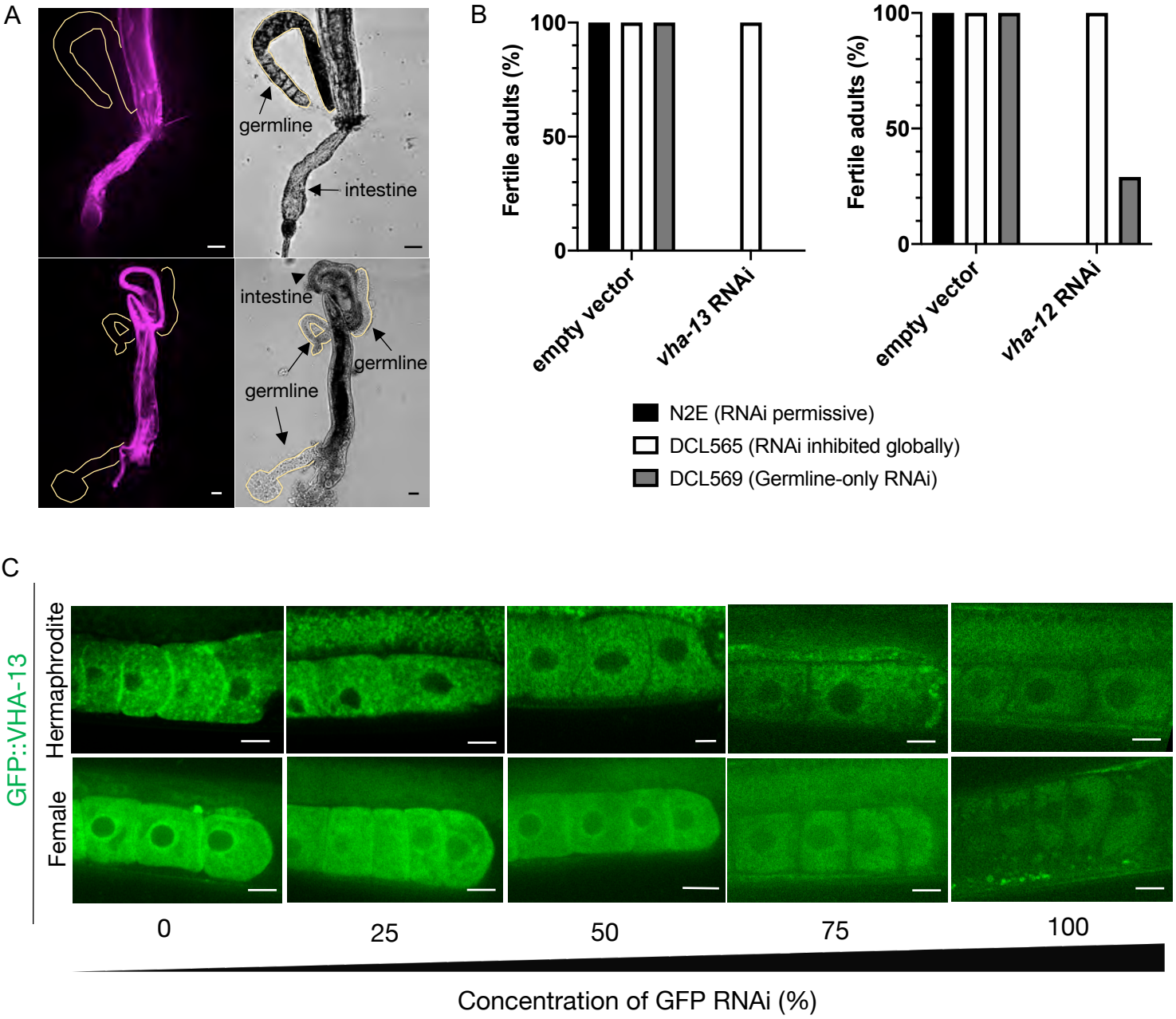
A
germline
intestine
intestine
germline
germline
B
Fertile adults (%)
100
50
0
empty vector
vha-13 RNAi
Fertile adults (%)
100
50
0
empty vector
vha-12 RNAi
N2E (RNAi permissive)
DCL565 (RNAi inhibited globally)
DCL569 (Germline-only RNAi)
C
GFP::VHA-13
Hermaphrodite
Female
0
25
50
75
100
Concentration of GFP RNAi (%)

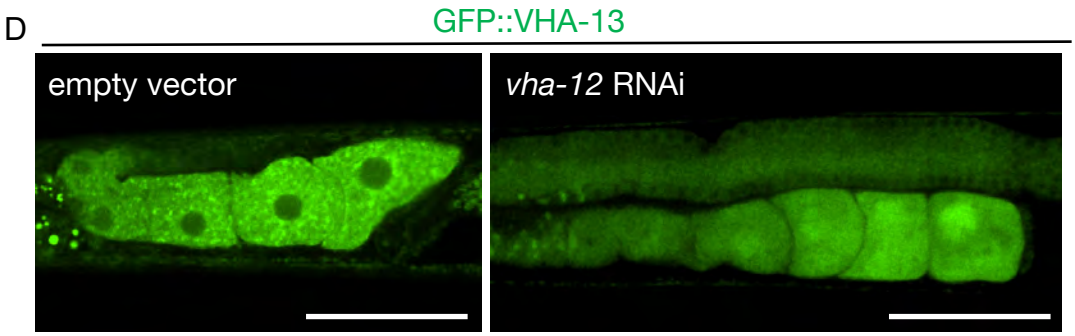
D
GFP::VHA-13
empty vector
vha-12 RNAi

Figure S9.

(A) Attempts to visualize tagged endogenous *wrmScarlet::vha-13* expression in the germline of PHX731 animals by dissecting gonads, to distance them from somatic tissues where it is highly expressed. Scale bars, 25 μm. (B) Percentage of fertile adults in N2E, DCL565 *rde-1(mkc36)*, and DCL569 *rde-1(mkc36); Psun-1::rde-1(+)* strains upon exposure to empty vector RNAi control, *vha-13* RNAi or *vha-12* RNAi, from hatching. Results are averaged from 3 biological replicates with each n>10. (C) Reduction of GFP::VHA-13 expression by serial dilution of *gfp* RNAi bacteria. Even at the limit of detection, hermaphrodites (PHX1414) exhibit discrete GFP::VHA-13 foci, whereas females (CF4599) exhibit a diffuse distribution. Scale bars, 10 μm. (D) Expression of GFP::VHA-13 in the germline of hermaphrodites exposed to empty vector RNAi (left) or *vha-12* RNAi (right). Scale bars, 50 μm.

Figure S10

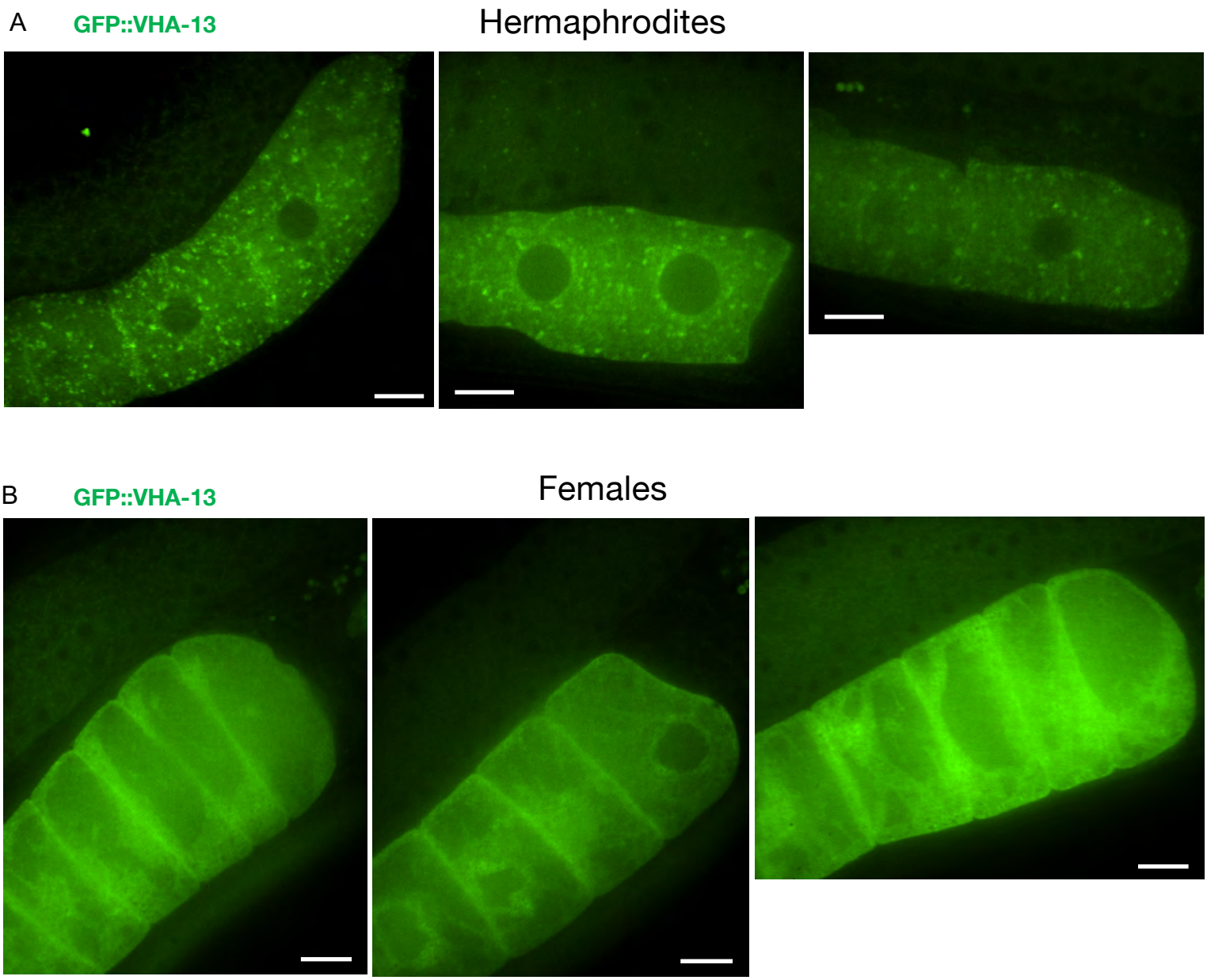

Figure S10.

Extended data related to Figure 3A.

Additional images showing the distribution of GFP::VHA-13 in proximal oocytes of (A) hermaphrodites (PHX1414) and (B) females (CF4599). Scale bars, 10 μm.

Figure S11

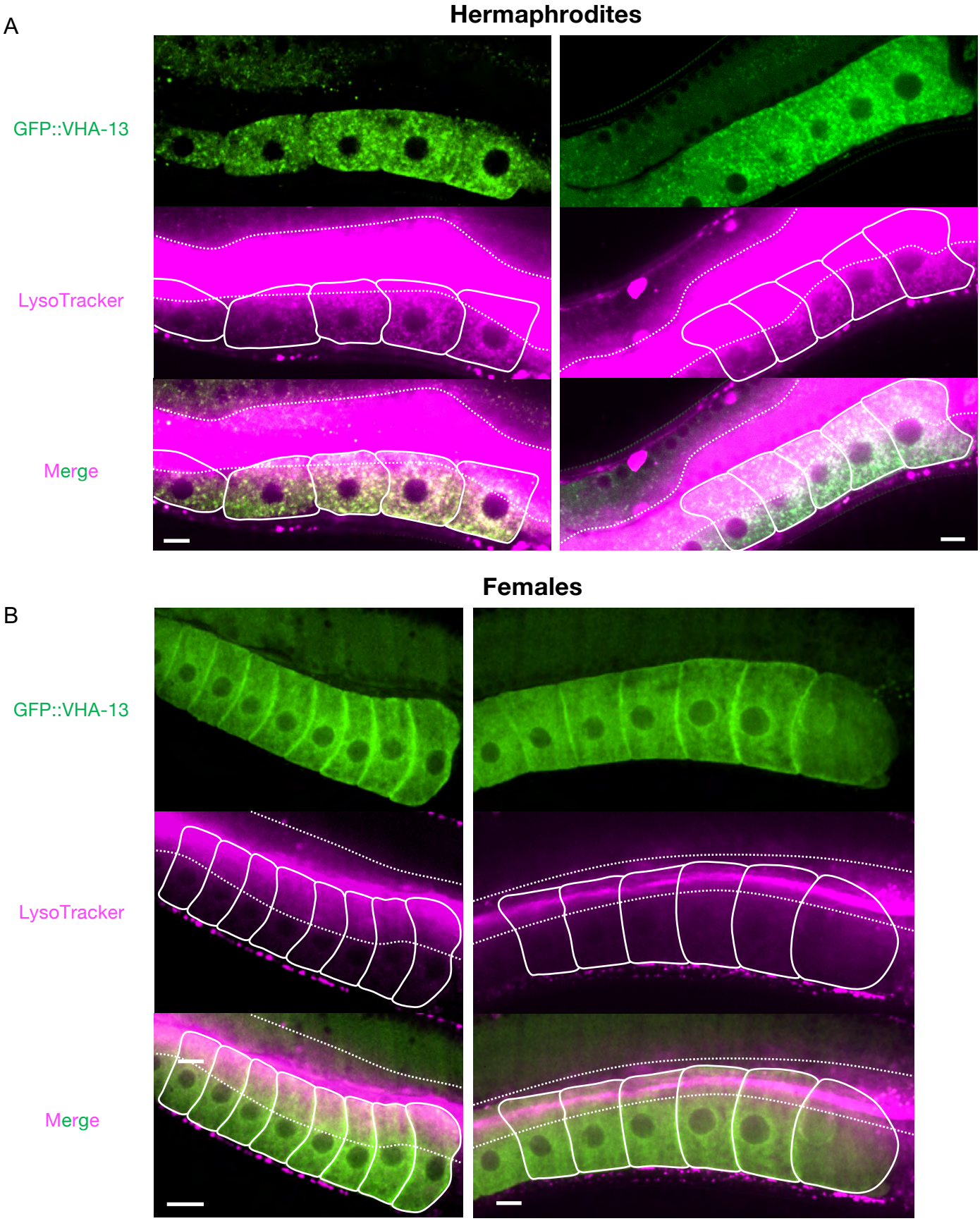
A
Hermaphrodites
GFP::VHA-13
LysoTracker
Merge
B
Females
GFP::VHA-13
LysoTracker
Merge

Figure S11.

Extended data related to Figure 3B.

Additional images of the LysoTracker-stained oocytes from GFP::VHA-13-expressing (A) hermaphrodites (PHX1414) and (B) females (CF4599), for visualization of acidic lysosomes. The two signals colocalize in hermaphrodite oocytes. Dotted line; intestinal boundary, and solid line; oocytes. Scale bars, 10 μm

Figure S12

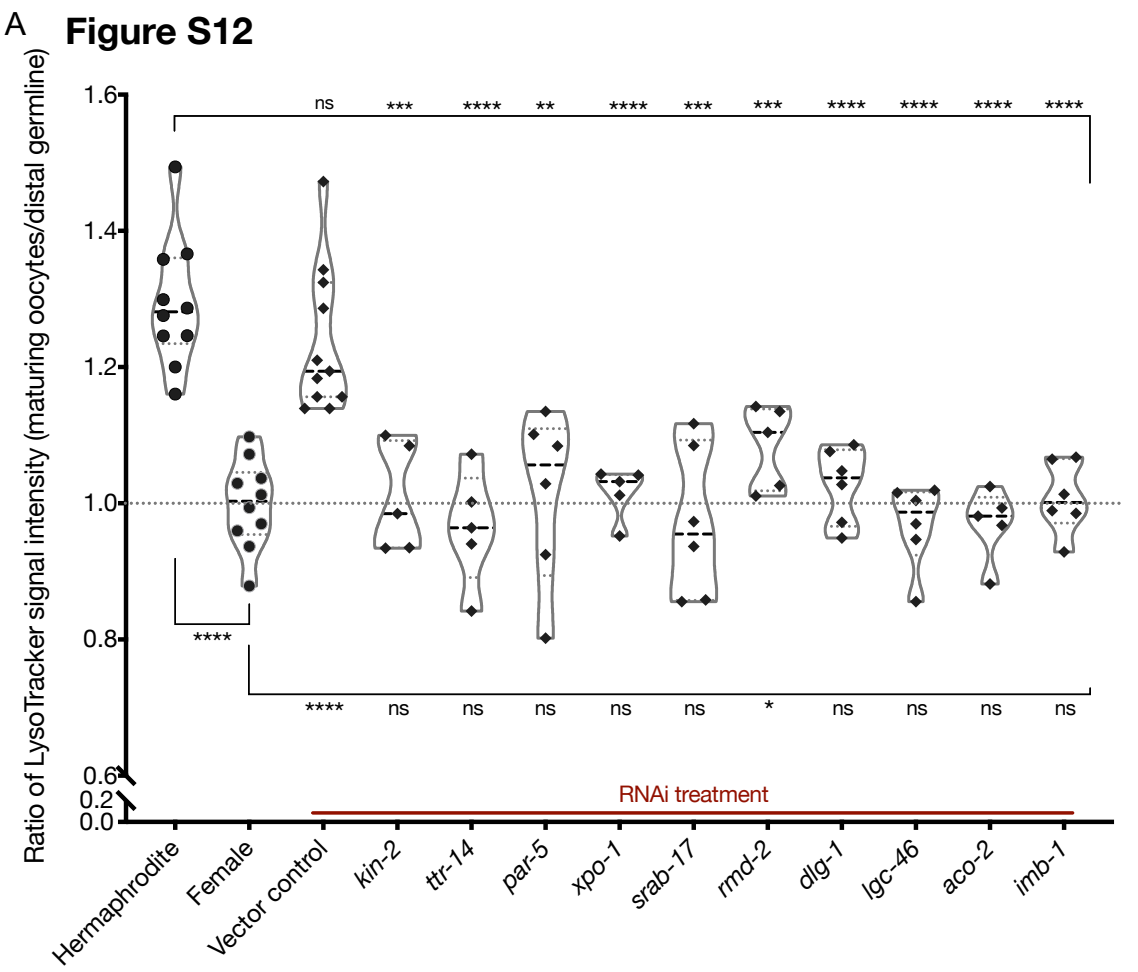
A
Ratio of LysoTracker signal intensity (maturing oocytes/distal germline)
1.6
1.4
1.2
1.0
0.8
0.6
0.2
0.0
ns
***
****
**
****
***
***
****
****
****
****
****
****
ns
ns
ns
ns
ns
*
ns
ns
ns
ns
RNAi treatment
Hermaphrodite
Female
Vector control
kin-2
ttr-14
par-5
xpo-1
srab-17
rmd-2
dlg-1
lgc-46
aco-2
imb-1

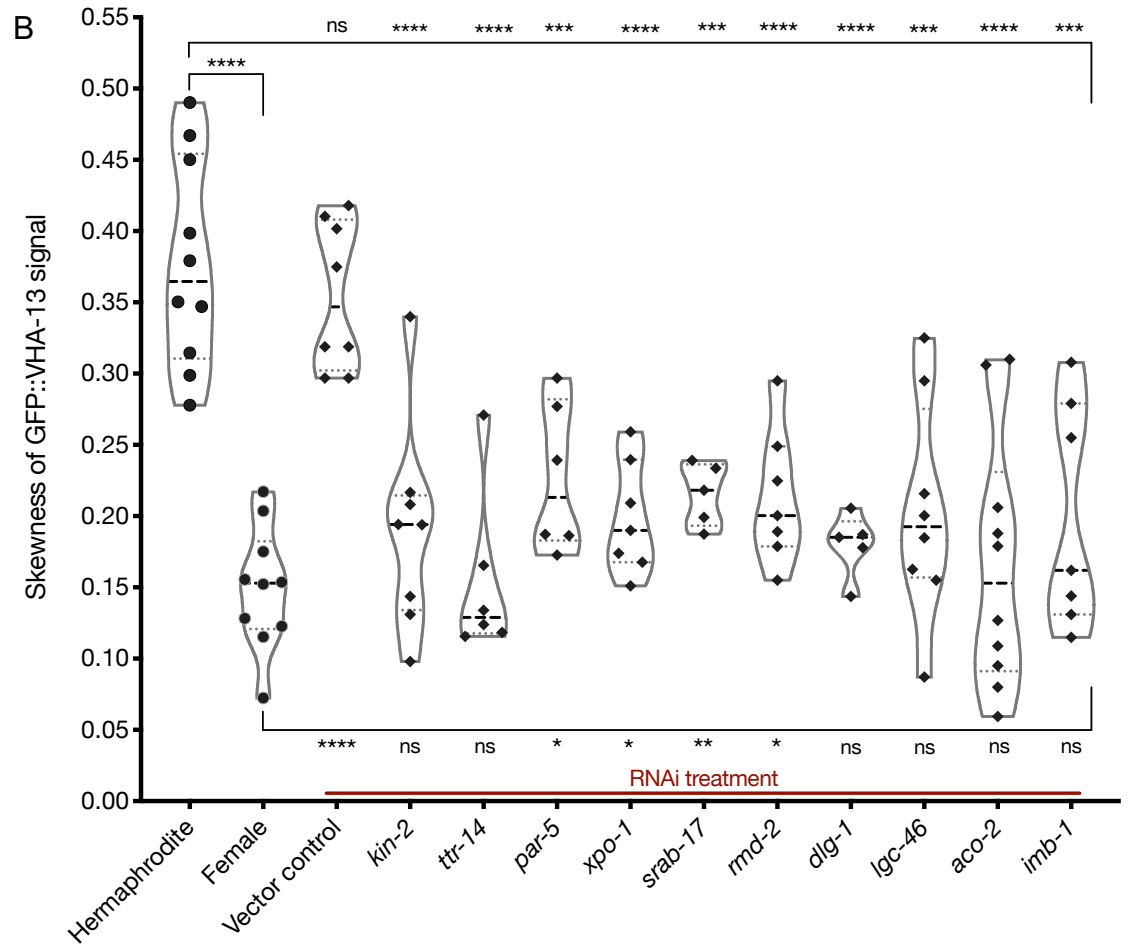
B
Skewness of GFP::VHA-13 signal
0.55
0.50
0.45
0.40
0.35
0.30
0.25
0.20
0.15
0.10
0.05
0.00
ns
****
****
***
****
***
****
****
***
****
***
****
****
ns
ns
*
*
**
*
ns
ns
ns
ns
RNAi treatment
Hermaphrodite
Female
Vector control
kin-2
ttr-14
par-5
xpo-1
srab-17
rmd-2
dlg-1
lgc-46
aco-2
imb-1

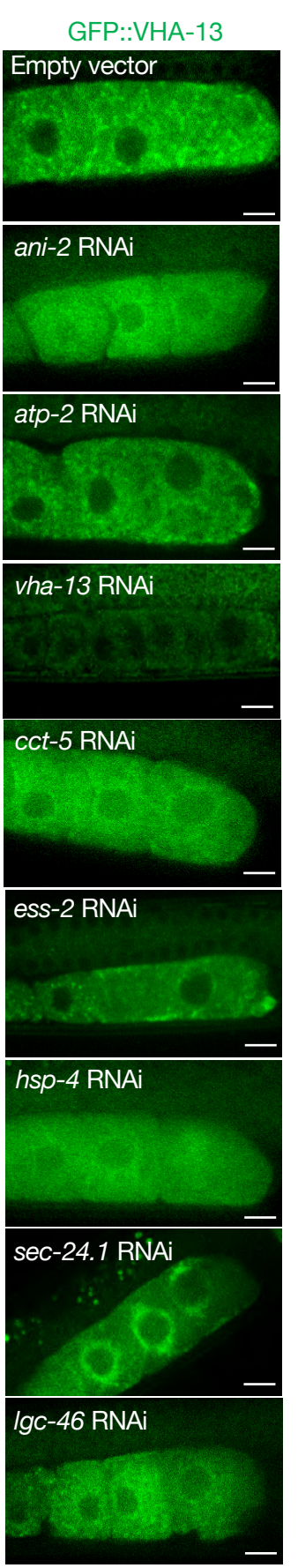
C
GFP::VHA-13
Empty vector
ani-2 RNAi
atp-2 RNAi
vha-13 RNAi
cct-5 RNAi
ess-2 RNAi
hsp-4 RNAi
sec-24.1 RNAi
lgc-46 RNAi

Figure S12.

(A) Analysis of germline LysoTracker staining in hermaphrodites (SA115) subjected to RNAi for the orphan genes. The LysoTracker signal is represented as the ratio of proximal oocyte to distal germline staining, and the values obtained from hermaphrodites (N2E) and females (CF4101) were used as controls (~1.3 and ~1.0, respectively). Each data point represents the average of values from 3 different locations in the most proximal oocyte of a single animal. The presence of GFP::RHO-1 aggregates in the same animals was used as a control to determine successful gene knockdown (not shown). (B) Analysis of GFP::VHA-13 localization (in terms of signal skewness) in hermaphrodites (PHX1414) subjected to RNAi for the orphan genes, and compared to hermaphrodite and female animals (PHX1414 and CF4599). Each data point represents the average of 10 skewness values from independent regions within the first three oocytes of a single animal. The presence of GFP::RHO-1 aggregates in SA115 animals in a parallel experiment served as a control for successful gene knockdown (not shown). For (A) and (B), unpaired t-test with Welch's correction was used to determine the statistical significance. The top and bottom rows of significance indicators in each experiment compare a specific RNAi condition to hermaphrodite and female animals respectively. P values: $P > 0.05$ = n.s., $P \leq 0.05$ = *, $P \leq 0.01$ = **, $P \leq 0.001$ = *** and $P \leq 0.0001$ = ****. (C) Visualization of GFP::VHA-13 distribution and localization in PHX1414 hermaphrodites following RNAi. A few representative gene knockdowns from the assay pool are shown here to demonstrate the range of localization phenotypes observed. Scale bars, 10 μm.

Figure S13

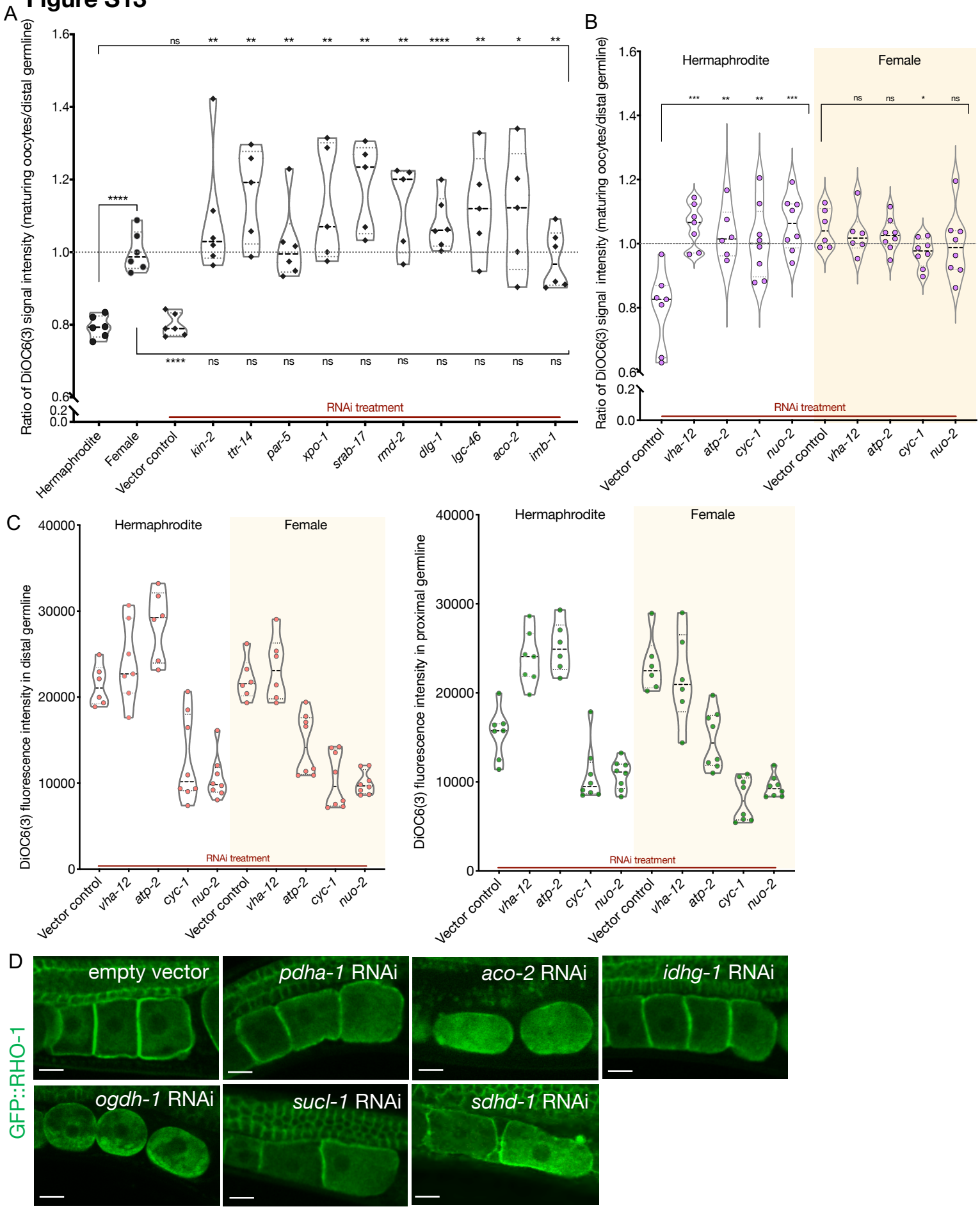
A
Ratio of DiOC6(3) signal intensity (maturing oocytes/distal germline)
RNAi treatment
Hermaphrodite
Female
Vector control
kin-2
ttr-14
par-5
xpo-1
srab-17
rmd-2
dlg-1
lgc-46
aco-2
imb-1
B
Hermaphrodite
Female
Ratio of DiOC6(3) signal intensity (maturing oocytes/distal germline)
RNAi treatment
Vector control
vha-12
atp-2
cyc-1
nuo-2
C
Hermaphrodite
Female
DiOC6(3) fluorescence intensity in distal germline
DiOC6(3) fluorescence intensity in proximal germline
RNAi treatment
D
empty vector
pdha-1 RNAi
aco-2 RNAi
idhg-1 RNAi
ogdh-1 RNAi
sucl-1 RNAi
sdhd-1 RNAi
GFP::RHO-1

Figure S13.

(A) Analysis of germline DiOC6(3) staining in hermaphrodite animals (OCF15) subjected to RNAi for the orphan genes, represented as the ratio of proximal oocyte to distal germline staining. Staining ratios obtained from N2E hermaphrodites (~0.8) and CF4101 females (~1) were used as controls for comparison. Each data point represents the average of values from 3 different locations within the most proximal oocyte of a single animal. When applicable, alteration in ER morphology was used as a control to determine successful gene knockdown in the same animals. The presence of aggregates in GFP::RHO-1 animals (SA115) treated in parallel was also used as a control to verify successful gene knockdown (not shown). The top and bottom rows of significance indicators compare a specific RNAi treatment to hermaphrodites and females, respectively. (B) DiOC6(3) staining expressed as the ratio between proximal oocytes and distal germline, in hermaphrodites (N2E; white) and females (CF4101; yellow) subjected to RNAi treatment for control (*vha-12* and *atp*-2) and electron transport chain (*cyc-1* and *nuo*-2) genes. Successful gene knockdown was determined by monitoring GFP::RHO-1 aggregation in parallel (shown in Figure 5B). (A-B) Unpaired t-test with Welch's correction was used to determine the statistical significance. P values: $P > 0.05$ = n.s., $P \leq 0.05$ = *, $P \leq 0.01$ = **, $P \leq 0.001$ = *** and $P \leq 0.0001$ = ****. (C) For the animals in B, DiOC6(3) signal intensity following RNAi treatment for electron transport chain genes in the distal (left panel) and proximal (right panel) germlines, respectively. *vha-12*-RNAi was used an independent positive control. (D) Identification of Krebs cycle genes that, when knocked down in hermaphrodites (SA115), cause GFP::RHO-1 aggregates to accumulate in oocytes. Scale bars, 10 μm.

Figure S14

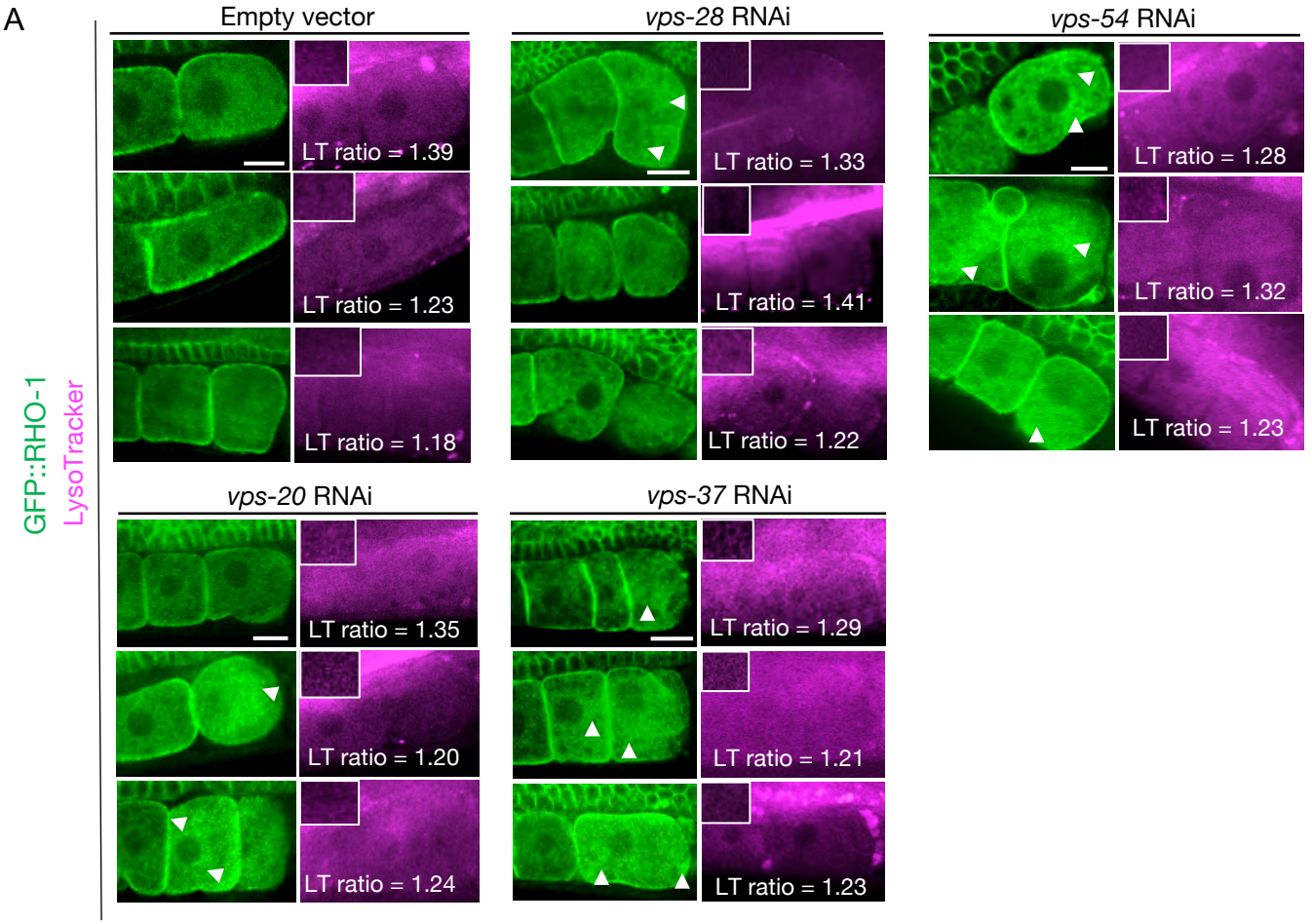
A
Empty vector
vps-28 RNAi
vps-54 RNAi
vps-20 RNAi
vps-37 RNAi
GFP::RHO-1
LysoTracker
LT ratio = 1.39
LT ratio = 1.23
LT ratio = 1.18
LT ratio = 1.33
LT ratio = 1.41
LT ratio = 1.22
LT ratio = 1.28
LT ratio = 1.32
LT ratio = 1.23
LT ratio = 1.35
LT ratio = 1.20
LT ratio = 1.24
LT ratio = 1.29
LT ratio = 1.21
LT ratio = 1.23

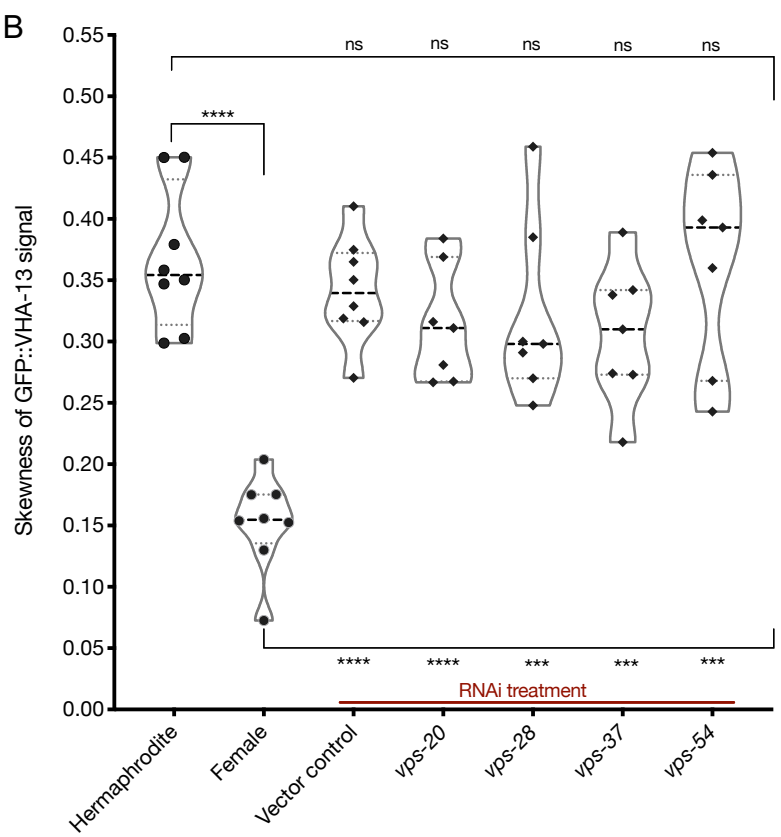
B
Skewness of GFP::VHA-13 signal
0.55
0.50
0.45
0.40
0.35
0.30
0.25
0.20
0.15
0.10
0.05
0.00
ns
****
***
RNAi treatment
Hermaphrodite
Female
Vector control
vps-20
vps-28
vps-37
vps-54

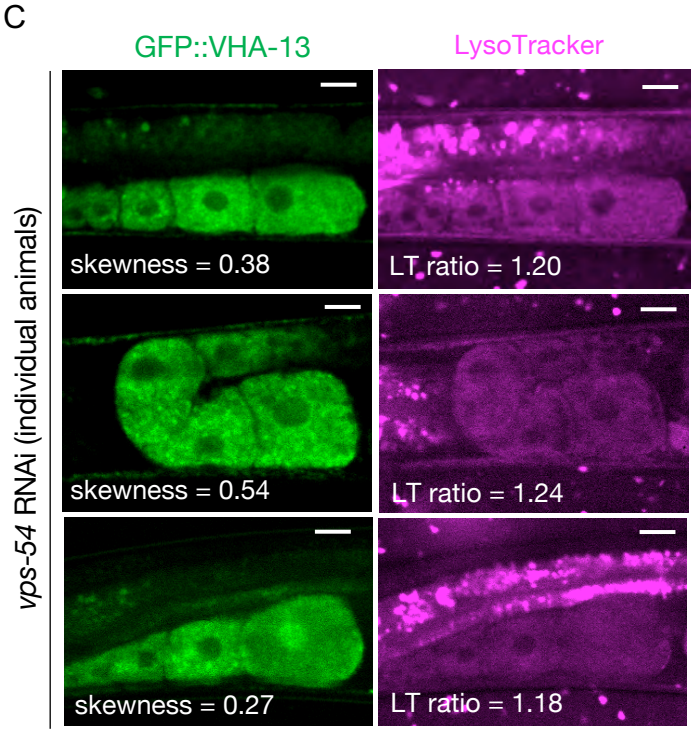
C
GFP::VHA-13
LysoTracker
vps-54 RNAi (individual animals)
skewness = 0.38
LT ratio = 1.20
skewness = 0.54
LT ratio = 1.24
skewness = 0.27
LT ratio = 1.18

Figure S14.

(A) GFP::RHO-1 aggregation and LysoTracker signal in hermaphrodites (SA115) subjected to ESCRT-complex RNAi. The proximal oocyte/distal germline ratio of LysoTracker intensity is indicated for each animal. Distal germline images from the same animal are shown as insets in the LysoTracker panels. LysoTracker staining ratios ranged from 1.18-1.45 and 0.85-1.15 in control hermaphrodites (N2E) and females (CF4101), respectively, across multiple experiments (not shown in this figure). Oocyte GFP::RHO-1 aggregates (confirming knockdown) are indicated with white arrows, and only oocytes containing aggregates were selected for calculating lysosome acidification in Figure 5C. Scale bars, 10 μm. (B) GFP::VHA-13 localization (signal skewness) in hermaphrodites (PHX1414) subjected to RNAi for ESCRT subunits, and compared to hermaphrodites and females (PHX1414 and CF4599 respectively). Each data point represents the average of ten skewness values from different regions within the three most proximal oocytes of a single animal. The top and bottom rows of significance indicators compare a specific RNAi treatment to hermaphrodite and female animals respectively. P values: $P > 0.05$ = n.s., $P \leq 0.001$ = *** and $P \leq 0.0001$ = ****. (C) Variability in GFP::VHA-13 localization and lysosome acidification phenotypes for individual PHX1414 animals treated with *vps-54* RNAi. The skewness value for the GFP::VHA-13 signal and LysoTracker staining ratio (proximal oocyte to distal germline) are indicated for each animal. Successful knockdown could not be verified in each animal (since VHA-13 and RHO-1 were both tagged with GFP). Instead, it was done in a parallel experiment with GFP::RHO-1-expressing animals (SA115) in which more than 75% of animals subjected to a specific RNAi treatment, exhibited detectable aggregation (not shown). Scale bars, 10 μm.

Figure S15

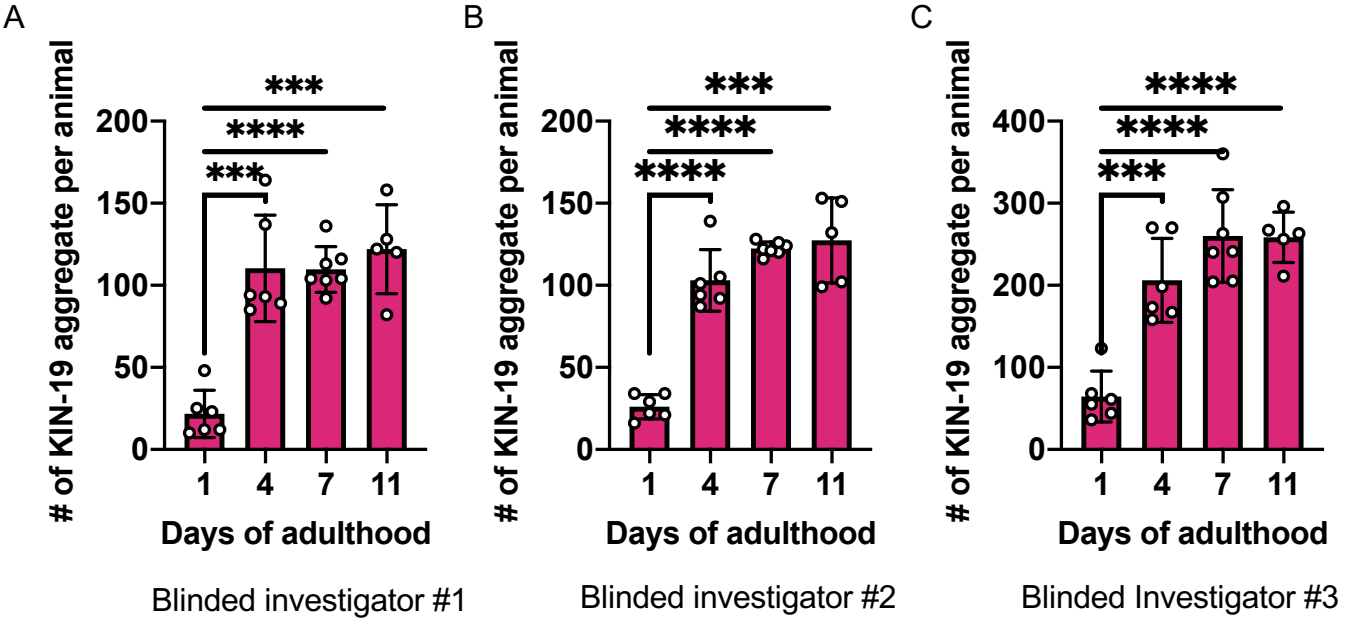
A
# of KIN-19 aggregate per animal
200
150
100
50
0
***
****
***
1
4
7
11
Days of adulthood
Blinded investigator #1
B
# of KIN-19 aggregate per animal
200
150
100
50
0
***
****
****
1
4
7
11
Days of adulthood
Blinded investigator #2
C
# of KIN-19 aggregate per animal
400
300
200
100
0
****
****
***
1
4
7
11
Days of adulthood
Blinded Investigator #3

Figure S15.

Extended data related to Figure 6B.

The same images of KIN-19 aggregates shown in figure 6B were scored again, blindly, by three additional investigators (A, B and C).

Figure S16

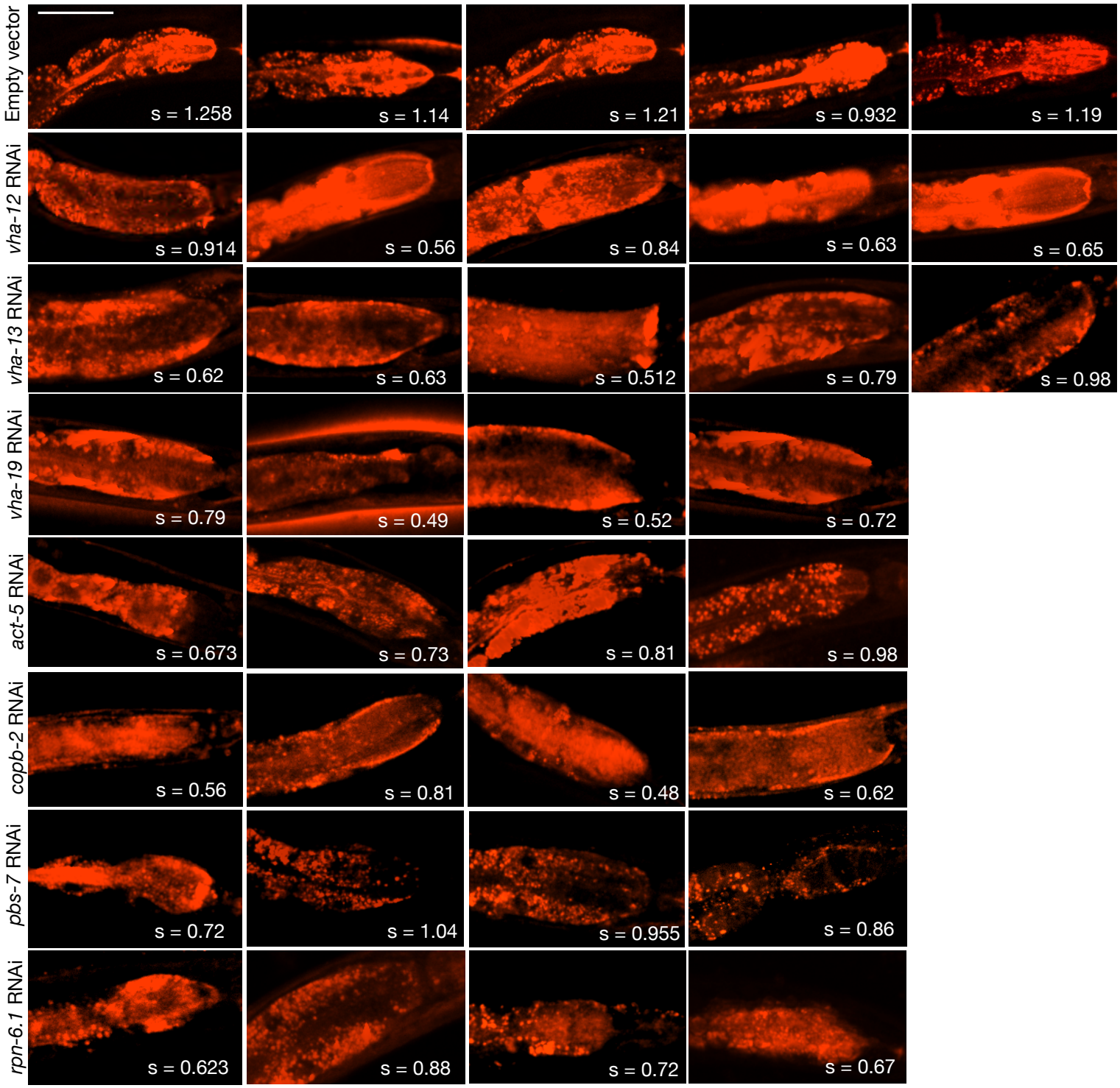
Empty vector
s = 1.258
s = 1.14
s = 1.21
s = 0.932
s = 1.19
vha-12 RNAi
s = 0.914
s = 0.56
s = 0.84
s = 0.63
s = 0.65
vha-13 RNAi
s = 0.62
s = 0.63
s = 0.512
s = 0.79
s = 0.98
vha-19 RNAi
s = 0.79
s = 0.49
s = 0.52
s = 0.72
act-5 RNAi
s = 0.673
s = 0.73
s = 0.81
s = 0.98
copb-2 RNAi
s = 0.56
s = 0.81
s = 0.48
s = 0.62
pbs-7 RNAi
s = 0.72
s = 1.04
s = 0.955
s = 0.86
rpn-6.1 RNAi
s = 0.623
s = 0.88
s = 0.72
s = 0.67

Figure S16.

Lysosome acidification in intestines.

LysoTracker staining in the intestines of animals subjected to gene knockdowns that caused KIN-19 aggregation in the head. Due to variability in dye uptake and staining, the actual LysoTracker signal intensities within the intestines were not evaluated. Instead, the mean skewness values, s, indicative of inhomogeneity expected for acidic intestinal lysosomes (so-called “lysosome-related organelles”), are reported for each animal (compared in Figure 6E). Skewness values were derived from six different locations within the anterior intestinal region near the pharyngeal bulb. Scale bar, 50 μm.

Table S1. Germline proteostasis candidates captured in the screen.

List of candidates obtained from primary screening and validation rounds with GFP::RHO-1. The phenotypic strengths and fertility status are indicated for each. Candidates that were discarded on the basis of their known functions, possible off-target effects, or the failure to pass orthogonal verification with NMY-2::GFP are indicated accordingly.

Table S2. List of *C. elegans* strains

Description of all strains used in the study, including the corresponding genotypes and sources.

Table S3. Candidates from primary screen that did not pass validation

This list is included because some of these candidates could be false negatives, as was the case for the ESCRT-complex genes. Also included are the GO terms (biological process) they represent.